

DEVELOPMENT AND CHARACTERIZATION OF NEXT-GENERATION CONTACT MATERIALS
FOR NANOELECTROMECHANICAL SWITCHES

Frank Streller

A DISSERTATION

in

Materials Science and Engineering

Presented to the Faculties of the University of Pennsylvania

in

Partial Fulfillment of the Requirements for the

Degree of Doctor of Philosophy

2016

Supervisor of Dissertation:

Robert W. Carpick

John Henry Towne Professor and Chair of Mechanical Engineering and Applied Mechanics

Graduate Group Chairperson:

Shu Yang

Professor of Materials Science and Engineering

Dissertation Committee:

David J. Srolovitz, Professor of Materials Science and Engineering

I-Wei Chen, Professor of Materials Science and Engineering

Mark G. Allen, Professor of Electrical and Systems Engineering

DEVELOPMENT AND CHARACTERIZATION OF NEXT-GENERATION CONTACT MATERIALS
FOR NANOELECTROMECHANICAL SWITCHES

COPYRIGHT

2016

Frank Streller

This work is licensed under the
Creative Commons Attribution-
NonCommercial-ShareAlike 3.0
License

To view a copy of this license, visit

<https://creativecommons.org/licenses/by-nc-sa/3.0/us/>

Für Mama und Papa.

ACKNOWLEDGMENTS

Even though this thesis bears the name of a single author, none of it would have been possible without the help and support of countless individuals.

First and foremost, I want to thank my advisor Prof. Robert W. Carpick. Thank you for taking a chance on an undergraduate student from Germany! Your guidance, passion, and direction have helped me tremendously throughout my PhD. I enjoyed the freedom you gave me to explore own ideas while always being there to answer questions. You have been a great advisor and you will be one of the things I will miss most after leaving Penn.

I would also like to thank my committee members, Prof. David Srolovitz, Prof. I-Wei Chen, and Prof. Mark Allen for their time and advice throughout of my PhD studies.

It was a great pleasure to be a part of the DMREF team and work together with Fan Yang, Prof. David Srolovitz, Yubo Qi, Jing Yang, Prof. Andrew Rappe, Dr. Vitali Brand, Changhoo Oh, Prof. Maarten de Boer, James Best, and Prof. Gianluca Piazza. I want to thank each DMREF member for making me a better scientist through helpful, useful and interesting discussions.

I am also truly grateful to Dr. Graham Wabiszewski who took me under his wing when I arrived from Germany and taught me all the important things related (and unrelated) to my work. I am very happy that I had such an amazing partner.

Another important person in my personal and scientific development was my desk neighbor Dr. Filippo Mangolini. Thank you for taking the time to teach me all your XPS tricks and let me be a part of your and your wife Silvia's and your son Leonardo's life.

Thank you also to Dr. Tevis Jacobs, Dr. Vahid Vahdat, Dr. Philip Eberts, and Dr. Jason Bares for being great scientific role models and friends! I want to thank also all other current and former members of the Carpick research group!

I also want to give a special thank you to Dan Durham. I truly enjoyed our time working together and I wish you all the best in your future endeavors.

I also want to acknowledge funding from the NSE DMREF-1334241 grant and the use of University of Pennsylvania Nano/Bio Interface Center, Nanoscale Characterization Facility, and Quattrone Nanofabrication Facility equipment.

It was a great pleasure being a part of such a social and fun department as the MSE department at Penn. I am extremely grateful that I was able to share my PhD experience with my classmates Jacob Berger, Robert Middleton, Dan Magagnosc, Daksh Agarwal and Nick Greybush.

I also want to thank Matteo Cargnello, Chia-Chun Lin, Wei-Shao Tung and Carlos Aspetti for their friendship over the years.

Thank you also to my girlfriend Jessica for always supporting me, being by my side and bringing joy to my life.

Last but not least, I want to thank my parents Ute and Berndt for believe and guidance throughout my life. I know it was not easy for them to let me go to another continent but I greatly appreciate their constant support!

ABSTRACT

DEVELOPMENT AND CHARACTERIZATION OF NEXT-GENERATION CONTACT MATERIALS FOR NANOELECTROMECHANICAL SWITCHES

Frank Streller

Robert W. Carpick

Nanoelectromechanical (NEM) switches were identified by the semiconductor industry as a low-power "beyond CMOS" technology. However, the reliability of the contact interface currently limits the commercialization of NEM switches, as the electrical contact has to be able to physically open and close up to a quadrillion (10^{15}) times without failing due to adhesion (by sticking shut) or contamination (reducing switch conductivity). These failure mechanisms are not well understood, and materials that exhibit the needed performance have not been demonstrated. Thus, commercially viable NEM switches demand the development of novel contact materials along with efficient methods to evaluate the performance of these materials.

To assess contact material candidates under NEM switch-like conditions, we developed a novel, high-throughput electrical contact screening method based on atomic force microscopy (AFM) that enables billions of contact cycles in laboratory timeframes. We compared the performance of self-mated and dissimilar single asperity Pt and Pt_xSi contacts under forces and environments representative of NEM switch operation and cycled up to 10 million times. The contact resistance increased by up to three decades due to cycling-induced growth of insulating tribopolymer in the case of Pt-Pt contacts whereas Pt_xSi exhibited reduced tribopolymer formation.

We also pursued the development of novel contact material candidates that are highly conductive, minimally adhesive, chemically inert, mechanically robust, and amenable to CMOS fabrication processes. One promising candidate material is platinum silicide (Pt_xSi). The controlled diffusion of thin films of amorphous silicon and platinum allowed us to tune the

chemical composition of Pt_xSi over a wide range ($1 < x < 3$). We performed the first measurements of the mechanical and electrical contact properties of Pt_xSi of multiple stoichiometries in comparison with pure Pt. These experiments showed that the platinum-rich silicide phase (Pt_3Si) may be an ideal contact material for NEM switches due to its desirable combination of mechanical robustness with metal-like conductivity. We also demonstrate that Pt_xSi can be used to release NEM switches with a self-formed gap caused by interfacial separation driven by shrinkage-induced tensile stress.

TABLE OF CONTENTS

ACKNOWLEDGMENTS	IV
ABSTRACT.....	VI
LIST OF TABLES	X
LIST OF ILLUSTRATIONS	XI
CHAPTER 1: NANOELECTROMECHANICAL SWITCHES – A “BEYOND-CMOS” TECHNOLOGY.....	1
1.1 The energy dilemma of solid-state computing	1
1.2 Nanoelectromechanical switches as low-power computing alternative.....	4
1.3 Reliability issues in nanoscale electrical contacts	11
BIBLIOGRAPHY CHAPTER 1	20
CHAPTER 2: ASSESSMENT OF NANOELECTROMECHANICAL SWITCH-LIKE CONTACTS USING ATOMIC FORCE MICROSCOPY	23
2.1 Atomic force microscopy to assess nanoscale electrical contact reliability	23
2.1.1 Electrical atomic force microscopy.....	23
2.1.2 Depositing electrical contact materials onto atomic force microscopy probes	27
2.2 Gigacycle interrogation of single asperity contacts	32
2.3 Improved single asperity interrogation method	40
2.3.1 PeakForce Tapping for continuous contact resistance measurements.....	40
2.3.2 Results for platinum-platinum single asperity contacts	45
2.3.3 Effect of probe and sample pre-treatment	47
2.4 Summary	53
BIBLIOGRAPHY CHAPTER 2	55

CHAPTER 3: DEVELOPMENT OF NEXT-GENERATION NANOELECTROMECHANICAL SWITCH CONTACT MATERIALS	56
3.1 Selecting nanoelectromechanical switch candidate contact materials	56
3.2 Platinum silicide as nanoelectromechanical switch contact material	62
3.2.1 Previous work on platinum silicide and its advantages.....	62
3.2.2 Formation of platinum silicide thin films from amorphous silicon and platinum	63
3.2.3 Platinum silicide-based release of microswitches.....	75
3.3 Platinum silicide stoichiometry and properties by design	78
3.3.1 Importance of metal silicide thin films	78
3.3.2 <i>In situ</i> measurements to elucidate platinum silicide formation mechanisms	80
3.3.3 Source-limited solid state diffusion	83
3.3.4 Kinetically-limited solid state diffusion.....	87
3.3.5 Specifics of Pt ₃ Si formation.....	91
3.3.6 Conclusions.....	96
3.4 Electronic properties of platinum silicide films and their control	97
3.5 Preliminary results of single asperity cycling of platinum silicide contacts	106
BIBLIOGRAPHY CHAPTER 3	115
CHAPTER 4: CHEMICAL AND STRUCTURAL CHARACTERIZATION OF TRIBOPOLYMERS	119
4.1 Experimental setup to produce tribopolymer	119
4.2 Spectroscopic characterization of tribopolymers	123
4.3 Summary	129
BIBLIOGRAPHY CHAPTER 4	131
CHAPTER 5: CONCLUSIONS AND FUTURE DIRECTIONS	132
5.1 Future work on contact material assessment.....	135
5.2 Future work on contact material development	138
5.3 Future work on tribopolymer formation and characterization	147
BIBLIOGRAPHY CHAPTER 5	150

LIST OF TABLES

Table 1: Qualitative evaluation of contact material candidates.	60
Table 2: Normalized carrier densities computed from VB XPS experiments and DOS calculations and measured sheet resistance values.	104

LIST OF ILLUSTRATIONS

Figure 1: Schematic timeline illustrating the history of computing.	2
Figure 2: Power consumption of field effect transistors. Static and dynamic power as a function of year and technology node.....	3
Figure 3: The Internet of Things (IoT) revolution will lead to a dramatic increase in mobile devices.	4
Figure 4: Market revenue and future predictions for microelectromechanical systems as of 2013. 5	5
Figure 5: Comparison of typical field effect transistor and nanoelectromechanical contact switch designs.....	7
Figure 6: Electron micrograph of a prototype piezoelectrically-actuated nano-electromechanical switch. Copyright 2014, with permission from IEEE. [28]	8
Figure 7: Schematic comparison of the current vs. voltage characteristics of field effect transistors and nanoelectromechanical switches.	10
Figure 8: Performance evaluation of a NEM switch. Adapted from the International Roadmap of the Semiconductor Industry (ITRS).....	12
Figure 9: Schematic illustrating the complex environment and acting stresses at the NEM switch contact interface.....	13
Figure 10: Adhesive failure in Au-Au microcontacts. Part of the top Au coating is permanently stuck to the bottom contact bump. [44] © IOP Publishing. Reproduced with permission. All rights reserved.	14
Figure 11: Tribopolymer formation in historic telephone contacts [48]. Left: experimental setup of telephone switch operated in glass tube of controlled atmosphere. Inset shows zoomed-in contact region. Right: top view of tribopolymer on Pd contact after 10 ⁶ switching cycles. Courtesy of Nokia © 1958 Nokia. All Rights Reserved.....	16
Figure 12: Contamination failure in AuRu _x -AuRu _x contacts [47]. Left: AuRu _x contact bump before switching. Right: AuRu _x counter surface after switch failure due to tribopolymer formation. Copyright 2007, with permission from AIP Publishing.	17
Figure 13: a) Schematic of NEM switch design utilized by Jang <i>et al.</i> and b) electron microscopy cross-section of the NEM switch indicating the TiO _x -coated bottom contact [51]. Copyright 2008, with permission from AIP Publishing.....	18
Figure 14: Schematic of the AFM-based test setup used to interrogate NEM switch contact materials. The tip and sample are coated with candidate films, and testing is then carried out under desired environments and testing conditions.	25
Figure 15: Schematic of a SolidWorks drawing of the AFM probe holder for coating inside a sputtering system. The holder can host 16 AFM probe chips and protects the cantilever from damage during the coating process, as well as enables easy flipping of the chips to enable backside coating. A loaded AFM probe chip is shown in magenta.	29

Figure 16: Image of two AFM probe chip holders (with 16 AFM probe chips each) loaded onto the Explorer 14 sputterer turntable, together with two half-wafer witness samples..... 30

Figure 17: Schematic of a SolidWorks drawing of the AFM probe holder usable in a rapid thermal annealing system. The holder can host 6 AFM probe chips and protects the cantilevers from damage during the heating process. A loaded AFM probe chip is shown in magenta..... 31

Figure 18: Image of the AFM probe chip holder loaded on the rapid thermal annealing crucible holder. The AFM probe chips are fixated using a screw in order to protect the cantilever from damage. 32

Figure 19: Simultaneous measurements of current and force during an AFM force-distance (FD) measurement with a 200 mV bias applied between a Pt-coated AFM probe tip and a Pt counter surface. A TEM micrograph of the probe tip used in this measurement is shown in the inset. 35

Figure 20: (A) 1156 force-distance measurements under 200 mV bias with simultaneous current measurements are performed before and at regular intervals throughout high-speed cycling of a nanoscale Pt-Pt interface. Histograms of the current response at maximum load (40 nN) are then produced. (B) Current measurements are converted to contact resistance and the median, lower quartile, and upper quartile values are reported as a function of the number of contact cycles. (C) The force of adhesion as a function of cycles is shown. Error bars represent the standard deviation of each ensemble of measurements. 37

Figure 21: Low-resolution (A) and high resolution (B) Pt-coated AFM probe tip before cycling. (C) High resolution image of the same Pt-coated AFM probe after 2×10^9 cycles with 100 mV bias voltage shows the addition of low density material in the contact area. 39

Figure 22: General operation principle of PeakForce Tapping® AFM. The cantilever is driven by a sine wave signal and the curves are presented as force vs. time and force vs. z-position [15]. a) Tip trajectory as it approaches the sample. b) Plots of the deflection/force as a function of time and z-position. (Copyright 2011 Bruker Corporation) 41

Figure 23: Plots of the z position, force and current as a function of time during a PeakForce TUNA™ interaction cycle. Point B corresponds to the snap-in point, point C represents the peak force value and point D corresponds to the adhesion value [16]. (Copyright 2011 Bruker Corporation) 43

Figure 24: Schematic (top) and image (bottom) of PeakForce TUNA™ setup used to interrogate the cycling behavior of single asperity contacts..... 44

Figure 25: Atomic force microscopy lifetime tests of Pt-Pt nanocontacts. Pt-coated AFM probes exhibit more than 3 orders of magnitude increase in contact resistance after cycling to 10^7 contact cycles while adhesion increases only marginally..... 46

Figure 26: Illustrations of sample pre-treatment methods. a) Pt-coated tip and sample tested in the as-deposited state without any pre-treatment. b) Pt-coated tip was scanned in contact mode over the sample to physically remove any contaminants. c) Oxygen plasma cleaning was employed on both, Pt-coated tip and sample, so remove any hydrocarbon contaminants. 48

Figure 27: Atomic force microscopy lifetime tests of Pt-Pt nanocontacts subject to different pre-treatment methods. Untreated Pt-Pt contact exhibits more than 3 orders of magnitude increase in contact resistance after cycling to 10^7 contact cycles. Slide-cleaned contact exhibits reduced

contact resistance increase, whereas plasma-cleaned contacts maintain initial contact resistance over 10^7 contact cycles.	49
Figure 28: Adhesion behavior during atomic force microscopy lifetime tests of Pt-Pt nanocontacts subject to different pre-treatment methods. Adhesion force increases continuously for the untreated and slide-cleaned Pt-Pt samples. Adhesion force initially increases until $5 \cdot 10^5$ cycles for the plasma-cleaned Pt-Pt sample and then becomes unstable.	50
Figure 29: Angular-resolved high resolution XPS spectra of the C 1s peak. Oxygen plasma cleaning reduces the C 1s peak noticeable due to its removal of adventitious carbon. The red area in the plasma-cleaned Pt C 1s spectrum represents the as-deposited Pt C 1s spectra at 0° for reference.	52
Figure 30: Angular-resolved high resolution XPS spectra of the Pt 4f peaks. Oxygen plasma cleaning forms small amounts of platinum oxygen, while still maintaining most of the metallic platinum.	53
Figure 31: Desired properties of NEM switch contact materials.	57
Figure 32: Example of the NEM contact materials selection process for pure elements. After applying materials property criteria, only 8 out of initially 111 elements remain realistic candidates as contact material for NEM switches.	58
Figure 33: Schematic of typical Pt_xSi formation using a thin layer of Pt deposited onto a cleaned <i>sc</i> -Si wafer, and subsequently annealed. In the first reaction, the Pt diffuses into the <i>sc</i> -Si and the intermediate Pt-rich silicide Pt_2Si is formed. After all Pt is consumed, the <i>sc</i> -Si diffuses into Pt_2Si to form the thermodynamically stable PtSi phase. The temperature range of the Pt_2Si formation ($180-200^\circ C$) and the PtSi formation ($280-400^\circ C$) are within the thermal budget of most CMOS processes.	63
Figure 34: <i>a</i> -Si/Pt samples. d, Schematic and SEM cross-section image of the as-deposited Pt: <i>a</i> -Si = 1:1 sample. e, Schematic and SEM cross-section image of the as-deposited Pt: <i>a</i> -Si = 1:2 sample.	64
Figure 35: Surface Characterization of as-deposited Pt and formed Pt_xSi . a, High-resolution XPS spectra of the Pt 4f peaks of the annealed Pt: <i>a</i> -Si = 1:2 spectra. The Pt 4f peaks shift to higher binding energies indicating Pt_xSi formation with progressively increase Si content. The near-surface composition of the annealed Pt: <i>a</i> -Si = 1:2 sample is dominated by Si-rich PtSi. b, High-resolution XPS spectra of the Pt 4f peaks of the annealed Pt: <i>a</i> -Si = 1:1 spectra. The Pt 4f peaks shift to higher binding energies indicating Pt_xSi formation. Near-surface composition of the annealed Pt: <i>a</i> -Si = 1:1 sample dominated by Pt-rich Pt_xSi . c, High-resolution XPS spectra of the Pt 4f peaks of the as-deposited sample. The Pt 4f peaks indicate the presence of pure metallic Pt.	66
Figure 36: Nanoindentation of as-deposited Pt and formed Pt_xSi . a, Modulus and hardness as a function of indentation depth curves for the Pt: <i>a</i> -Si = 1:1 sample in the as-deposited and annealed state. Both modulus and hardness shoulder at approximately 50 nm indentation depth, indicating that this depth is ideal for measuring the thin film properties. b, Average modulus and hardness values and their standard derivations obtained from 100 depth-controlled indentations at 50 nm indentation depth for the Pt: <i>a</i> -Si = 1:1 and Pt: <i>a</i> -Si = 1:2 samples in their as-deposited and annealed states. For both Pt: <i>a</i> -Si ratios, the modulus and hardness significantly increased due to the Pt_xSi formation compared to the as-deposited film.	68

Figure 37: Conducting-mode contact atomic force microscopy measurements of as-deposited Pt and Pt_xSi samples. a-c, Contact resistance color relief maps of a representative 200 nm x 200 nm scan on a representative a) as-deposited Pt film, b) annealed Pt:*a*-Si = 1:1, and c) annealed Pt:*a*-Si = 1:2. Insets show the contact resistance distribution obtained from each scan. The contact resistance distribution shifts towards higher contact resistances with increasing *a*-Si availability from a-c. d, Minimum contact resistance values encountered during the 200 nm x 200 nm scans. Annealed Pt:*a*-Si = 1:1 film possesses contact resistance values approximately 10 % higher than those seen in pure Pt films. The higher *a*-Si content in the Pt:*a*-Si = 1:2 film leads to a further increased contact resistance to approximately twice the value of as-deposited Pt. However, these values are still within the same order of magnitude of pure Pt and well within acceptable bounds for NEM switches. 70

Figure 38: AFM contact resistance and topography images of a Pt-coated sample measured with a Pt-coated probe. The locations of three line scans are indicated on both images. 71

Figure 39: Height and contact resistance line scans of a Pt-coated sample. Peaks of the sample are correlated to low contact resistances and valleys of the sample are correlated to high contact resistances. 72

Figure 40: Height and contact resistance data of Line 1 plotted with equal scale bars for scan distance and height. Transmission electron microscopy image of a Pt-coated AFM probe is shown with identical scale bar than the scan distance and height. 74

Figure 41: Schematic and SEM cross-section of the Pt_xSi-based silicide-release process. A Pt layer, which is initially sandwiched between two *a*-Si layers, diffuses into the *a*-Si layers upon rapid thermal annealing for 5 minutes at 600 °C and two completely separated Pt_xSi layers are formed. 75

Figure 42: Schematic of a resistive, passive-cooled heater for use in a scanning electron microscope (SEM)..... 76

Figure 43: Screenshots of the scanning electron microscope (SEM) image and temperature measurement during heating of a SAC305 soldering alloy. a) Graph of the time-temperature recording during experiment. b) SEM image of the solder alloy at a temperature below T_{melt}. c) SEM image of the solder alloy at a temperature just above T_{melt}. 77

Figure 44: Schematics of the as-deposited and annealed samples and the used in situ TEM annealing technique 81

Figure 45: Source-limited Pt_xSi formation. a, Electron diffraction pattern of as-deposited Pt and Pt₃Si, Pt₂Si, and PtSi films produced using source-limited solid-state diffusion. Grey slices indicate diffraction ring positions according to the theoretical crystal structure shown schematically for each phase. b, Schematic of the source-limited solid-state diffusion process which utilizes precise control of the Pt and *a*-Si precursor film thicknesses to predetermine the desired Pt_xSi phase. c, High-resolution XPS spectra of the Pt_{4f} peaks for as-deposited Pt and resulting Pt_xSi formed on TEM grids using source-limited solid-state diffusion. PtSi sample (Pt:*a*-Si=1:3): quantitative analysis indicates formation of 92% of PtSi. Pt₂Si sample (Pt:*a*-Si=1:1): quantitative analysis indicates formation of 70% Pt₂Si. Pt₃Si sample (Pt:*a*-Si=2:1): quantitative analysis indicates formation of 74% Pt₃Si. Pt sample: quantitative analysis indicates the presence of pure metallic Pt 85

Figure 46: Kinetically-limited Pt_xSi formation. a, Electron diffraction pattern of as-deposited Pt and Pt₃Si, Pt₂Si, and PtSi films produced using kinetically-limited solid-state diffusion. Grey slices

indicate diffraction ring positions according to the theoretical crystal structure shown schematically for each phase. b, Schematic of the kinetically-limited solid-state diffusion process which utilizes precise control of the temperature-time regime to obtain the desired Pt_xSi phase. c, High-resolution XPS spectra of the Pt_{4f} peaks for as-deposited Pt and resulting Pt_xSi formed on TEM grids using kinetically-limited solid-state diffusion. *PtSi sample* (heated to 200 °C): quantitative analysis indicates formation of 91% of PtSi. *Pt₂Si sample* (heated to 300 °C): quantitative analysis indicates formation of 72% Pt₂Si. *Pt₃Si sample* (heated to 500 °C): quantitative analysis indicates formation of 88% Pt₃Si. *Pt sample*: quantitative analysis indicates the presence of pure metallic Pt. 88

Figure 47: Comparison of diffraction pattern intensity distributions obtained from the kinetically-limited and source-limited solid-state diffusion samples. Peak locations and intensity ratios are similar for both methods and indicate that the two methods produce similar Pt_xSi compositions. The theoretical peak positions of the four strongest peaks are indicated by the downward arrows. 90

Figure 48: Determination of the dominant diffusing species (DDS) during Pt₃Si formation. a, The schematic and the TEM image on the left shows the as-deposited sample: an *a*-Si film covered by Pt nanoparticles. Annealing will lead to Pt₃Si formation. If Pt is the DDS, then the Pt nanoparticles will diffuse into the underlying *a*-Si layer and the Pt-containing region (high Z contrast) will appear larger in TEM images. If Si is the DDS, then the nanoparticle shape and size will be nearly preserved and no major change of the high Z contrast region will be visible in the TEM. b, TEM images of several Pt nanoparticles before (at 130 °C) and after (280 °C) Pt₃Si formation. The overall shape and size of the Pt and Pt₃Si nanoparticles is similar, indicating that Pt₃Si formation occurs through diffusion of *a*-Si into Pt. The electron diffraction pattern shows that Pt₃Si particles were formed. 93

Figure 49: TEM image of formed Pt₃Si nanoparticles. Comparison of the initial Pt and resulting Pt₃Si nanoparticle sizes ($r_{Pt} \approx 8.8$ nm, $r_{Pt_3Si} \approx 10.0$ nm) show a particle radius increase due to Pt₃Si formation of similar magnitude then the theoretical value of 9%. 95

Figure 50: TEM images of anti-phase boundaries (APBs) formed in Pt₃Si and electron diffraction image of APB shows single-crystal diffraction spots. 96

Figure 51: Fermi edge shapes and locations in XPS spectra. a. Schematic Fermi edge shape of a metal, a semimetal, and a semiconductor. The intensity of charge carriers at the Fermi edge reduces from metals to semimetals and becomes zero for semiconductors. b. Location of the Fermi edge within an experimental Pt XPS spectrum. The Fermi edge is located at a binding energy value of 0 eV. 99

Figure 52: Experimental and theoretical Fermi edge shapes and compositions for [Pt], [Pt₃Si], [Pt₂Si], and [PtSi] samples. a. Experimental Fermi edge shapes of [Pt], [Pt₃Si], [Pt₂Si], and [PtSi] samples. Valence band electron population decreases with increasing Si-content of the silicide. b. Theoretical Fermi edge shapes of [Pt], [Pt₃Si], [Pt₂Si], and [PtSi] samples. Valence band electron population decreases with increasing Si-content of the silicide. The dotted vertical lines represent the location of the Pt_{5d} manifold for PtSi (2.7 eV below Fermi edge), Pt₂Si (1.8 eV below Fermi edge), and Pt₃Si (0.5 eV below Fermi edge). c. Thin film composition of [Pt], [Pt₃Si], [Pt₂Si], and [PtSi] samples as determined from quantitative XPS measurements. 101

Figure 53: Comparison between experimental and theoretical Fermi edge shapes for [Pt], [Pt₃Si], [Pt₂Si], and [PtSi] samples. a. [Pt] sample (100% metallic Pt). b. [Pt₃Si] sample (which includes 74

% Pt ₃ Si). c. [Pt ₂ Si] sample (which includes 70% Pt ₂ Si). d. [PtSi] sample (which includes 92% PtSi).....	103
Figure 54: Sheet resistance of [Pt], [Pt ₃ Si], [Pt ₂ Si], and [PtSi] samples.	105
Figure 55: Schematic of the Pt _x Si AFM probe fabrication process. A commercial <i>sc</i> -Si AFM probe is sequentially coated with thin films of <i>a</i> -Si and Pt. Pt _x Si is later formed through a rapid thermal annealing treatment at 500°C for 10 minutes.	108
Figure 56: Fabrication process of Pt _x Si probes including electron micrographs and electron diffraction images. a) As-received <i>sc</i> -Si AFM probes possess an oxide-sharpened end. b) Contact AFM scans used to physically remove the silicon oxide and create a reproducible tip geometry. c) Sequential coating of the front- and backside of the AFM probe with <i>a</i> -Si and Pt. Electron beam diffraction image shows diffraction pattern typical of Pt. d) Annealing of coated AFM probes creates Pt _x Si. Electron beam diffraction image shows Pt _x Si diffraction spots appearing (marked with red circles).	110
Figure 57: Atomic force microscopy lifetime tests of Pt-Pt and Pt _x Si-Pt nanocontacts. Pt _x Si-coated AFM probes exhibit constant contact resistance of 10 ⁷ cycles, whereas Pt-coated AFM probes exhibit a 3 order of magnitude increase in contact resistance. The adhesion force of the Pt _x Si-coated AFM probe becomes unstable after 3·10 ⁵ cycles.	112
Figure 58: Density functional theory (DFT) calculations of the interaction of benzene (C ₆ H ₆) with Pt and PtSi surfaces. Side view of the simulation box showing the strong adsorption of benzene on Pt and weaker adsorption of benzene on PtSi surfaces.	113
Figure 59: Experimental setup and results of the macrotribometer experiment to form tribopolymer. a) Schematic and picture of the experimental setup. A Pt-coated steel ball is slid against a Pt-coated shim stock under a benzene-containing atmosphere. b) Friction coefficient and normal load as a function of sliding time and sliding distance. The friction coefficient stayed below 0.6, indicating Pt-Pt contact throughout the experiment.	121
Figure 60: Optical images and profilometry of the wear track. a) Optical image of the whole wear track with three zoom-in regions (labeled A, B, C) indicating the different types of tribopolymer formed. b) Optical image of the unworn Pt-coated sheet stock. c) Cross-sectional measurement of the wear track topography using a scanning white light interferometer. The locations of the two cross-sections are indicated in a).	123
Figure 61: Energy-dispersive X-ray spectroscopy (EDX) measurements of the three identified tribopolymer kinds. a) EDX map of the carbon concentration. b) EDX line scan of carbon, oxygen and platinum concentrations in tribopolymer type B. The location of the cross-section is illustrated by the dotted line.	125
Figure 62: Schematic of the Anasys nanoIR2™ working principle. The sample is illuminated with pulses of IR radiation and an AFM probe is utilized to detect the absorbed radiation with nanoscale spatial resolution. [10].....	127
Figure 63: Nano infrared (nano-IR) measurements of the unworn Pt-coated shim stock and the three identified tribopolymer types. The break in signal between 2200 cm ⁻¹ and 2300 cm ⁻¹ corresponds to a change in excitation laser.....	128
Figure 64: Example of Pt-Pt cycling tests conducted with modified cycling methodology including slow force-distance cycling in the beginning of the test.	137

Figure 65: Schematic of the *in situ* TEM cycling and scratch tests setup. A Hysitron PicoIndenter probe made out of conductive diamond will be cycled or scratched against a Pt_xSi or any other coated AFM probe under an applied bias. In the case of cycling, the pull-off force and contact resistance can be measured during the test to evaluate the early-lifetime behavior of the single-asperity contact. 140

Figure 66: Contact resistance and adhesion as a function of contact cycles for Ru-coated AFM probes in different pretreatment states. 143

Figure 67: Force-distance and current-distance curves of a Pt-coated AFM probe against a graphene-coated Pt sample. 144

Figure 68: Scanning electron microscopy (SEM) image of the graphene-covered Pt foil. 145

Figure 69: AFM topography and conductivity measurements of Gr-Pt sample. Top row: 5 μm x 5 μm topography (left) and conductivity (right, in A) scan on Gr-Pt sample. Bottom row: 500 nm x 500 nm topography (left) and conductivity (right, in A) scan on Gr-Pt sample. 146

CHAPTER 1: NANOELECTROMECHANICAL SWITCHES – A “BEYOND-CMOS” TECHNOLOGY

Nanoelectromechanical (NEM) switches were identified by the roadmap of the semiconductor industry as a low-power “beyond CMOS” technology [1,2]. NEM switches feature nanoscale moving parts that open and close a conductive path, making them a mechanical alternative to traditional solid-state, field-effect transistors [3]. The macroscale mechanical relay marks the founding technology in the history of computing (Figure 1) and continues to be of technological importance in reed switches. However, the reliability of the contact interface currently limits the commercialization of nanoscale switches, *i.e.* NEM switches, as the electrical contact has to be able to physically open and close up to a quadrillion (10^{15}) times without failing, which typically occurs due to adhesion (by sticking shut) or contamination (reducing switch conductivity) [4]. These failure mechanisms are not well understood, and materials that exhibit the needed performance have not been demonstrated. Thus, the development and characterization of materials that can avoid such failures presents a significant scientific challenge. This chapter will discuss the need for low energy computing using NEM switches, the advantages of this technology, and the reliability issues that currently limit the commercialization of NEM switch technology.

1.1 The energy dilemma of solid-state computing

The fully-electronic field-effect transistor (FET), the heart of the integrated circuit (IC), has fueled a constant growth in computing power in combination with a decrease in computing cost for the last half century (Figure 1). This solid-state computing technology

has performed exceptionally in terms of an exponential increase in the aerial density of transistors in order to achieve faster switching times [5]. This trend, dubbed as Moore's Law [6], constitutes that the number of transistors per chip doubles every 18 months and has been true since the 1960s [7].

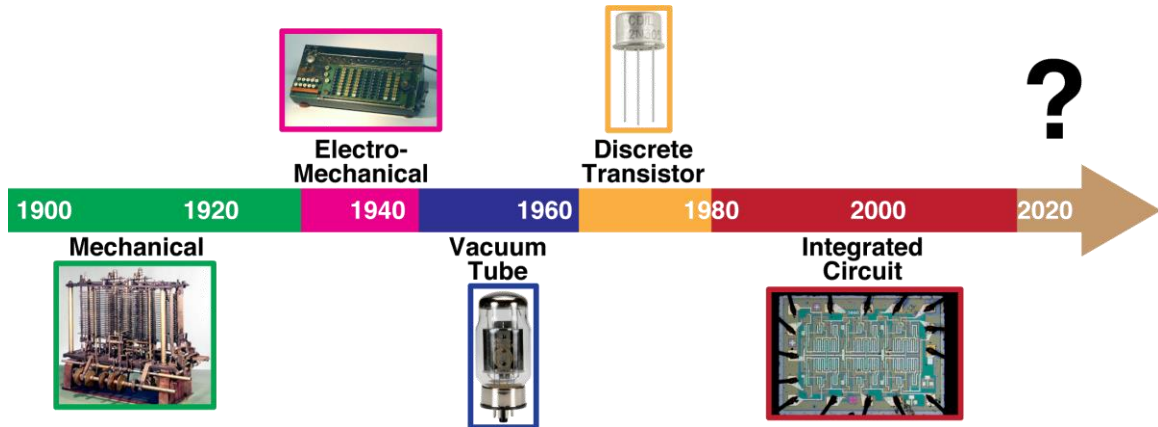


FIGURE 1: Schematic timeline illustrating the history of computing.

However, aggressive scaling of FETs has led to a “power crisis” in the semiconductor industry [1]. Increasing amounts of device leakage, resulting in significant power losses, are typical for scaled FETs, even when switching is not occurring [5,8,9,10]. Figure 2 shows the development of dynamic power (power used to switch the FET) and static power (power lost due to leakage) in FETs as a function of their critical feature size and year. It can be seen that since a decade, FETs lose more power due to leakage than they consume to fulfil computational tasks. The reduction of turn-on voltages in FETs is stalled by the fundamental physics of switching using the field effect, motivating the need for new switching approaches. This dilemma led the "International Technology Roadmap for Semiconductors" (ITRS), a guideline document for the

semiconductor industry, to announce the final stage of down-scaled FETs for the year 2022 [1,11].

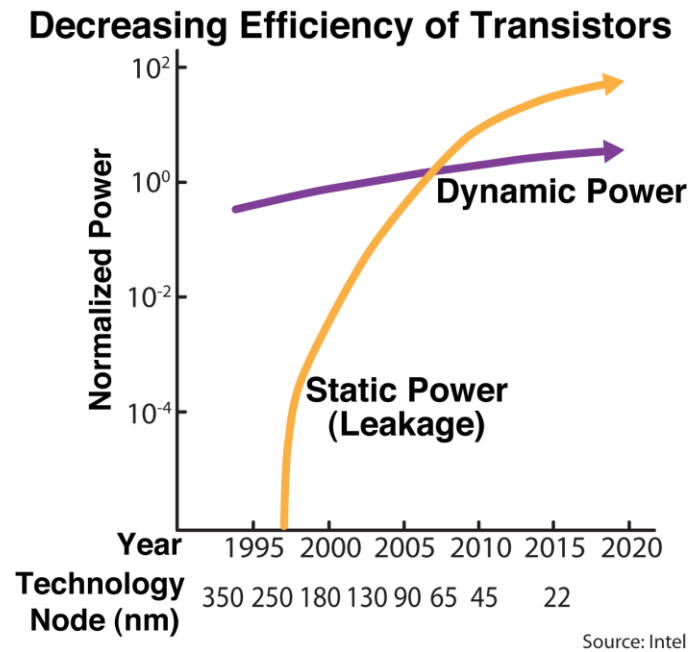


FIGURE 2: Power consumption of field effect transistors. Static and dynamic power as a function of year and technology node.

A 2009 report estimates that 15% of the overall power grid load is due to home computers and electronics [12,13]. The United States alone consumes power equal to five 1 GW power plants, totaling an electricity bill of almost \$3B for the operation of servers alone [14]. Intel's ICs increased in power consumption from 5 W in 1989 to 75 W in 2000 [12]. This CMOS power crisis is even more precarious as the Internet of Things (IoT) movement will accelerate over the next years, leading to an increasing demand for mobile, smart, and interconnected devices featuring long battery lives. Figure 3 illustrates the explosion in the number of mobile devices over the next years, surpassing

50 billion by the year 2020. This rapid increase in battery-powered devices in the next years is mainly due to the increasing utilization of sensors.

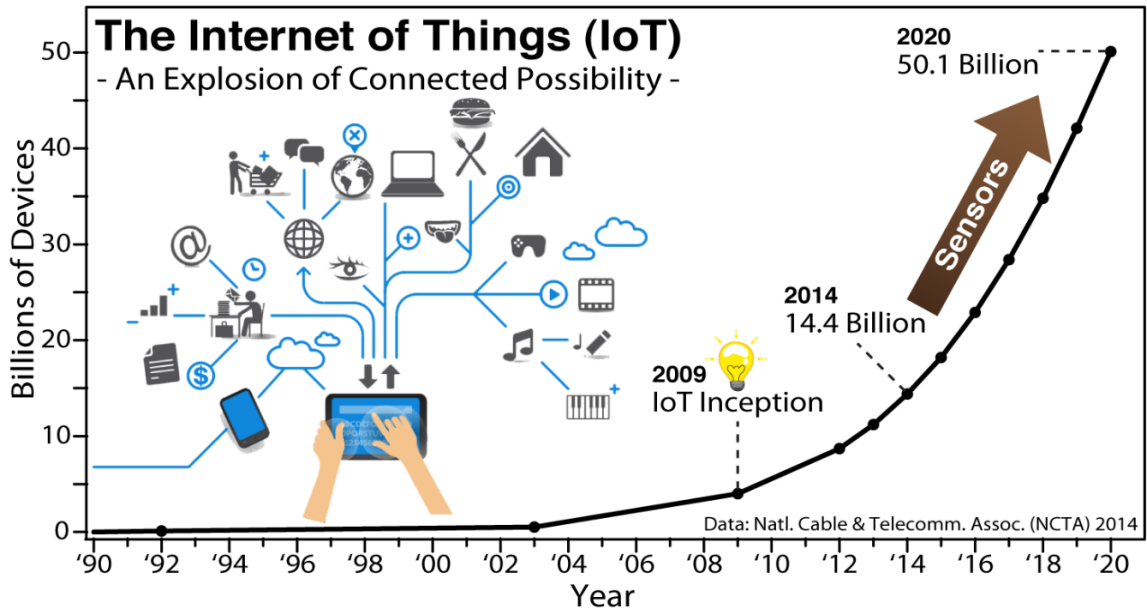


FIGURE 3: The Internet of Things (IoT) revolution will lead to a dramatic increase in mobile devices.

The increasing trend towards smart, mobile devices [12], increasing spread of home and laptop computers into developing countries [12] and the demand for long lasting battery-operated devices [15] reinforces the need for low power computation technologies.

1.2 Nanoelectromechanical switches as low-power computing alternative

Nanoelectromechanical (NEM) switches are considered as one of seven “Beyond CMOS” technologies by the 2008 ITRS report [1]. Their larger counterparts,

microelectromechanical systems (MEMS), gained increasing popularity over the past decade and constitute a \$15B industry to date, mainly due to airbags, ink-jet printers, and projectors (see Figure 4).

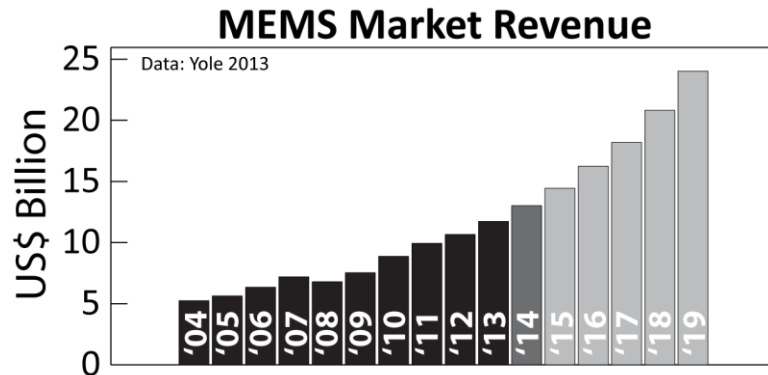


FIGURE 4: Market revenue and future predictions for microelectromechanical systems as of 2013.

A NEM switch utilizes mechanical motion to modulate electrical current flow, whereas a FET uses the so called “field effect” that changes the electrical resistance along a normally insulating layer through the application of an electric field. Figure 5 compares the design of a typical NEM switch with that of a FET. A FET switches to its “ON” state (current flows between source and drain terminals), after a voltage above a certain threshold (note: the threshold voltage is defined as the voltage where the source-drain current reaches 90% of its maximum value) is applied at the gate terminal. This gate voltage causes the formation of an n-type channel (note: p-type channels can also be formed, if source and drain are p-doped and rest of the wafer is n-doped) below the gate oxide (shown in orange in Figure 5) that allows for source-drain current flow. After

the removal of the gate voltage, that conductive channel disappears, which leads to a drastic reduction in source-drain current and represents the “OFF” state of the switch. A NEM switch uses mechanical actuation to physically make and break an electrical contact between two conductive surfaces, corresponding to source and drain electrodes. The NEM device is in its “OFF” state when the source and drain electrodes are separated by an air gap, as shown in Figure 5. The switch reaches its “ON” state after the air gap between source and drain electrodes is closed with sufficient force to enable electrical current flow. In order to close the air gap, a gate voltage is converted to mechanical motion to decrease the source-drain separation until closure of the air gap. Various actuation methods can be employed to achieve the desired mechanical motion. Commonly, electrostatic (as exemplified in Figure 5) [16,17,18] and piezoelectric actuation [18,20,21] mechanisms are being utilized. Flexible beams (as exemplified in Figure 5) [18,20,21], anchorless bridges [22], nanowires [23], nanotubes [24,25,26], graphene films [27] and tethered structures are typical topologies that are being actuated. Even though NEM switches can feature a large range of actuation mechanisms and topologies, their underlying operation principle remains the same: closing and opening of a conductive interface to allow or stop source-drain current flow.

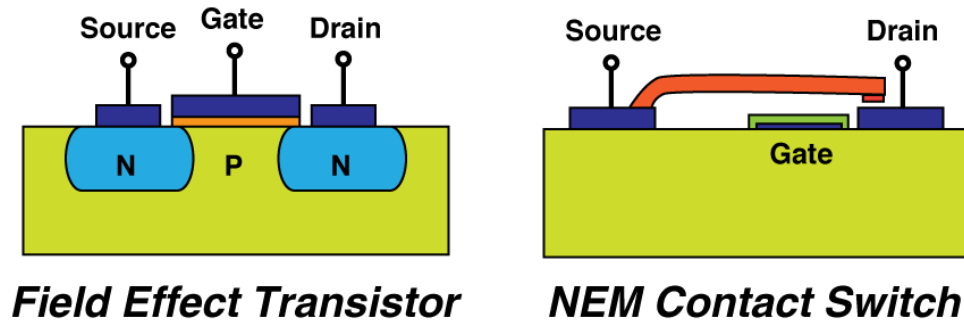


FIGURE 5: Comparison of typical field effect transistor and nanoelectromechanical contact switch designs

Figure 6 shows electron micrographs of a prototype NEM switch developed by our collaborators in the Piazza group and fabricated at Carnegie Mellon University [28]. This switch is piezo-electrically actuated to enable electrical contact between a Pt-coated tip and Pt-coated source and drain electrodes. After the gate pushes the tip into contact with both electrodes (as seen in the oblique view in Figure 6), current can flow from the source electrode, through the tip, to the drain electrode. The switch is in its “OFF” state when the tip is lifted away from source and drain electrode, which are normally separated by an air gap.

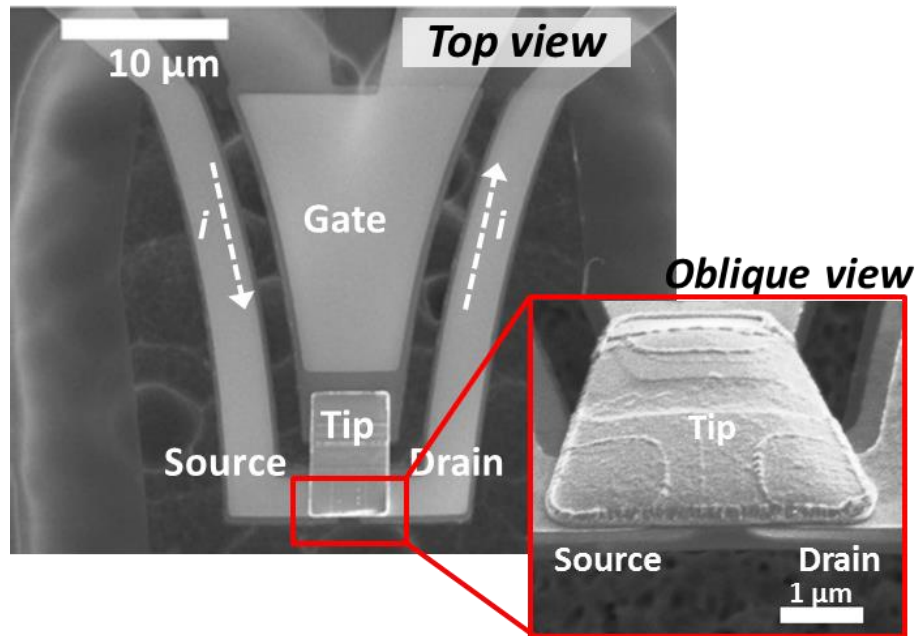


FIGURE 6: Electron micrograph of a prototype piezoelectrically-actuated nano-electromechanical switch. Copyright 2014, with permission from IEEE. [28]

As mentioned before, the abrupt mechanical making and breaking of the electrical contact has positive implications on the power consumption of NEM switches compared to FETs [29]. The power consumption of NEM and FET switches can best be compared on a so called I-V plot that shows the source-drain current as a function of gate voltage. The NEM switch and FET I-V curves shown in Figure 7 demonstrate that both device types have entirely different I-V characteristics. An increasing gate voltage will eventually lead to source-drain current flow for both device types. The overall power consumption of NEM switches and FETs is composed of the power dissipated when the device is in its “ON” state ($V_{\text{Gate}} > 0$), called dynamic power, and the power dissipated when the device is in its “OFF” state ($V_{\text{Gate}} \leq 0$), called static or leakage power (see also Figure 2). NEM switches offer significant power savings in both dissipation types [30,31].

Leakage losses in FETs are mainly due to source-drain and gate leakage, which become more prominent as the devices are scaled down in dimension [29]. Scaling of FETs in order to follow Moore's Law leads to shorter and thinner oxide gates and channels that are more prone to current leakage. The leakage through the thin gate oxide is thereby the dominating loss mechanism and continues to increase as device scaling continues [9]. Figure 7 illustrates this standby leakage in FETs through a non-zero current when no gate voltage is applied. Subthreshold leakage losses currently represent more than 50% of the total microprocessor power consumption [29] and leakage currents of more than 1 nA/FET were typical for the 250 nm technology node [32]. Piazza *et al.* demonstrated NEM switches with leakage values of less than 10 fA – more than five order of magnitude lower than the leakage in FETs [33]. The main reason for the superior leakage performance of NEM switches is their air gap between source and drain in the “OFF” state, which serves as an ideal insulator as long as it is larger than >2 nm to avoid electron tunneling [5]. The present air gap in mechanical switches and, in the case for piezoelectrically-actuated switches, less leaky gate materials lead to near-zero leakage currents.

Besides significantly lower leakage power values, NEM switches also offer a much lower dynamic power consumption than FETs. Figure 7 shows the subthreshold slope. An important quantity to characterize NEM switches and FETs is the subthreshold swing, which is equal to the inverse of the I-V curve slope, and corresponds to the voltage needed to achieve a decade change in source-drain current [32]. Low subthreshold swings confer low turn-on voltages that ultimately lead to low dynamic power consumption values. The subthreshold swing in FETs is fundamentally limited due to its electron drift and diffusion-based operating mechanism to 60 mV/dec [33].

Current FETs show subthreshold swing values in the range of 70-100 mV/dec [29,32], which corresponds to turn on voltages of 0.3-1 V [34]. The prototype NEM switch shown in Figure 6 demonstrated a NEM switch record low subthreshold swing of 0.013 mV/dec (switching energy of 23 aJ) [28], whereas other NEM switches show subthreshold slopes of 0.03-2 mV/dec [4,20,33]. These, almost four orders of magnitude lower, subthreshold swings lead to actuation voltages of just a few mV [21,28].

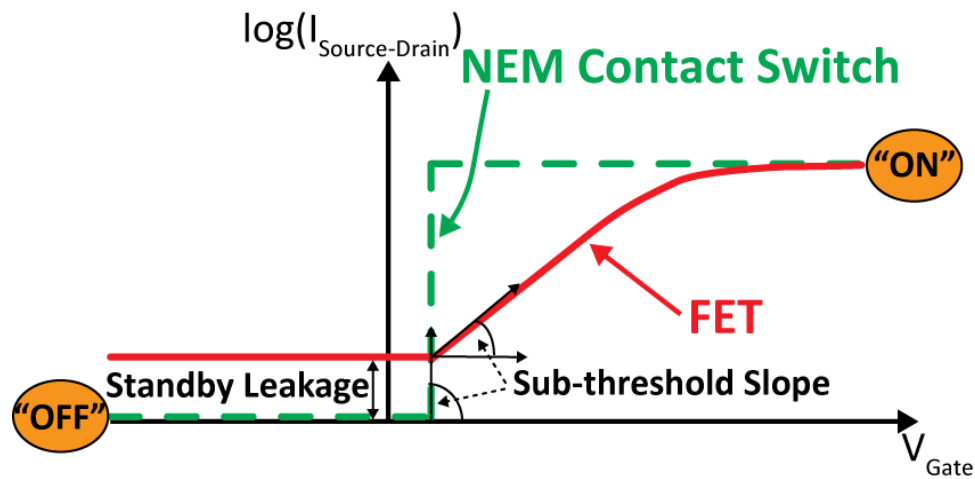


FIGURE 7: Schematic comparison of the current vs. voltage characteristics of field effect transistors and nanoelectromechanical switches.

Next to their up to five orders of magnitude lower power consumption, NEM switches offer additional advantages over FETs. The application space of FETs is drastically limited due to the sensitivity of the semiconductor doping to elevated temperatures ($T > 400\text{ }^{\circ}\text{C}$). NEM switches do not rely on doping and are unaffected by elevated temperatures, which opens up applications at temperature as high as $800\text{ }^{\circ}\text{C}$ [35]. NEM switches are also unaffected by radiation [2,36] and external electric fields

[37] due to their air gap, making them attractive for military-based application [2,36]. Besides their application in logic, NEM switches can also be utilized as nonvolatile memory, if the adhesion between the electrical contacts is carefully optimized to achieve permanently stuck contacts that can reversibly be opened [1].

1.3 Reliability issues in nanoscale electrical contacts

Despite the aforementioned benefits of NEM switch technology, electrical contact material-mediated failure mechanisms currently limit its commercial viability [5]. In particular, the operational reliability is severely limited and currently constitutes the Achilles heel of NEM switches. Figure 8 shows a performance evaluation of NEM switch technology made by the semiconductor industry in their 2009 ITRS report [1]. It can be seen that this evaluation points to the operational reliability as the area of greatest weakness, whereas the operational temperature and energy efficiency serve as the greatest strengths of NEM switches.

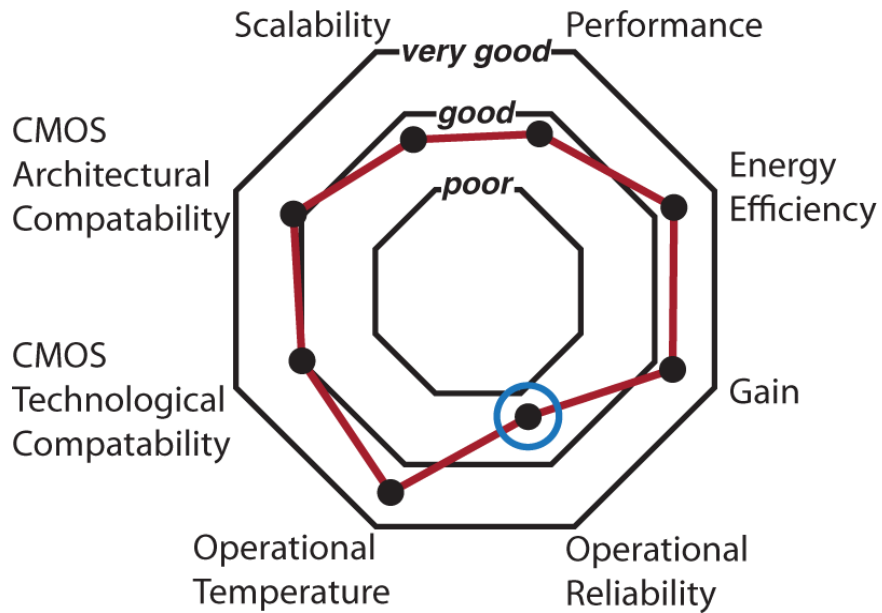


FIGURE 8: Performance evaluation of a NEM switch. Adapted from the International Roadmap of the Semiconductor Industry (ITRS).

The insufficient operational reliability in NEM switches is a consequence of the extreme environment present in their switching interface. Figure 9 summarizes the acting environment and important contact material properties. The complex interplay between the applied bias V that leads to high current densities in the contact, the contact force F_{contact} that creates high stresses, and relative humidity RH and atmosphere creates a complicated switch environment. This leads to stringent requirements on contact material properties like thermal and electrical conductivity (σ_{thermal} , $\sigma_{\text{electrical}}$), surface energy (γ_{adh}), surface roughness (Ra), as well as hardness (H) and modulus (E).

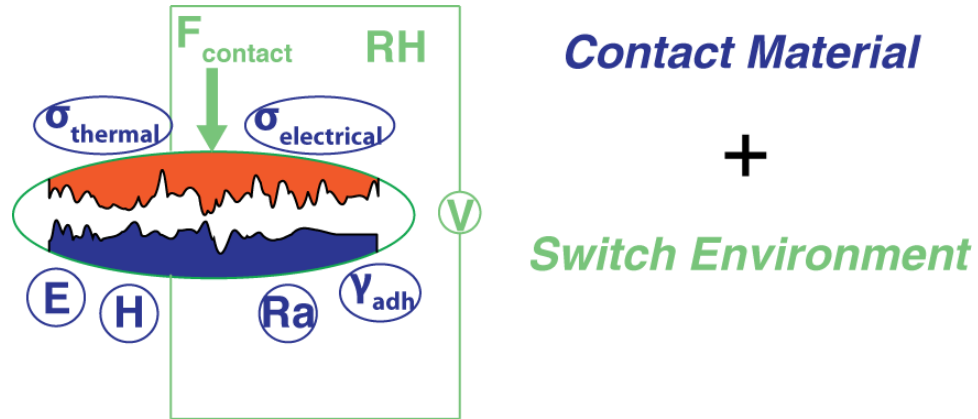


FIGURE 9: Schematic illustrating the complex environment and acting stresses at the NEM switch contact interface.

Reliability concerns for NEM contact switches arise from two primary failure mechanisms that are commonly observed in microscale switches [38-46]: device stiction, and contamination/tribopolymer formation. Device stiction, which occurs when the adhesive force between the switch contacts exceeds the restoring force available to open the contact, has been observed for soft [39], low melting point, highly adhesive, and/or miscible [38,40] contact interfaces such as Au-Au or Au-Pt [38,39,41]. The adhesive interactions often increase over the switch lifetime due to surface deformations that increase contact areas [42]. Therefore, contact materials should have a high hardness and elastic modulus.

Figure 10 shows the adhesive failure in an Au-coated microswitch. Stiction between the top and bottom contact led to a permanently closed switch upon which Czaplewski *et al.* forcefully separated the top and bottom contact [44]. The Au coating thereby partially transferred from the top to the bottom contacted indicating the strength of the adhesive bond. The susceptibility of NEM switches to adhesive failure is strongly dependent on the used actuation method. Electrostatically-actuated switches are far

more susceptible to adhesive failure than piezoelectrically-actuated switches. This is a consequence of the active opening method offered in piezoelectric NEM switches upon reversing the actuation voltage. Electrostatic NEM switches in contrast, entirely rely on the inherent restoring force of the beam upon removal of the actuation voltage.

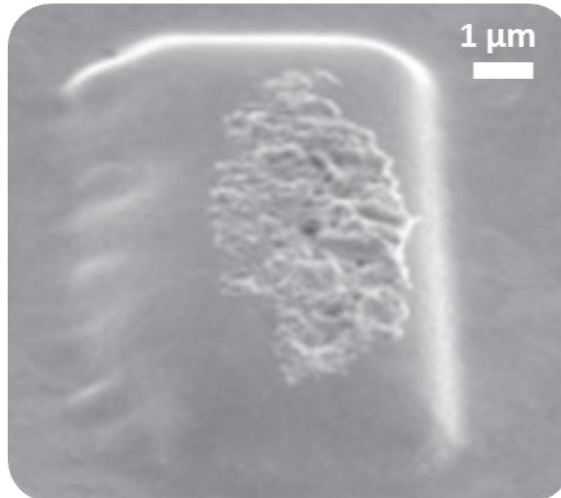


FIGURE 10: Adhesive failure in Au-Au microcontacts. Part of the top Au coating is permanently stuck to the bottom contact bump. [44] © IOP Publishing. Reproduced with permission. All rights reserved.

Contamination/tribopolymer formation, which increases the contact resistance with continued cycling, results from mechanochemically-induced growth of insulating material at contact interfaces [43,44]. Tribopolymer formation has been observed even for unreactive noble metal contacts such as Pt, Ru, and Ir [45,46,47] and has been correlated with the cleanliness of the environment surrounding the contact [43].

In an early comprehensive study of tribopolymer formation, Hermance and Egan found that hydrocarbon concentrations in 1 atm at 5 ppm were sufficient for insulating

tribopolymer buildup on macroscopic precious metal contacts [48]. Figure 11 shows the experimental setup and formed tribopolymer from Hermance & Egan's work. The authors compared the susceptibility of different macroscale contact material pairings (Pt-Pt, Pd-Pd, Ru-Ru, Ta-Ta and various alloys) to tribopolymer formation in varying hydrocarbon-containing atmospheres. They found that Pt-Pt forms the largest amount of "mysterious brown deposit" compared to the other contact pairings. However, many other pairs, including Pd-Pd, showed problematic levels of tribopolymer buildup. The researchers suspect that the organic material is formed by chemisorption of the organic vapor onto the metal, followed by "frictional activation and polymerization of the chemisorbed layers" to form an organic, polymer-like contaminant. This work is the oldest reported study on tribopolymer formation in electro-mechanical contacts and had important implications on future technologies. Reed switches [49], which are macroscale electro-mechanical switches actuated through an applied magnetic field, operate in hermetically sealed environments to protect their Pd, Ru, or Rh contacts from forming organic contaminants as seen in Hermance & Egan's study.

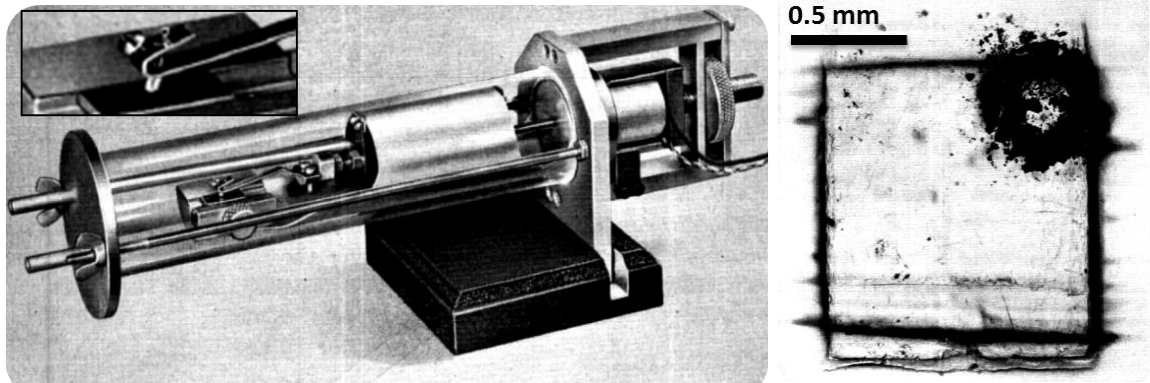


FIGURE 11: Tribopolymer formation in historic telephone contacts [48]. Left: experimental setup of telephone switch operated in glass tube of controlled atmosphere. Inset shows zoomed-in contact region. Right: top view of tribopolymer on Pd contact after 10^6 switching cycles. Courtesy of Nokia © 1958 Nokia. All Rights Reserved.

More recent work studying contamination failure in microscale electro-mechanical contacts is shown in Figure 12. Chen *et al.* cycled a gold-ruthenium contact bump against a gold-ruthenium counter surface [47]. The contact resistance increased through the agglomeration of carbonaceous, insulating contaminants in the contact interface leading to switch failure.

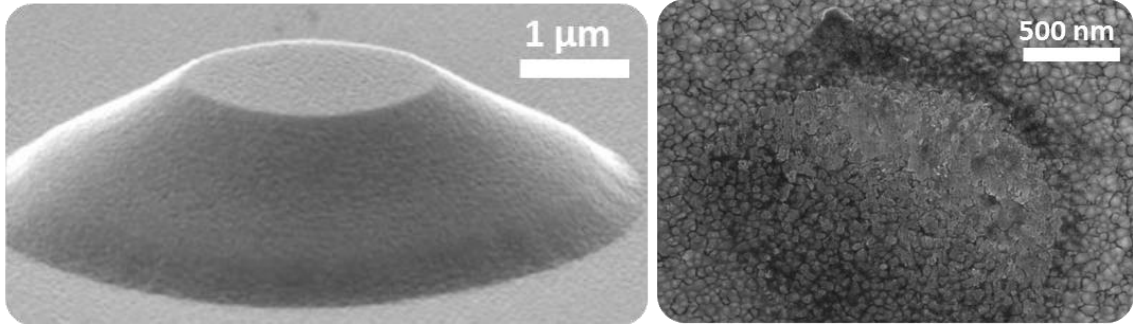


FIGURE 12: Contamination failure in AuRu_x-AuRu_x contacts [47]. Left: AuRu_x contact bump before switching. Right: AuRu_x counter surface after switch failure due to tribopolymer formation. Copyright 2007, with permission from AIP Publishing.

Other recent work concerning NEM switch reliability and contact material selection centers around titanium nitride (TiN) as contact material. Ramezani *et al.* studied silicon-germanium-based (SiGe) NEM switches and found that TiN coating of the bottom electrical contact greatly enhanced the lifetime of their devices [50]. The formed dissimilar SiGe-TiN contacts lasted for $>10^{10}$ cycles in vacuum while offering low contact resistance values due to the conductive nature of the TiN. Jang *et al.* studied selfmated TiN-TiN contacts in NEM switches and found that Joule heating led to a melting of the contacts, which ultimately led to adhesive failure of the device [51]. However, they found that a 8 nm thick coating of titanium oxide (TiO_x) ontop of the bottom TiN electrode completely prevented adhesve failure. Figure 13 show the switch design utilized by Jang *et al.* and a electron microscopy cross-section indicating the TiO_x-coated bottom contact [51]. It is of high importance that the TiO_x coating is sufficiently thin to allow for electron tunneling, otherwise high contact resistances hinder the applicability of this method. TiO_x coated contacts were also utilized by Tsu-Jae King Liu and coworkers [52].

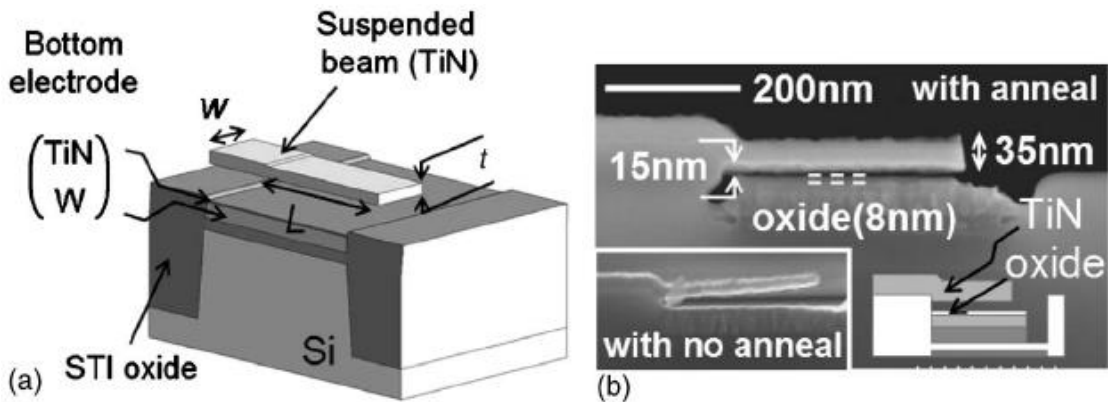


FIGURE 13: a) Schematic of NEM switch design utilized by Jang *et al.* and b) electron microscopy cross-section of the NEM switch indicating the TiO_x -coated bottom contact [51]. Copyright 2008, with permission from AIP Publishing.

Finally, amorphous carbon (*a*-C) as contact material has been studied by researchers from IBM Zurich [53]. They coated top and bottom contact of a curved NEM switch with 10 nm *a*-C and achieved 10^8 contact cycles without noticeable degradation. Low surface energy and excellent wear resistance motivate the use of *a*-C. Additionally, low contact resistances can be achieved through the formation of highly localized conducting filaments in the *a*-C through Joule heating-induced clustering of sp^2 C atoms within the sp^3 matrix [53,54]. The main disadvantage is the high voltage (>2 V) necessary to form the conducting filament within *a*-C, which conflicts with the low power consumption of NEM switches.

The failure mechanisms presented throughout this section are exacerbated in NEM switches, where low contact and restoring forces required for reliable operation (10^{16} contact cycles are desirable [1]) may be insufficient to penetrate adsorbed films or to separate adhesive contacts. Thus, both stiction and tribopolymer formation constitute

principle challenges for NEM switch commercialization and call for developing new materials with reliably low contact resistance, low adhesion, high hardness and elastic modulus, and resistance to tribofilm formation [47].

BIBLIOGRAPHY CHAPTER 1

- [1] "International technology roadmap for semiconductors (2009 edition)," 2009.
- [2] Blick, R. H.; Qin, H.; Kim, H.-S.; Marsland, R. *New J. Phys.* **2007**, 9, 241.
- [3] Czaplewski, D. A.; Patrizi, G. A.; Kraus, G. M.; Wendt, J. R.; Nordquist, C. D.; Wolfley, S. L.; Baker, M. S.; de Boer, M. P. *J. Micromech. Microeng.*, **2009**, 19, 085003.
- [4] Loh, O. Y.; Espinosa, H. D. *Nat. Nanotech.* **2012**, 7, 283–295.
- [5] "International technology roadmap for semiconductors (2011 edition)." 2011.
- [6] Moore, G. E. *Proc. IEEE* **1998**, 86, 82–85.
- [7] Calhoun, B. *Proc. IEEE* **2008**, 96, 343–365.
- [8] "Building energy-efficient ICs from the ground up," Cadence Design Systems, White paper, 2011.
- [9] Borkar, S. "Exponential challenges, exponential rewards - The future of moore's law," in *Proceedings of the VLSI-SOC*, Darmstadt, Germany, 2003.
- [10] Kim, N. S.; Austin, T.; Baauw, D.; Mudge, T.; Flautner, K.; Hu, J. S.; Irwin, M. J.; Kandemir, M.; Narayanan, V. *Computer* **2003**, 36, 68–75.
- [11] Hutchby, J. A.; Bourianoff, G. I.; Zhirnov, V. V.; Brewer, J. E. *IEEE Circuits and Devices Magazine* **2002**, 18, 28–41.
- [12] International Energy Agency and Organisation for Economic Co-operation and Development, *Gadgets and gigawatts: policies for energy efficient electronics*. Paris: OECD/IEA, 2009.
- [13] Climatewire, J. M. "Soaring electricity use by new electronic devices imperils climate change efforts," *The New York Times*, 14-May-2009.
- [14] Koomey, J. G. "Estimating total power consumption by servers in the US and the world," Oakland, CA, 2007.
- [15] Najm, F. N. *IEEE Trans. Very Large Scale Integr. VLSI Syst.* **1994**, 2, 446–455.
- [16] Nathanael, R.; Pott, V.; Kam, H.; Jeon, J.; King Liu, T.-J. "4-terminal relay technology for complementary logic," in *2009 IEEE International Electron Devices Meeting (IEDM 2009)*, Piscataway, NJ, USA, 2009.
- [17] Tabib-Azar, M.; Venumbaka, S. R.; Alzoubi, K.; Saab, D. "1 volt, 1 GHz NEMS switches," presented at the IEEE Sensors, 2010, pp. 1424–1426.
- [18] Jang, W. W.; Yoon, J.-B.; Kim, M.-S.; Lee, J.-M.; Kim, S.-M.; Yoon, E.-J.; Cho, K. H.; Lee, S.-Y.; Choi, I.-H.; Kim, D.-W.; Park, D. *Solid-State Electron.* **2008**, 52, 1578–1583.
- [19] Sinha, N.; Wabiszewski, G. E.; Mahameed, R.; Felmetsger, V. V.; Tanner, S. M.; Carpick, R. W.; Piazza, G. *Appl. Phys. Lett.* **2009**, 95, 053106.

- [20] Piazza, G. "Alumimun nitride piezoelectric NEMS resonators and switches," in *Proc. SPIE 7679, Micro- and Nanotechnology Sensors, Systems, and Applications II*, Orlando, FL, USA, 2010, p. 76791L–76791L.
- [21] Zaghoul U.; Piazza, G. "10 - 25 nm piezoelectric nano-actuators and NEMS switches for millivolt computational logic," in *IEEE 26th International Conference on Micro Electro Mechanical Systems (MEMS)*, Taipei, Taiwan, 2013, pp. 233–236.
- [22] Pott, V.; Chua, G. L.; Vaddi, R.; Tsai, J. M.-L.; Kim, T. T. *IEEE Trans. Electron Devices* **2012**, *59*, 1137–1143.
- [23] Li, Q.; Koo, S.-M.; Edelstein, M. D.; Suehle, J. S.; Richter, C. A. *Nanotechnology* **2007**, *18*, 315202.
- [24] Cha, S. N.; Jang, J. E.; Choi, Y.; Amaratunga, G. A. J.; Kang, D.-J.; Hasko, D. G.; Jung, J. E.; Kim, J. M. *Appl. Phys. Lett.* **2005**, *86*, 083105.
- [25] Lee, S. W.; Lee, D. S.; Morjan, R. E.; Jhang, S. H.; Sveningsson, M.; Nerushev, O. A.; Park, Y. W.; Campbell, E. E. B. *Nano Lett.* **2004**, *4*, 2027–2030.
- [26] Loh, O.; Wei, X.; Ke, C.; Sullivan, J.; Espinosa, H. D. *Small* **2011**, *7*, 79–86.
- [27] Kim, S. M.; Song, E. B.; Lee, S.; Seo, S.; Seo, D. H.; Hwang, Y.; Candler, R.; Wang, K. L. *Appl. Phys. Lett.* **2011**, *99*, 023103.
- [28] Zahloul, U.; Piazza, G. *IEEE Electron Device Lett.* **2014**, *35*, 669–671.
- [29] Dadgour H. F.; Banerjee, K. *IET Computers & Digital Techniques* **2009**, *3*, 593.
- [30] Akarvardar, K.; Elata, D.; Parsa, R.; Wan, G. C.; Yoo, K.; Provine, J.; Peumans, P.; Howe, R. T.; Wong, H.-S. "Design considerations for complementary nanoelectromechanical logic gates," in *Electron Devices Meeting, 2007. IEEE International*, 2007, pp. 299–302.
- [31] Ionescu, A. M.; Pott, V.; Fritschi, R.; Banerjee, K.; Declercq, M. J.; Renaud, P.; Hibert, C.; Fluckiger, P.; Racine, G. A. "Modeling and design of a low-voltage SOI suspended-gate MOSFET (SG-MOSFET) with a metal-over-gate architecture," in *Quality Electronic Design, 2002. Proceedings. International Symposium on*, 2002, pp. 496–501.
- [32] Fallah F.; Pedram, M. *IEICE Transactions on Electronics* **2005**, *E88–C*, 509–519.
- [33] Sinha, N.; Jones, T. S.; Guo, Z.; Piazza, G. *J. Microelectromech. Syst.* **2012**, *21*, 484–496.
- [34] Yablonovitch, E. "There are orders-of-magnitude power advantages in complementing the transistor with a milli-volt switch," presented at the MTO Symposium, San Jose, CA, USA, 07-Mar-2007.
- [35] Lee, T.-H.; Bhunia, S.; Mehregany, M. *Science* **2010**, *329*, 1316–1318.
- [36] S.-W. Lee, R. W. Johnstone, and A. M. Parameswaran, "MEMS mechanical logic units: characterization and improvements of devices fabricated with MicraGEM and PolyMUMPs," in *Proceedings of SPIE 2005*, p. 60371A–60371A–10.

- [37] Lovellette, M. N.; Campbell, A. B.; Hughes, H. L.; Lawrence, R. K.; Ward, J. W.; Meinhold, M.; Bengtson, T. R.; Carleton, G. F.; Segal, B. M.; Rueckes, T. presented at AEROSP CONF PROC, Big Sky, Montana, USA (March, **2004**)
- [38] Coutu, R. A.; Kladitis, P. E.; Leedy, K. D.; Crane, R. L. *J. Micromech. Microeng.* **2004**, *14*, 1157.
- [39] Yang, Z.; Lichtenwalner, D. J.; Morris, A. S.; Krim, J.; Kingon, A. I. *J. Microelectromech. Syst.* **2009**, *18*, 287.
- [40] Kam, H.; Alon, E.; Liu, T.-J. K. presented at INT EL DEVICES MEET, San Francisco, California, USA (December, 2010).
- [41] Gilbert, K. W.; Mall, S.; Leedy, K. D. *J. Adhes. Sci. Technol.* **2010**, *24*, 2597.
- [42] Brown, C.; Rezvanian, O.; Zikry, M. A.; Krim, J. *J. Micromech. Microeng.* **2009**, *19*, 025006.
- [43] Brand, V.; Baker, M. S.; de Boer, M. P. *Tribol. Lett.* **2013**, *51*, 341.
- [44] Czaplewski, D. A.; Nordquist, C. D.; Dyck, C. W.; Patrizi, G. A.; Kraus, G. M.; Cowan, W. D. *J. Micromech. Microeng.* **2012**, *22*, 105005.
- [45] Lee, H.; Coutu, R. A.; Mall, S.; Leedy, K. D. *J. Micromech. Microeng.* **2006**, *16*, 557.
- [46] Kwon, H.; Choi, D. J.; Park, J. H.; Lee, H. C.; Park, Y. H.; Kim, Y. D.; Nam, H. J.; Joo, Y. C.; Bu, J. U. presented at PROC IEEE MICR ELECT, Hyogo, Japan (January, 2007).
- [47] Chen, L.; Lee, H.; Guo, Z. J.; McGruer, N. E.; Gilbert, K. W.; Mall, S.; Leedy, K. D.; Adams, G. G.; *J. Appl. Phys.* **2007**, *102*, 074910.
- [48] Hermance, H. W.; Egan, T. F. *Bell Syst. Tech. J.* **1958**, *37*, 739.
- [49] Hinohara, K. in *Electrical Contacts: Principles and Applications*, Edt. Slade, P. G. Marcel Dekker Inc.: New York, 1999.
- [50] Ramezani, M.; Severi, S.; Moussa, A.; Osman, H.; Tilmans, H. A. C.; De Meyer, K. "Contact Reliability Improvement of a Poly-SiGe Based Nano-Relay with Titanium Nitride Coating," in *IEEE Transducers 2015*, Anchorage, AK, 2015, pp. 576-579.
- [51] Jang, W. W.; Lee, J. O.; Yoon, J.-B.; Kim, M.-S.; Lee, J.-M.; Kim, S.-M.; Cho, K.-H.; Kim, D.-W.; Park, D.; Lee, W.-S. *Appl. Phys. Lett.* **2008**, *92*, 103110.
- [52] Kam, H.; Chen, Y.; Liu, T. J. K. "Reliable micro-electro-mechanical (MEM) switch design for ultra-low-power logic," in *Reliability Physics Symposium (IRPS), 2013 IEEE International*, Anaheim, CA, 2013, pp. 6A.1.1-6A.1.5.
- [52] Grogg, D.; Ayala, C. L.; Drechsler, U.; Sebastian, A.; Koelmans, W. W.; Bleiker, S. J.; Fernandez-Bolanos, M.; Hagleitner, C.; Despot, M.; Duerig, U. T. "Amorphous Carbon Active Contact Layer for Reliable Nanoelectromechanical Switches," in *MEMS 2014*, San Francisco, CA, 2014, pp. 143-146.
- [53] Sebastian, A.; Pauza, A.; Rossel, C.; Shelby, R. M.; Rodriguez, A. F.; Pozidis, H.; Eleftheriou, E. *New J. Phys.* **2011**, *13*, 013020.

CHAPTER 2: ASSESSMENT OF NANOELECTROMECHANICAL SWITCH-LIKE CONTACTS USING ATOMIC FORCE MICROSCOPY¹

This chapter describes the use of atomic force microscopy (AFM) to assess the reliability of nanoscale electrical contacts with applications in nanoelectromechanical switches. First, conducting atomic force microscopy and the deposition of different AFM probe materials are described. Second, a protocol to assess the reliability of nanoscale electrical contacts up to 10^9 interaction cycles is presented. Third, a modified test methodology to achieve better force control and continuous contact resistance and adhesion data is introduced and results for Pt-Pt nanocontacts are presented.

2.1 Atomic force microscopy to assess nanoscale electrical contact reliability

Atomic force microscopy (AFM) is a widespread surface analyses method that is typically used for high precision measurements of the surface topography and quantification of the surface adhesion or friction force of nanoscale contacts. In this thesis, electrical measurements using an AFM setup are performed to quantify the contact resistance of nanoscale electrical contacts.

2.1.1 Electrical atomic force microscopy

Existing electrical contact materials testing methods are insufficient to efficiently screen potential nanoscale NEM switch electrical contact materials. Electrical contact

¹ Parts of this chapter appear in print: Adapted with permission from Streller, F. *et al.*, *IEEE Nanotechnol. Mag.* **2015**, 9, 18–24. (Copyright 2015 IEEE).

lifetime testing has been previously achieved using modified scanning probe setups [1], nanoindentors [2], or full fabrication of switches [3,4]. These methods are typically low-throughput, costly, difficult to implement without specialized hardware, and often do not reveal the adhesiveness of the contacts – a characteristic of NEM switch contacts that can have a large impact on device longevity and power consumption. Here, we present two distinct methods to cycle single asperity electrical contacts – the fundamental unit of contact in a NEM switch – using AFM, for up to two billion contact cycles in laboratory time frames (12-18 hours). These high throughput cycling methods may be used to efficiently interrogate any thin-film contact material under NEM switch-like conditions, can be used to quantify the mechanical and electrical characteristics of electrical contacts, and could be widely adopted due to the ubiquity of the instrumentation.

The operation principle of an AFM lies in the registration of the interactions of a nanoscale tip with a counter surface commonly referred to as the sample (note: although we are studying the electrical properties of nanocontacts, standard AFM does not require conductive samples – in contrast to scanning tunneling microscopy). AFM is able to record the surface topography of the sample and the surface forces between the tip and sample with sub-nm and sub-nN precision, respectively. AFMs are comprised of four main constituents: a) a nanofabricated, flexible cantilever with a nanoscale tip at the end (radius typically <100 nm), b) a laser or photoluminescent diode, c) a quadrant photodetector, and d) a piezoelectric scanner. Figure 14 shows a schematic of the electrical or conductive AFM (C-AFM) setup used in this thesis. A C-AFM setup adds a voltage source, series resistor and current amplifier to a standard AFM setup to enable electrical characterization of the tip-sample contact.

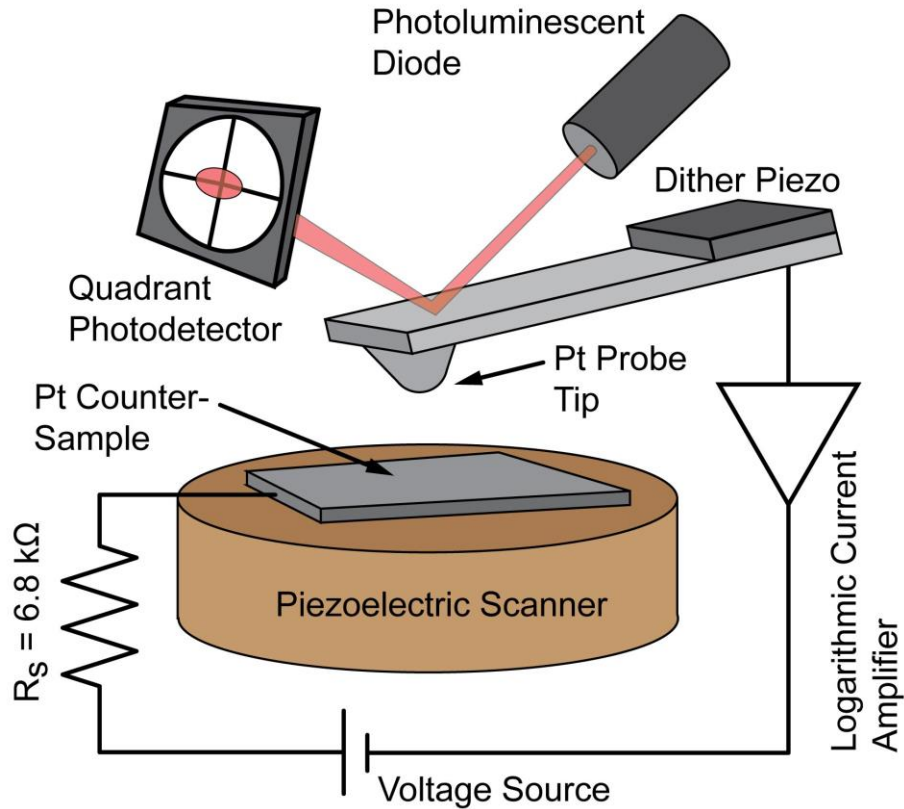


FIGURE 14: Schematic of the AFM-based test setup used to interrogate NEM switch contact materials. The tip and sample are coated with candidate films, and testing is then carried out under desired environments and testing conditions.

The forces between tip and sample are detected through the nanofabricated, flexible cantilever. These cantilevers are typically fabricated out of *sc*-Si using typical microfabrication techniques and culminate in tip radii of several tens of nm. The interaction of the tip and the sample causes the cantilever to bend. A laser or luminescent diode is focused onto the end of the cantilever, in the area where the tip is located, and from there reflected into a position-sensitive, quadrant photodetector. The photodetector can precisely sense flexural bending of the cantilever caused by normal loading as well as torsion of the cantilever due to the frictional forces created by sliding

of the tip on the sample. Finally, the relative motion between the tip and sample is achieved through a piezoelectric scanner. Three dimensional movement with nanoscale precision enables the tip to interact in different ways with the sample, *i.e.* laterally scanning over the sample to measure its topography and the resulting frictional interactions or vertically moving in and out of contact (called “force-distance”, FD, measurements) to measure the adhesive interaction between tip and sample. Under an applied voltage, these two interaction schemes, both used in this work, produce two dimensional contact resistance maps accompanied by topography maps and contact resistance values at a specific location accompanied by the adhesion force, respectively. The applied DC voltage across the tip and sample produces current flow that was recorded using a current-voltage amplifier. A series resistor, R_s , was utilized to limit the current flow through the tip-sample contact in order to prevent vaporization or melting of the tip. R_s was subtracted from all quoted contact resistance values in this thesis.

The measured contact resistance from this setup is a combination of the series resistance, R_s , the constriction resistance, $R_{\text{constriction}}$, which is due to the nanoscale geometry of the AFM tip and the roughness of the sample, as well as the contaminant resistance, $R_{\text{contaminant}}$, due to the presence of insulating films in the tip-sample contact (note: other resistances originating from electrical connections within the C-AFM setup can be ignored due to their comparatively low values).

Another essential component of the AFM setup is a controller that provides feedback on the position of the probe to the piezoelectric scanner and photodetector. The feedback parameter the controller uses can be specified by the user and is typically the load. After selecting a load and calibrating the cantilever (defining the relationship

between load and photodetector voltage), the controller varies the piezoelectric scanner to modulate the tip-sample interactions to account for the present surface topography.

In order to determine the interaction forces between tip and sample, knowledge of the AFM cantilever stiffness and displacement is needed. The tip-sample contact is thereby treated as a linear spring and the interaction force is the product of cantilever stiffness and deflection. The cantilever stiffness was determined using the Sader method [5], which measures the hydrodynamic response of a cantilever to determine its normal stiffness. The exact dimensions of the cantilever need to be known in order to perform this method. The length and width of each cantilever used in this work was measured using a Zygo New View 3100 white light interferometer (Zygo Corporation, Middlefield, CT, United States). The displacement of the cantilever is measured by the photodetector and reported in units of volts. It is therefore important to relate the voltage output from the photodetector to physical units through the deflection sensitivity S (units: nm/V). The deflection sensitivity values in this work were extracted from the loading portion of an FD measurement (as shown in Figure 19).

2.1.2 Depositing electrical contact materials onto atomic force microscopy probes

In order to effectively utilize AFM-based nanocontact reliability tests for NEM switch contact material development, candidate materials need to be available on AFM probes. Commercial AFM probe materials are mostly limited to Si, SiO₂, SiN, Pt, Ir, Au, ultrananocrystalline diamond, and diamond-like carbon of specific, vendor-determined coating thicknesses. This motivates the development of deposition methods to coat commercial *sc*-Si AFM probes with various contact material candidates.

We developed a holder for coating of AFM probe chips for use in a Denton Vacuum Explorer 14 sputterer (Denton Vacuum Inc, Moorestown, NJ). Sputtering is a physical vapor deposition method that provides good coating conformity as it is needed for the coating of high aspect ratio AFM probes. The Explorer 14 system features a rotating turntable and top-down sputtering that necessitates a stable position for the AFM probes that need to be coated. Since AFM cantilevers easily break if handled incorrectly, it is very important to ensure a safe position of the AFM probe chips during the coating process as well as an easy loading and unloading process. Additionally, it is desirable to coat the front and backside of the AFM chip, to minimize stress effects of the coating on the cantilever. If a coating has high internal stresses, the cantilever can deform to a point that makes its use in AFM impossible. The probe holder must therefore be able to provide a way to easily flip the AFM probe chip from the front to the back side for further coating. The developed probe holder is able to accommodate the aforementioned constraints for a variety of different commercially available host probes. Figure 15 shows a SolidWorks (Dassault Systemes SE, Velizy-Villacoublay, France) drawing of the designed AFM probe chip holder including a loaded example AFM probe chip.

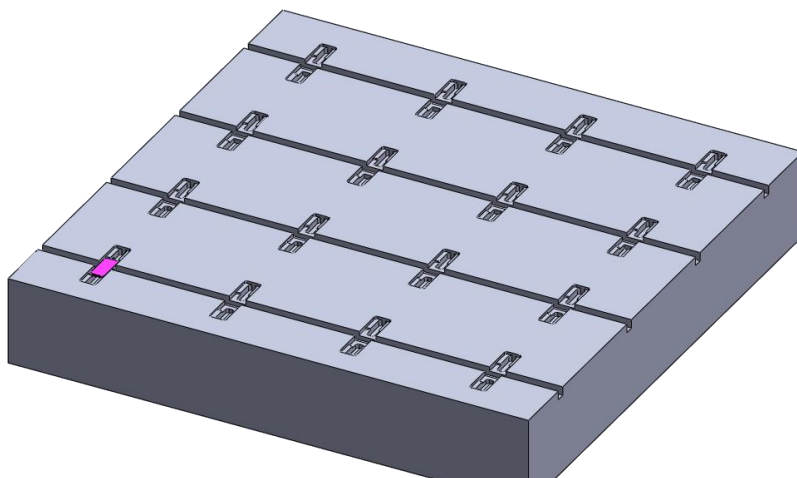


FIGURE 15: Schematic of a SolidWorks drawing of the AFM probe holder for coating inside a sputtering system. The holder can host 16 AFM probe chips and protects the cantilever from damage during the coating process, as well as enables easy flipping of the chips to enable backside coating. A loaded AFM probe chip is shown in magenta.

A total of 16 AFM probe chips can be placed on the designed holder, which protects the cantilevers from damage during the loading, coating, and unloading process. Additionally, grooves enable easy flipping of the AFM probe chips to enable a backside coating. Three of such holders were fabricated from aluminum and tested. Figure 16 shows two fully-loaded (16 AFM probe chips each) AFM probe chip holders placed on top of the Explorer 14 sputtering system turntable. Two half-wafer witness samples are placed adjacent to the holders and enable the characterization of the deposition thickness and composition.

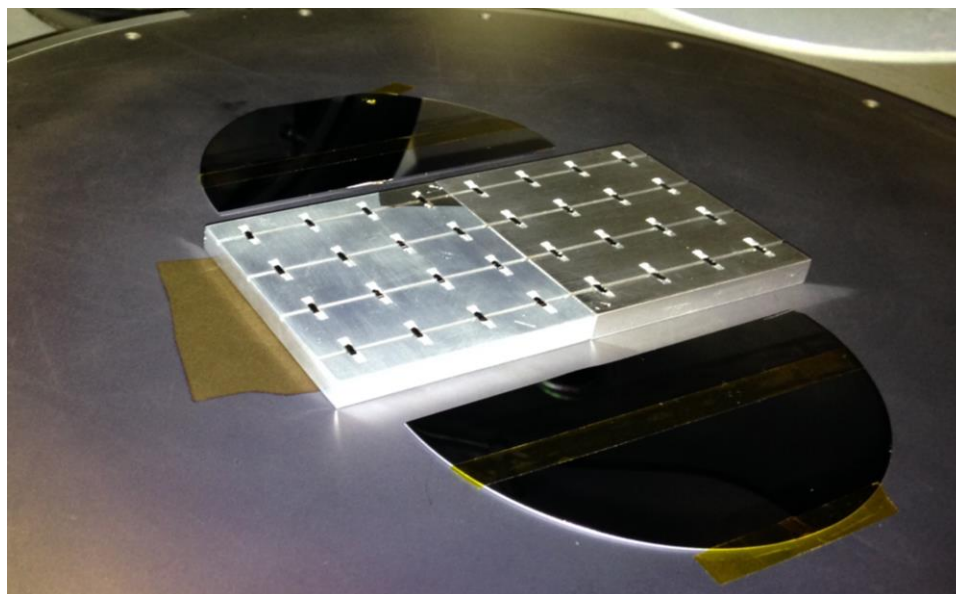


FIGURE 16: Image of two AFM probe chip holders (with 16 AFM probe chips each) loaded onto the Explorer 14 sputterer turntable, together with two half-wafer witness samples.

In addition to simply depositing materials onto an AFM probe, heating of such AFM probes is necessary for specific contact material candidates that are formed through solid-state diffusion reactions. Loading AFM probe chips into rapid thermal annealing (RTA) systems (MILA-3000-P-N, ULVAC Technologies Inc., Kanagawa, Japan) requires the same precautions as previously discussed for sputter deposition. We therefore designed and fabricated a holder to securely fix AFM probe chips during a RTA treatment. Figure 17 shows a SolidWorks drawing of the RTA AFM probe chip holder including a mounted example AFM probe chip.

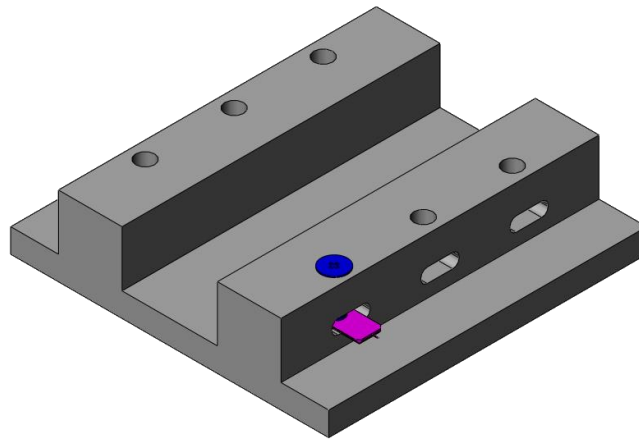


FIGURE 17: Schematic of a SolidWorks drawing of the AFM probe holder usable in a rapid thermal annealing system. The holder can host 6 AFM probe chips and protects the cantilevers from damage during the heating process. A loaded AFM probe chip is shown in magenta.

The RTA holder fixes each AFM probe chip using a screw and thereby prevents any unwanted movements during the loading, heating and unloading process that could damage the cantilever. Figure 18 shows an image of the AFM probe chip holder loaded into the RTA crucible area. The holder was fabricated from MACOR® Machinable Glass Ceramic (Corning Inc., Corning, NY), to ensure a vacuum-compatible, high temperature operation. The holder was tested to temperatures up to 600°C under both, moderate vacuum conditions ($p \approx 20$ mbar) and flowing nitrogen gas.

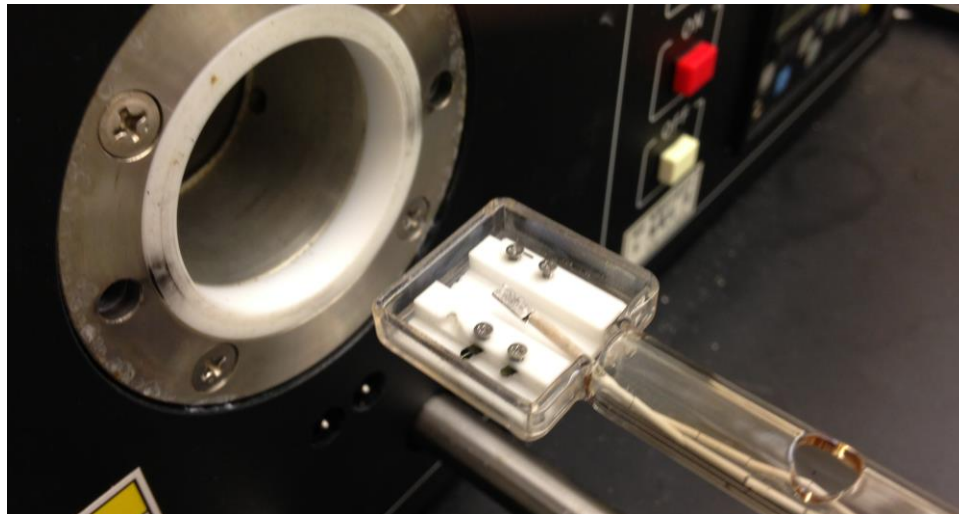


FIGURE 18: Image of the AFM probe chip holder loaded on the rapid thermal annealing crucible holder. The AFM probe chips are fixated using a screw in order to protect the cantilever from damage.

With the sputtering and RTA holder in place, a wide range of contact material candidates can be explored using AFM-based nanocontact reliability testing methods.

2.2 Gigacycle interrogation of single asperity contacts

Pt-Pt contacts were investigated to demonstrate the capability of this AFM-based cycling technique. This material set was chosen since its behavior in microscale, multiasperity tests has been previously investigated [1,3,6] and its lifetime behavior is a useful baseline for comparison to novel and unproven electrical contact materials. Figure 14 shows a schematic of the single asperity electrical test setup implemented on an Asylum MFP-3D AFM (Asylum Research, Santa Barbara, CA). A commercial Si AFM probe (Nanosensors PPP-FM) and a Si wafer were coated with 70 nm of Pt and brought into repetitive contact under nanonewton applied loads.

The electrical characteristics of the contact interface were measured with a custom logarithmic amplifier having a current range of sub-nanoamperes to milliamperes. The output of the amplifier was fed into the AFM controller for synchronized measurements of interaction force and current. The AFM controller provided the adjustable DC voltage source and a current limiting safety resistor was used to prevent accidental shorting during setup.

Two modes of AFM that are commonly available on most commercial AFM systems were used to mimic single asperity electrical contact interactions as they would be encountered in a nanomechanical switch. Hard tapping mode amplitude-modulation AFM (AM-AFM) [7], in which the AFM cantilever is resonated near its natural frequency (~73 kHz for the test presented here) in proximity to the counter-surface, was used to cycle the contact in excess of a billion cycles. The use of hard-tapping mode AM-AFM ensures tip-surface contact during every oscillation of the cantilever. To simulate the contact environment of a NEM switch interface, the interface was hot-switched by continuously applying a 1 V potential between the Pt-Pt surfaces during cycling, and all tests were performed in laboratory air. The peak interaction force and stress during cycling were 114 – 137 nN and 1.8 – 2.0 GPa as determined from dynamic simulations of the physical system using the method of Garcia *et al.* [8], the electrostatic potentials of Law and Rieutord [9], and Derjaguin-Müller-Toporov (DMT) contact mechanics [10] (Note: please refer to section 2.1.5 of the PhD thesis of G. E. Wabiszewski for a discussion of the model and an example of the peak interaction force calculation [11]). The forces, stresses, and voltages used are representative of contact conditions in a NEM switch.

Meaningful electrical characterization of the contact cannot be performed during AM-AFM cycling as the cycling frequency exceeds the bandwidth of the custom-built logarithmic amplifier (176 Hz). Consequently, before cycling and at various logarithmically-spaced time points throughout cycling, AM-AFM oscillations were interrupted to perform force-distance (FD) measurements at ~2 Hz. As shown in Figure 19, these slower measurements permit high-fidelity collection of conductivity and adhesion. 1156 of these FD measurements, each loaded up to a maximum applied load of 40 nN and with a tip-surface potential of 200 mV, were performed at each interruption. These ensembles of FD measurements were necessary as the nanoscale size of the contacts and the presence of adsorbed surface contamination led to large variations in current response between single measurements.

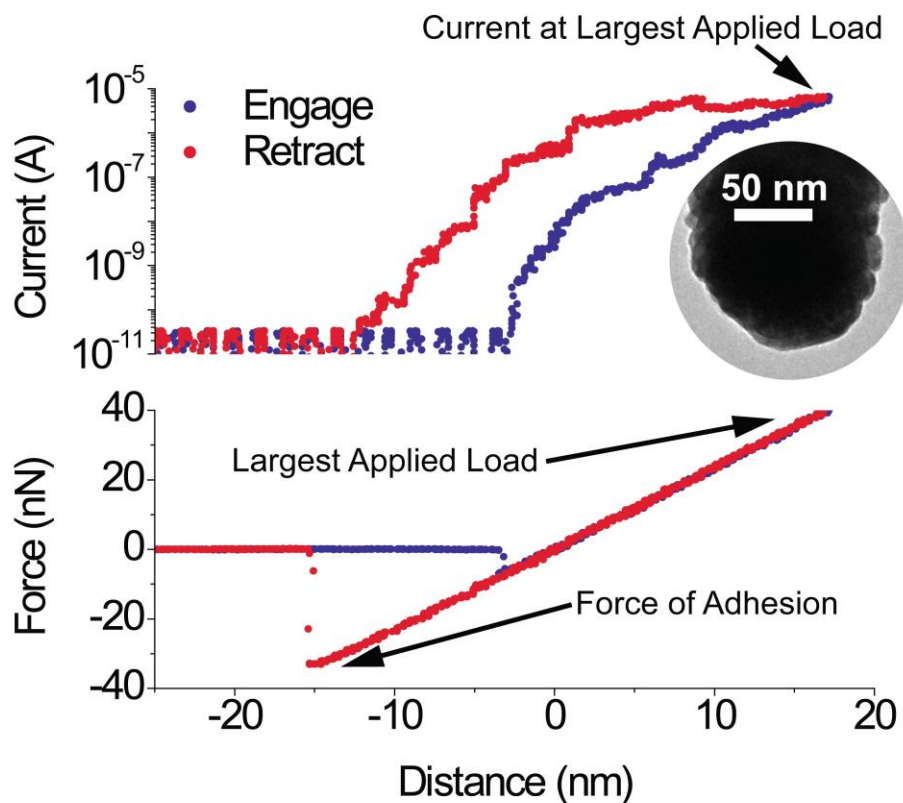


FIGURE 19: Simultaneous measurements of current and force during an AFM force-distance (FD) measurement with a 200 mV bias applied between a Pt-coated AFM probe tip and a Pt counter surface. A TEM micrograph of the probe tip used in this measurement is shown in the inset.

The electrical and adhesive lifetime behavior of the Pt-Pt interface is shown in Figure 20. Selected histograms from each set of 1156 FD measurements are shown in Figure 20A. These measurements of current are then converted to contact resistance and plotted as a function of the number of cycles in Figure 20B. Both of these plots show a dramatic decrease in Pt-Pt interface conductivity as cycling progresses: resistance after 1.5 billion cycles is more than 10,000 times the initial contact resistance. However, the force of adhesion (Figure 20C) was observed to increase only ~12% over the lifetime of

the contact. This suggests minimal variation in the geometry and the work of adhesion at the contact interface.

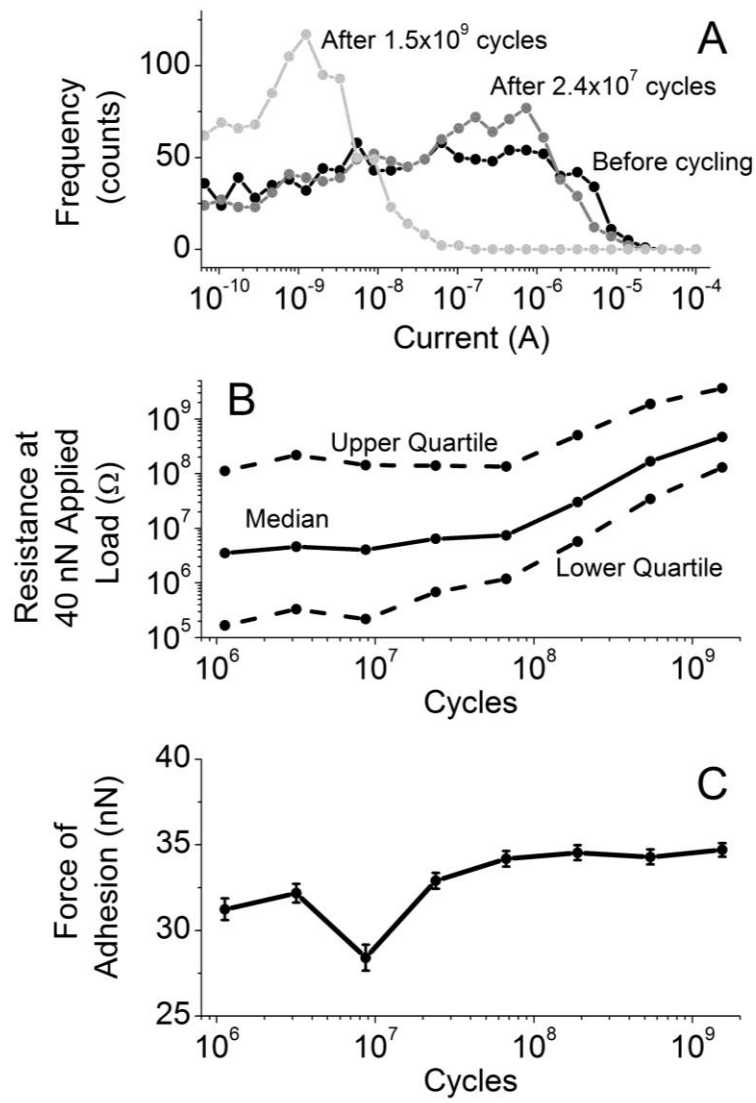


FIGURE 20: (A) 1156 force-distance measurements under 200 mV bias with simultaneous current measurements are performed before and at regular intervals throughout high-speed cycling of a nanoscale Pt-Pt interface. Histograms of the current response at maximum load (40 nN) are then produced. (B) Current measurements are converted to contact resistance and the median, lower quartile, and upper quartile values are reported as a function of the number of contact cycles. (C) The force of adhesion as a function of cycles is shown. Error bars represent the standard deviation of each ensemble of measurements.

These findings show similarities to earlier observations of electrical degradation in microscale Pt-Pt systems [3,12,13] in which the formation of insulating tribopolymers inhibit current flow through the contact. Contact stress, electrical power through the contact, and the presence of adsorbed environmental contaminants lead to the mechanochemical formation of short-chain, carbon-containing compounds [13,14]. To verify the presence of this insulating film, high-resolution transmission electron microscopy (TEM) was performed on probe tips subjected to similar testing. Figure 21 shows representative TEM images of a Pt probe taken before and after cycling for 2 billion interactions with a Pt counter-surface. An increase in contact resistance for this probe was accompanied by the emergence of a low contrast film, several nm-thick that is hypothesized to be a tribopolymer. Gross deformation or wear the probe was not observed, despite the appreciable peak contact stresses applied (1.8 – 2.0 GPa) for billions of cycles.

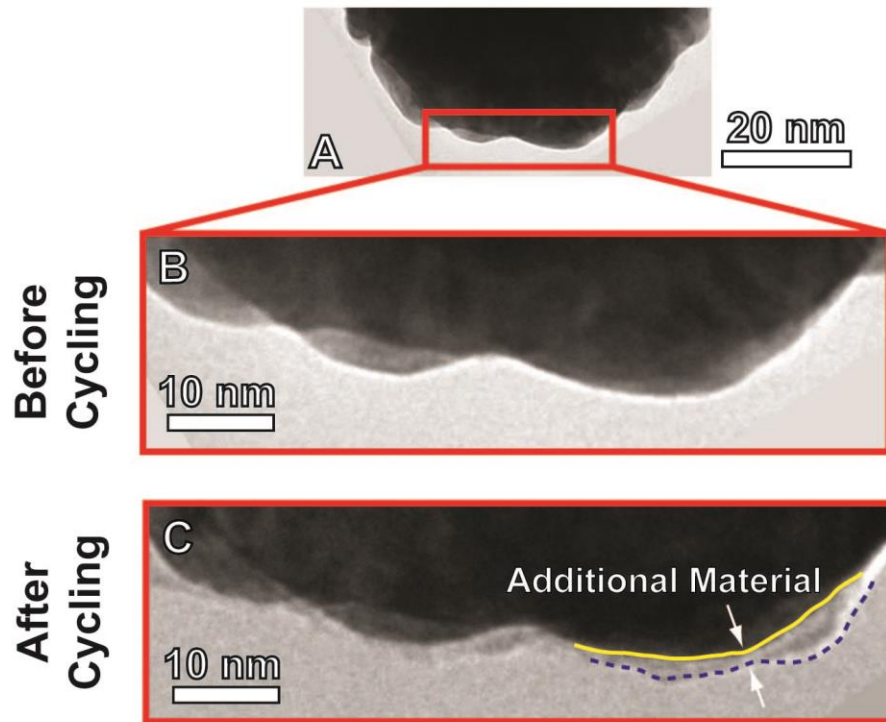


FIGURE 21: Low-resolution (A) and high resolution (B) Pt-coated AFM probe tip before cycling. (C) High resolution image of the same Pt-coated AFM probe after 2×10^9 cycles with 100 mV bias voltage shows the addition of low density material in the contact area.

The electrical contact material cycling experiments presented here demonstrate the ability to quantitatively screen the behavior of potential electrical contact materials under NEM switch-like conditions without the need for full device fabrication. This test can be implemented with minimal to no modification of most commercial AFMs setups, and only requires that the candidate materials can be deposited in thin film form on commercial AFM cantilevers.

2.3 Improved single asperity interrogation method

The single asperity interrogation method based on tapping mode amplitude-modulation AFM (AM-AFM) presented in section 2.2 can achieve billions of interaction cycles in laboratory timeframes due to its high tapping frequency of up to 73 kHz. However, the high tapping frequency prevents electrical characterization of the contact during the AM-AFM cycling experiment. In order to gain contact resistance and adhesion information, the AM-AFM cycling tests need to be interrupted at various time points to perform slow force-distance (FD) measurements. The results of this methodology are therefore contact resistance vs. cycle count and adhesion vs. cycle count plots with logarithmically-spaced data points. This lack of data density, combined with the previously described uncertainty in contact force motivates the development of a single asperity interrogation method that allows for the continuous recording of contact resistance and adhesion while having precise and direct contact force control.

2.3.1 PeakForce Tapping for continuous contact resistance measurements

PeakForce Tapping® mode can be used to achieve continuous data collection coupled with precise contact force control. PeakForce Tapping® is a proprietary AFM methodology developed by Bruker (Bruker Corporation, Billerica, MA) that operates similar to AM-AFM by avoiding lateral forces through intermittent sample contact [15]. However, PeakForce Tapping® utilizes oscillation frequencies well below the cantilever resonance and therefore avoids the complicated dynamics associated with AM-AFM. The reduced oscillating frequencies allow for direct force control in PeakForce Tapping®, similar to contact mode measurements, while still avoiding lateral forces. One

can consider PeakForce Tapping® measurements as a collection of continuous force vs. distance (FD) measurements at frequencies between 1 kHz and 10 kHz. In order to avoid resonances at the turnaround points during PeakForce Tapping® measurements, the z-position is modulated by a sine wave instead of a triangular wave, which is used during FD measurements [15]. Figure 22 shows the general operational principle of PeakForce Tapping®. The individual peak tapping force values are used as triggering mechanism to retract the z-piezo, which provides the exceptional force control.

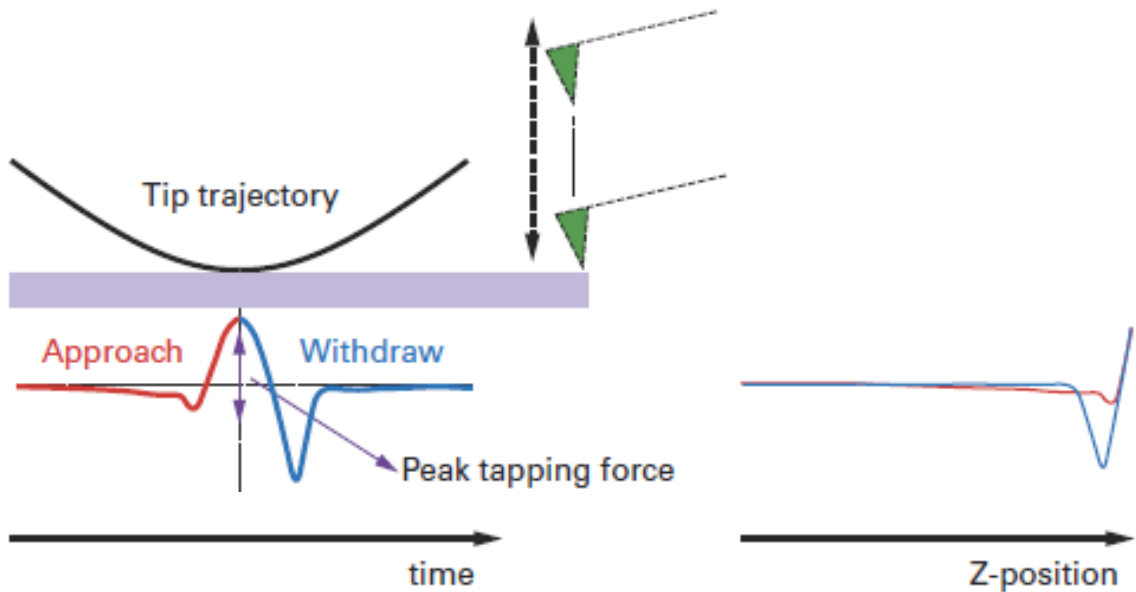


FIGURE 22: General operation principle of PeakForce Tapping® AFM. The cantilever is driven by a sine wave signal and the curves are presented as force vs. time and force vs. z-position [15]. a) Tip trajectory as it approaches the sample. b) Plots of the deflection/force as a function of time and z-position. (Copyright 2011 Bruker Corporation)

In order to perform measurements of the contact resistance during PeakForce Tapping, a bias between tip and sample is applied and Bruker's TUNA™ module (Bruker Corporation, Billerica, MA) is used [16]. The TUNA™ module is a low-noise, high-bandwidth linear current amplifier that allows the resulting tip-sample current to be measured up to 1 kHz tip oscillation frequency. Figure 23 shows force and current vs. time plots resulting from one PeakForce TUNA™ interaction cycle. All current values from PeakForce TUNA™ measurements reported in the thesis represent current values measured at maximum force (Point C in Figure 23).

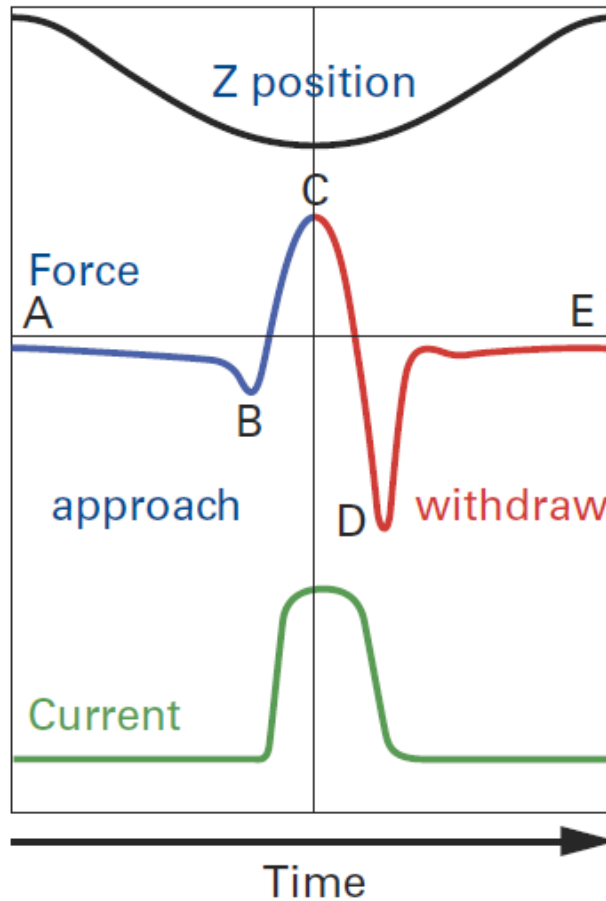


FIGURE 23: Plots of the z position, force and current as a function of time during a PeakForce TUNA™ interaction cycle. Point B corresponds to the snap-in point, point C represents the peak force value and point D corresponds to the adhesion value [16]. (Copyright 2011 Bruker Corporation)

Figure 24 shows a schematic and image of the employed PeakForce TUNA™-based cycling measurements. PeakForce TUNA™ measurements were conducted on a Bruker Dimension ICON AFM (Bruker Corporation, Billerica, MA) under a 0.5 V bias, 1 kHz cycling frequency over a 200 nm x 200 nm area using 36 samples and 6 lines at 2 Hz. This means that each recorded image is composed of 3000 taps. The conductivity

map of each 200 nm x 200 nm image was averaged in the post processing, the average current then transformed into a contact resistance (the 6.71 k Ω series resistor was taken into account) and this value served as a data point of the contact resistance vs. cycling plot. By continuously recording 200 nm x 200 nm images, up to 10⁷ interaction cycles were achieved within 4 hours, with data points every 3000 cycles. Averaging of a 200 nm x 200 nm area was used to mitigate any effect of specific features of the sample such as grain boundaries and localized impurities, and due to the unfeasibility of performing PeakForce TUNA™ measurements in a single point due to drift.

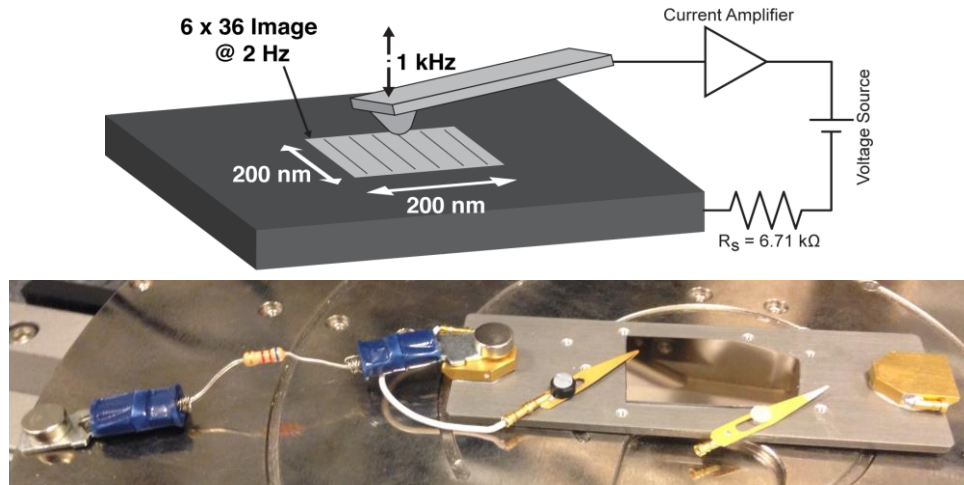


FIGURE 24: Schematic (top) and image (bottom) of PeakForce TUNA™ setup used to interrogate the cycling behavior of single asperity contacts.

To close the electrical circuit and embed the series resistor, it is extremely important to ensure good electrical connections between all parts to avoid additional contact resistances. Strong magnets have been used to ensure a stable, low resistance connection between the series resistor and the sample holder and sample stage, respectively (see Figure 24).

2.3.2 Results for platinum-platinum single asperity contacts

The aforementioned PeakForce TUNA™-based single asperity cycling method was applied to test Pt-coated AFM probes in contact with a Pt-coated single crystal silicon wafer. Both Pt coatings were 70 nm in thickness, the applied bias was 0.5 V, and the contact force was 80 nN. Figure 25 shows the lifetime curve (contact resistance and adhesion force vs. cycling count) of the Pt-Pt contact. The first data point is located at 3000 cycles and every following data point is spaced 3000 cycles apart due to the averaging of a 200 nm x 200 nm image. The contact resistance of the first recorded image (data point at $3 \cdot 10^3$ cycles) is approximately $3 \cdot 10^9 \Omega$ and stays within the same order of magnitude for about $3 \cdot 10^5$ contact cycles. The contact then begins to noticeably degrade above $3 \cdot 10^5$ cycles and a contact resistance of up to $6 \cdot 10^{12} \Omega$ is reached after 10^7 cycles. The adhesion force in contrast displays a steady and almost constant increase from initially 20 nN to 34 nN after 10^7 contact cycles. The steady increase in adhesion indicates that no sudden tip changes occurred through the test.

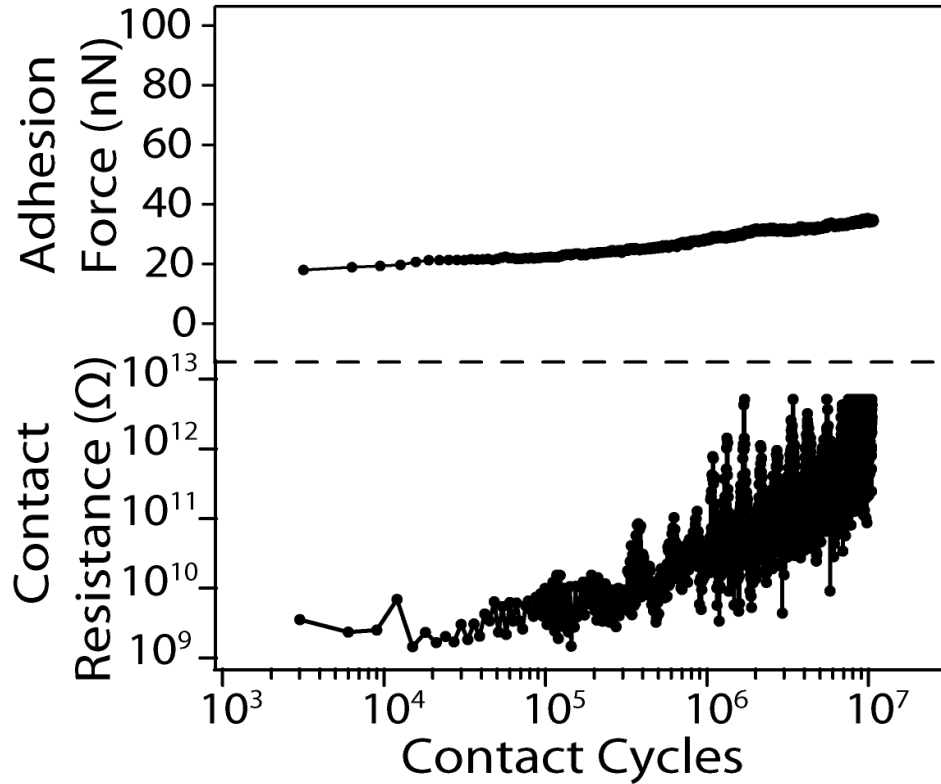


FIGURE 25: Atomic force microscopy lifetime tests of Pt-Pt nanocontacts. Pt-coated AFM probes exhibit more than 3 orders of magnitude increase in contact resistance after cycling to 10^7 contact cycles while adhesion increases only marginally.

The more than three orders of magnitude increase in contact resistance presented in Figure 25 is similar in magnitude to what was observed using the tapping mode amplitude-modulation AFM methodology presented in section 2.2. It can therefore be concluded that the PeakForce TUNA™ methodology captures similar, tribopolymer-based degradation behavior. When compared to Figure 20b, the advantages of the slower cycling frequency used in PeakForce TUNA™ cycling become evident. The data in Figure 25 offers more information about the low cycle count contact resistance values and a higher density of data points.

2.3.3 Effect of probe and sample pre-treatment

Section 2.3.2 confirmed the susceptibility of Pt-Pt contacts to tribopolymer formation and its implications on increasing the contact resistance. We now present attempts to enhance the performance of nanoscale Pt-Pt contacts in cycling tests through two different pre-treatment methods: slide-cleaning and plasma-cleaning of the Pt-coated AFM probe and Pt-coated sample. Figure 26 illustrates the used sample pre-treatment methods. During slide-cleaning, the as-deposited AFM probe was scanned over a $2\ \mu\text{m} \times 2\ \mu\text{m}$ area of the Pt-coated sample under 15 nN normal force. This mechanical sliding procedure was expected to remove any adsorbed surface contaminants on both AFM tip and sample. AFM cycling of the Pt-coated AFM probe inside the slide-cleaned area of the Pt-coated sample, as described in section 2.3.1, was immediately started after the slide-cleaning. During plasma-cleaning, the as-deposited AFM probe and Pt-coated sample were cleaned for 2 minutes inside an oxygen plasma cleaner (Solarus™ Advanced Plasma Cleaning System, Gatan Inc., Pleasanton, CA) under an oxygen plasma (15 W, $p_{\text{O}_2} = 250\ \text{mTorr}$). Upon completion of the plasma cleaning, the Pt-coated AFM probe and sample were immediately loaded into the Bruker Dimension ICON AFM (Bruker Corporation, Billerica, MA) and the cycling experiment was started.

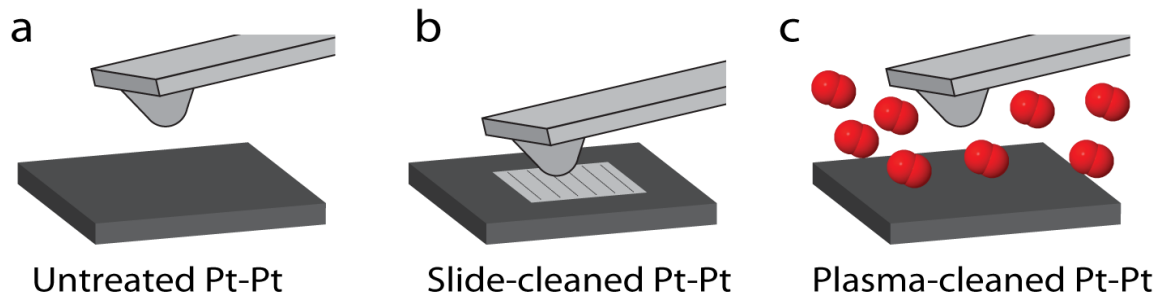


FIGURE 26: Illustrations of sample pre-treatment methods. a) Pt-coated tip and sample tested in the as-deposited state without any pre-treatment. b) Pt-coated tip was scanned in contact mode over the sample to physically remove any contaminants. c) Oxygen plasma cleaning was employed on both, Pt-coated tip and sample, so remove any hydrocarbon contaminants.

Figure 27 shows the results of the AFM cycling lifetime tests conducted on untreated, slide-cleaned, and plasma-cleaned Pt-Pt contacts. While the untreated Pt-Pt contact degrades (increase in contact resistance by three orders of magnitude) as previously seen in section 2.3.2, both the slide-cleaned and plasma-cleaned contacts performed noticeably better. The contact resistance of the slide-cleaned Pt-Pt contact increased by approximately one order of magnitude over 10^7 cycles and the contact resistance of the plasma-cleaned Pt-Pt contact stayed within the same order of magnitude for the duration of the test.

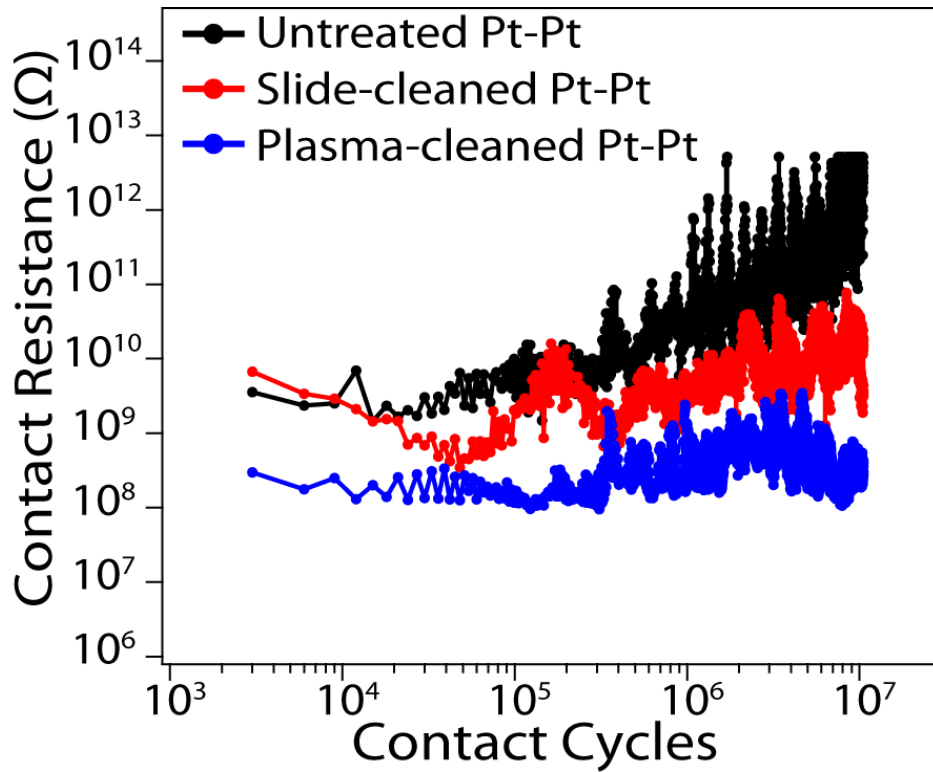


FIGURE 27: Atomic force microscopy lifetime tests of Pt-Pt nanocontacts subject to different pre-treatment methods. Untreated Pt-Pt contact exhibits more than 3 orders of magnitude increase in contact resistance after cycling to 10^7 contact cycles. Slide-cleaned contact exhibits reduced contact resistance increase, whereas plasma-cleaned contacts maintain initial contact resistance over 10^7 contact cycles.

Figure 28 shows the adhesion force as a function of cycle count for the untreated, slide-cleaned, and plasma-cleaned Pt-Pt contacts. The adhesion force steadily and constantly increases for the untreated and slide-cleaned contact throughout the tested 10^7 cycles, which indicates that no sudden changes in contact and/or tip geometry occurred throughout the test. The adhesion force of the plasma-cleaned Pt-Pt contact increased equally until $5 \cdot 10^5$ cycles after which two drops in adhesion force were observed. The first drop of about 5 nN occurred at $8 \cdot 10^5$ cycles and was followed by an

increase in adhesion $2 \cdot 10^5$ later. The second drop was of 20 nN magnitude and occurred at the end of the test, starting at $2 \cdot 10^6$ cycles. The observed adhesion force drops of the plasma-cleaned Pt-Pt contacts are not noticeably correlated with the contact resistance and suggest minor changes of the tip geometry. The changes in adhesion can also be due to chemical changes at the end of the tip (*i.e.*, $-H$ terminated surface vs. $-OH$ terminated surface).

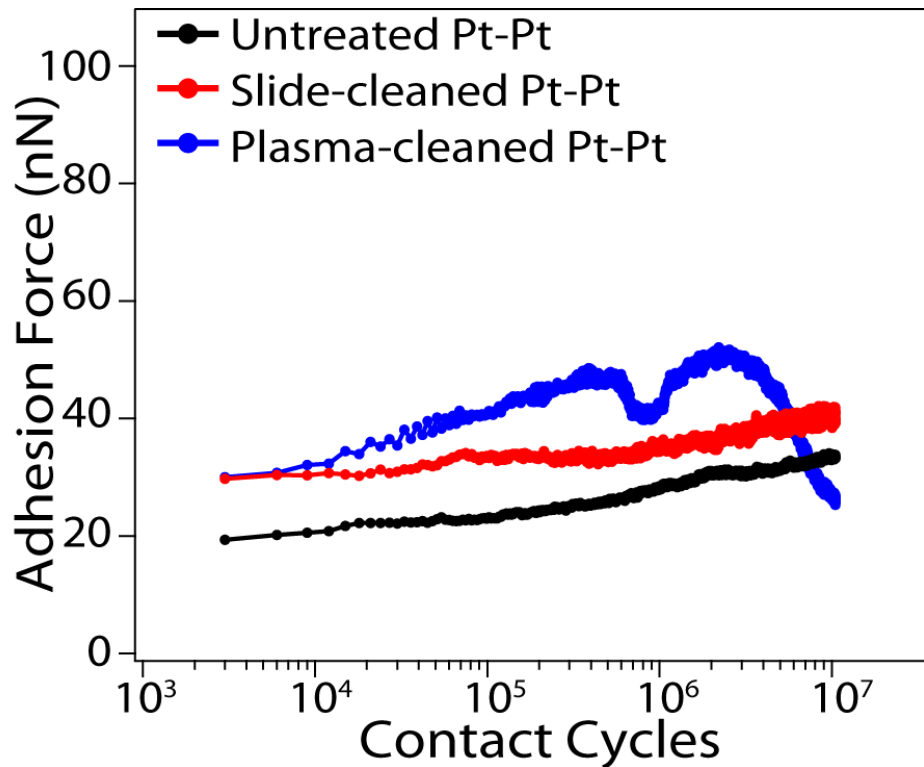


FIGURE 28: Adhesion behavior during atomic force microscopy lifetime tests of Pt-Pt nanocontacts subject to different pre-treatment methods. Adhesion force increases continuously for the untreated and slide-cleaned Pt-Pt samples. Adhesion force initially increases until $5 \cdot 10^5$ cycles for the plasma-cleaned Pt-Pt sample and then becomes unstable.

X-ray photoelectron spectroscopy (XPS) measurements were conducted in order to identify the mechanism by which oxygen plasma cleaning reduces the susceptibility of Pt-Pt contacts to tribopolymer formation. Flat Pt surfaces, identical to those used as counter-samples in the untreated Pt-Pt cycling studies, were analyzed before and after oxygen plasma cleaning in order to identify the composition of the near surface region. Details of the XPS system used here can be found later in this thesis in chapter 3.3.2. Here, we performed angular-resolved measurements of the carbon, platinum, and oxygen signals. Angular-resolved XPS varies the incident angle of the X-ray beam to achieve increased surface sensitivity. The 0° angle corresponds to the lowest surface sensitivity and the 45° angle delivers the highest surface sensitivity. Figure 29 shows the angular-resolved XPS spectra of the C 1s peak of the as-deposited and plasma-cleaned Pt surfaces. The oxygen plasma cleaning reduces the C 1s peak by more than 65% due to its removal of adsorbed adventitious carbon. For the plasma-cleaned sample, the intensity of the C 1s peak decreases with decreasing XPS angle showing that the carbonaceous species are located at the sample surface. These hydrocarbon containing contaminants are present due to the catalytic activity of Pt (see section 3.5 for more details).

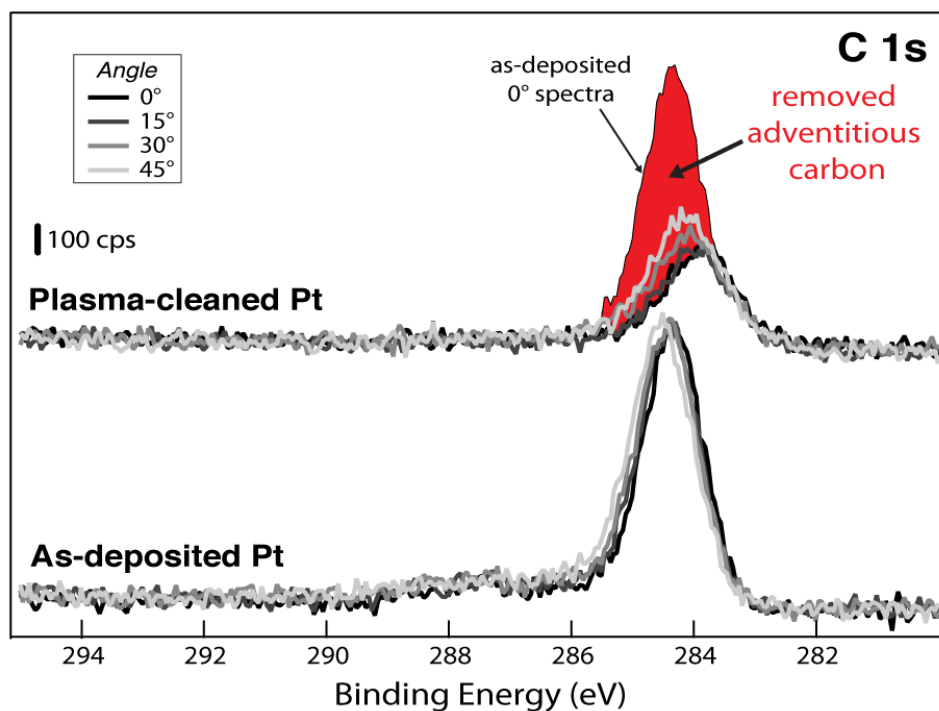


FIGURE 29: Angular-resolved high resolution XPS spectra of the C 1s peak. Oxygen plasma cleaning reduces the C 1s peak noticeable due to its removal of adventitious carbon. The red area in the plasma-cleaned Pt C 1s spectrum represents the as-deposited Pt C 1s spectra at 0° for reference.

Figure 30 presents the angular-resolved XPS spectra of the Pt 4f peaks of the as-deposited and plasma-cleaned Pt surfaces. Small amounts of platinum oxide are formed as a consequence of the oxygen plasma treatment, while most of the metallic platinum is maintained.

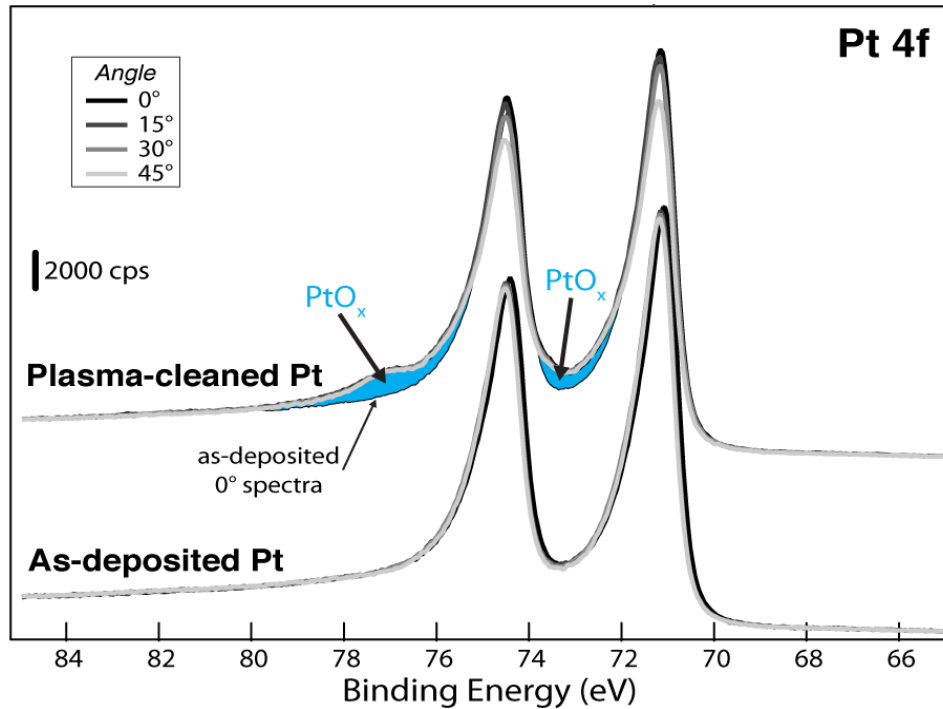


FIGURE 30: Angular-resolved high resolution XPS spectra of the Pt 4f peaks. Oxygen plasma cleaning forms small amounts of platinum oxygen, while still maintaining most of the metallic platinum.

In summary, the oxygen plasma cleaning has two effects on as-deposited Pt surfaces: first, it removes large amounts of adsorbed adventitious carbon leading to less tribopolymer formation and thereby less contact resistance increase during cycling; second, it maintains most of the metallic platinum by only forming small amounts of high resistive platinum oxide ensuring low starting contact resistances.

2.4 Summary

In this section we present a novel, high-throughput electrical contact screening method based on PeakForce Tapping® (Bruker Corporation, Billerica, MA) atomic force

microscopy (AFM) that enables the simultaneous evaluation of electrical contact resistance and adhesion during millions of contact cycles to be tested in laboratory timeframes. We developed AFM probe holders that enable sputter coating of AFM tips with various materials as well as the thermal annealing of AFM probes to facilitate solid-state diffusion reactions. We cycled self-mated Pt contacts under forces and environments representative of NEM switch operation for ten million times, while recording the electrical contact resistance and adhesion. The contact resistance increased more than three decades due to cycling-induced growth of insulating tribopolymer. We then employed different Pt-Pt contact pre-treatment methods, including slide-cleaning and plasma-cleaning, and found that slide-cleaning can reduce the amount of electrical degradation. Plasma-cleaning however, was seen to completely inhibit the electrical degradation of Pt-Pt contacts cycled for ten million cycles due in part to the removal of absorbed adventitious carbon prior to cycling. This suggests a route for mitigating contamination-induced failure.

BIBLIOGRAPHY CHAPTER 2

- [1] Chen, L.; Guo, Z. J.; Noshi, N.; Eid, H.; Adams, G. G.; McGruer, N. E. *J. Micromech. Microeng.* **2012**, *22*, 045017.
- [2] Dickrell, D. J.; Drugger, M. T. *IEEE Trans. Compon. Packag. Technol.* **2007**, *30*, 75-80.
- [3] Czaplewski, D. A.; Nordquist, C. D.; Dyck, C. W.; Patrizi, G. A.; Kraus, G. M.; Cowan, W. D. *J. Micromech. Microeng.* **2012**, *22*, 105005.
- [4] Coutu, R. A.; Reid, J. R.; Cortez, R.; Strawser, R. E.; Kladitis, P. E. *IEEE Trans. Compon. Packag. Technol.* **2006**, *29*, 341-349.
- [5] Sader, J. E.; Larson, I.; Mulvaney, P.; White, L. R. *Rev. Sci. Instrum.* **1995**, *66*, 3789-3798.
- [6] Kwon, H.; Choi, D.-J.; Park, J.-H.; Lee, H.-C.; Park, Y.-H.; Kim, Y.-D.; Nam, H.-J.; Joo, Y.-C.; Bu, J.-U. In Proceedings of the 20th IEEE International Conference on Micro Electro Mechanical Systems (MEMS 2007), Piscataway, NJ, **2007**, 231-234.
- [7] Garcia, R.; Perez, R. *Surf. Sci. Rep.* **2002**, *47*, 197-301.
- [8] Garcia, R.; San Paulo, A. *Phys. Rev. B: Condens. Matter Mater. Phys.* **1999**, *60*, 4961-4967.
- [9] Law, B.; Rieutord, F. *Phys. Rev. B: Condens. Matter Mater. Phys.* **2002**, *66*, 035402.
- [10] Derjaguin, B. V.; Müller, V. M.; Toporoy, Y. P. *J. Colloid Interface Sci.* **1975**, *53*, 314-326.
- [11] Wabiszewski, G. E. Interrogation of Single Asperity Electrical Contacts Using Atomic Force Microscopy with Applications to NEMS Logic Switches. *PhD Thesis*, **2013**.
- [12] Chen, L.; Lee, H.; Guo, Z. J.; McGruer, N. E.; Gilbert, K. W.; Mall, S.; Leedy, K. D.; Adams, G. G. *J. Appl. Phys.* **2007**, *102*, 0749101.
- [13] Hermance, H. W.; Egan, T. F. *Bell Syst. Tech. J.* **1958**, *37*, 739-776.
- [14] Beyer, M. K.; Clausen-Schaumann, H. *Chem. Rev.* **2005**, *105*, 2921-2948.
- [15] Kaemmer, S. B. *Bruker Application Note # 133*. **2011**.
- [16] Li, C.; Minne, S.; Pittenger, B.; Mednick, A. *Bruker Application Note # 132*. **2011**.

CHAPTER 3: DEVELOPMENT OF NEXT-GENERATION NANOELECTROMECHANICAL SWITCH CONTACT MATERIALS²

This chapter describes general selection criteria for nanoelectromechanical (NEM) switch contact materials and briefly discusses several candidate materials. Then platinum silicide (Pt_xSi) as a NEM switch contact material is discussed. First, Pt_xSi formation from thin amorphous silicon (*a*-Si) films is discussed. Second, source-limited and kinetically-limited solid-state diffusion as methods to precisely tune Pt_xSi stoichiometry and properties is introduced. Third, the electronic structure and electrical properties of Pt_xSi are discussed in detail. And last, preliminary results of atomic force microscopy (AFM) cycling tests using Pt_xSi as contact material are presented.

3.1 Selecting nanoelectromechanical switch candidate contact materials

As discussed in chapters 1.2 and 1.3, the availability of suitable contact materials represents the greatest obstacle to NEM switch commercialization to date. Figure 31 summarizes the desired properties of a NEM switch contact material. Mechanical robustness is desired for protection against surface degradation during switching. Electrically conductive materials are desired to achieve low contact resistances in the switch. Low adhesion materials are needed in order to avoid stiction/adhesive failures (i.e. NEM switch stays stuck shut). And finally, chemical inert contact materials are desired in order to avoid the formation of insulating films/contaminants before or

² Parts of this chapter appear in print: Adapted with permission from Streller, F. *et al.*, *Adv. Mater. Interfaces* **2014**, *1*, 1300120. (Copyright 2014 John Wiley and Sons), Streller, F. *et al.*, *Chem. Mater.* **2015**, *27*, 4147–4253 (Copyright 2015 American Chemical Society), and Streller, F. *et al.*, *J. Phys. Chem. Lett.* **2016**, *6*, 2573–2578 (Copyright 2016 American Chemical Society).

throughout the cycling. Another important point to consider is that the selected contact materials need to be compatible with common semiconductor fabrication techniques in order to guarantee a successful commercialization. This means that the deposition/formation temperatures involved in the contact material fabrication should not exceed 400-500 °C and that standard deposition (*i.e.* sputtering) and annealing techniques (*i.e.* rapid thermal annealing) should be used.

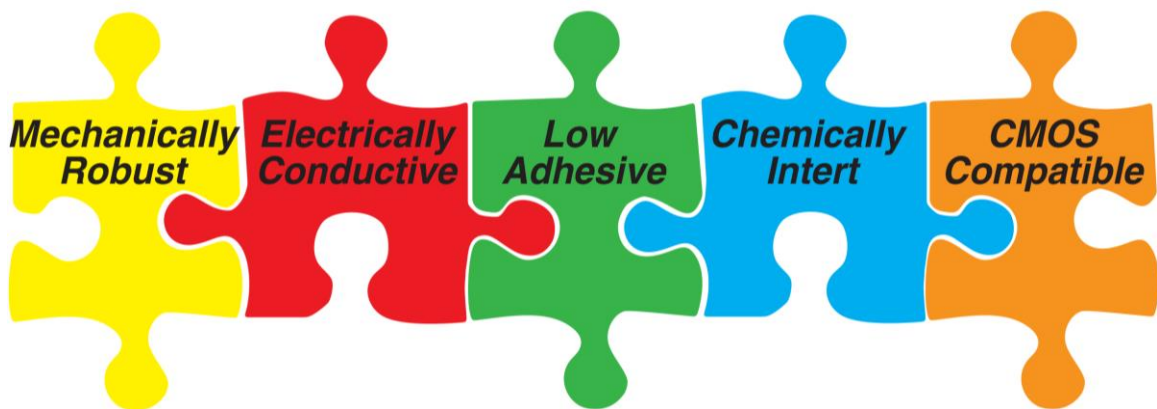


FIGURE 31: Desired properties of NEM switch contact materials.

Finding materials that feature the desired properties mentioned in Figure 31 is extremely difficult and requires a thorough materials selection process. Figure 32 illustrates such a contact material selection process for pure elements. The initial 111 available elements can be quickly reduced to only 7 through the application several material property-based criteria. The exclusion of unstable, gaseous and insulating ($\sigma_{\text{electr}} < 1 \cdot 10^4 \text{ S/m}$) materials reduces the number of elemental options from 111 to 52. If further all toxic materials and alkali-metals are excluded, this number reduces to 36. A following exclusion of low melting point materials ($T_{\text{melt}} \leq 500^\circ\text{C}$) and materials of

insufficient mechanical stiffness ($E < 75$ GPa) reduces the number of possibilities to 22. Finally, the exclusion of materials that form insulating layers such as oxides and sulfides reduces the number of contact material candidates to 8. While this selection only focusses on pure elements and excludes alloys and composites, it shows how simple property-based criteria can quickly reduce the number of useful NEM contact material candidates.

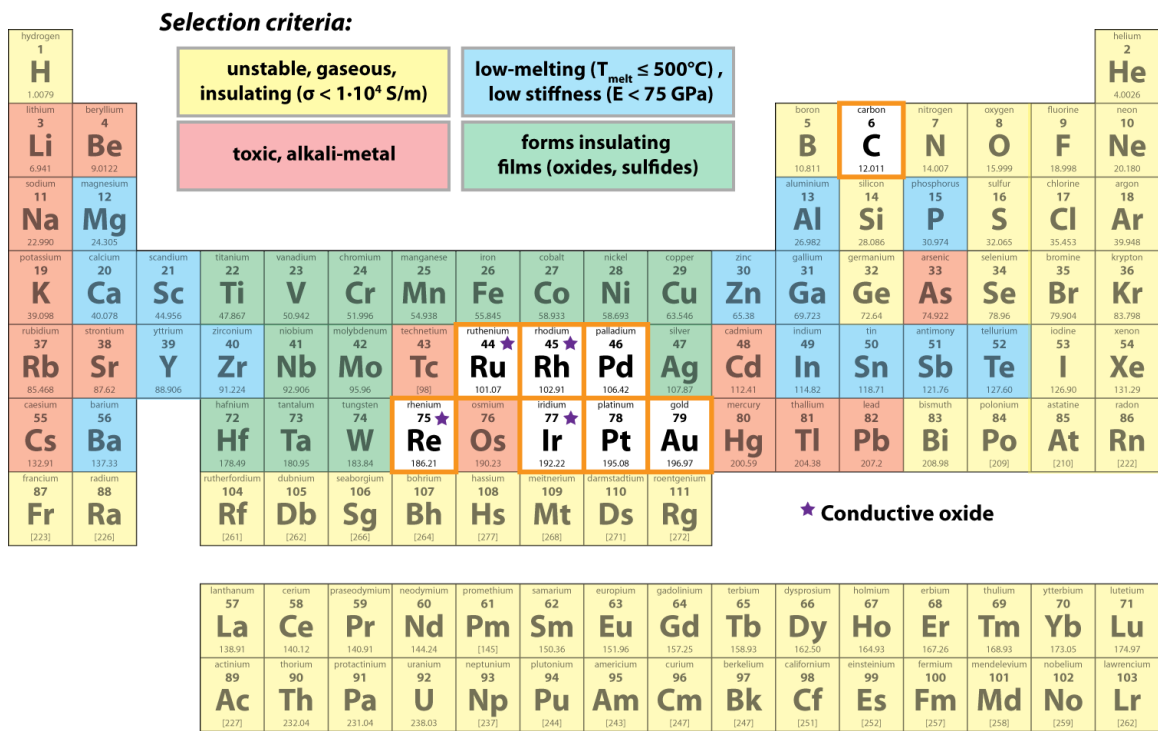


FIGURE 32: Example of the NEM contact materials selection process for pure elements. After applying materials property criteria, only 8 out of initially 111 elements remain realistic candidates as contact material for NEM switches.

The 8 elements that remain as possible NEM switch contact material are Au, Pt, Pd, Re, Ru, Rh, Ir and C (note: the C allotrope graphene fulfills all the criteria and will be discussed separately in Chapter 5). The refractory metals Re, Ru, Rh, and Ir are mechanically robust and form a conductive oxide layer, which provides the necessary electrical conductivity by additionally reducing the work of adhesion. However, integration of Re, Ru, Rh and Ir into CMOS processes is not straightforward, mainly because of underdeveloped methods to etch these materials [1]. The noble metal Au possesses a high electrical conductivity and low surface contamination, but its high adhesion combined with low mechanical robustness impedes its application as NEM contact material. Mechanical deformation during cycling can lead to a growth in contact area and thereby to increased adhesive interactions between the top and bottom contact, similar than shown previously in Figure 10. The metals Pt and Pd have similar oxidation resistance and electrical conductivity, while Pt being mechanically more robust than Pd. However, Pt leads to the formation of tribopolymers due to its catalytic activity as shown in sections 2.2 and 2.3. This exercise of finding candidate contact materials within pure elements shows that next-generation NEM switch contact materials will likely be multi-component materials and not single-elements. This is in contrast to micro-scale switches (RF MEMS switches), where both Au-based and Pt-based contact materials can be used due to the higher contact and separation forces achievable in MEMS devices that are able to separate adhesive contacts or penetrate through thin insulating films.

Table 1 reviews and compares several candidate contact materials according to the metrics introduced in Figure 31 as well as their CMOS compatibility. The materials in this list were preselected according to availability, prior use, and existence of data.

TABLE 1: Qualitative evaluation of contact material candidates.

Candidate Material	Mechanical Robustness	Electrical Conductivity	Low Adhesion	Chemical Inertness	CMOS Compatibility
Silicides					
Ni _x Si	😊	😊	😊	😞 #	😊
Ti _x Si	😊	😊	😊	😞 #	😞 *
Pt _x Si	😊	😊	😊	😊	😊
Co _x Si	😊	😊	😊	😞 #	😞 *
Mo _x Si	😊	😊	😊	😞 #	😞 *
Diborides					
HfB ₂	😊	😐	😊	😞 #	😊
TiB ₂	😊	😊	😊	😞 #	😊
ZrB ₂	😊	😊	😊	😞 #	😊
Carbides/Nitrides					
WC	😊	😊	😊	😞 #	😊
TiN	😊	😐	😊	😞 #	😊
Conductive Oxides					
RuO _x	😊	😊	😊	😊	😞 ^
ReO _x	😊	😊	😊	😊	😞 ^
Carbon-based Materials					
N-UNCD	😊	😞	😊	😞	😞 *
Graphene	😊	😊	😊	😊	😞 *

= oxide formation, * = high formation temperature, ^ = etch recipe needed

Table 1 shows that several material groups possess properties that are desired for NEM switch contact materials. Most metal silicides possess high mechanical robustness coupled with sufficient electrical conductivity and low adhesion. However, oxide formation and high silicidation temperatures are a concern for Ni-, Ti-, Co-, and Mo-based silicides. Diborides are an interesting class of materials for NEM switches, as their only flaw is their susceptibility to oxide formation over time. Carbides and nitrides suffer from oxide formation as well, while possessing several other promising properties. Conductive oxides are extremely appealing as NEM switch contact material due to their inherent electrical conductivity, low adhesion, and mechanical robustness. A possible issue with conductive oxides is the lack of etching methods that would be necessary for successful semiconductor integration. Carbon-based materials such as conductive nanocrystalline diamond (N-UNCD) and graphene possess intriguing properties but also suffer from potential process integration issues. Table 1 highlights that platinum silicide (Pt_xSi) is the most appealing candidate material since it theoretically possesses all the desired mechanical, electrical, and adhesive properties combined with resistance against contamination formation and semiconductor compatible formation temperature and processes. The remainder of this chapter studies the formation process of Pt_xSi thin films, their electrical and mechanical properties, and the performance of Pt_xSi in AFM-based contact reliability tests.

3.2 Platinum silicide as nanoelectromechanical switch contact material

3.2.1 Previous work on platinum silicide and its advantages

Platinum silicide (Pt_xSi) possesses several appealing characteristics that make it an attractive switch contact material candidate. Pt_xSi was first investigated in the 1980's as an electrical contact material with high conductivity in fully-electronic, Si-based devices [2]. More recently, Pt_xSi films have demonstrated wear and oxidation resistance during nanoscale mechanical contact [3]. Conversion of Pt and single-crystal silicon (*sc*-Si) to Pt_xSi results in approximately 15% volumetric shrinkage [2] and may be exploited to separate buried material interfaces. Pt_xSi could therefore be used to release NEM switches with a self-formed gap caused by interfacial separation driven by shrinkage-induced tensile stress. Nguyen *et al.* recently demonstrated the release of free-standing MEMS structures with Ti/Si and Mo/Si chemistries [4], a task traditionally accomplished using costly and time-consuming sacrificial Si release etches. Silicide-based release of buried interfaces would also eliminate exposure to air, preventing adsorption of carbon, oxygen, and other contaminants which profoundly affect device operation.

Pt_xSi formed from thin film Pt and a *sc*-Si wafer is described by a two-reaction process (Figure 33) [5,6]. Since common NEM switch geometries [7,8] demand silicidation away from the *sc*-Si carrier wafer, the *sc*-Si/Pt silicidation process is incompatible with NEM switch geometries, especially if co-integration with CMOS is desired. Furthermore, silicide-release using existing device topologies would require silicidation on both the top and bottom of features, which is not compatible with *sc*-Si/Pt process. Instead, Pt_xSi must be formed from precursors both deposited as thin films, necessitating the use of either polycrystalline Si or amorphous silicon (*a*-Si) precursor films; *a*-Si's homogeneity renders it preferable.



FIGURE 33: Schematic of typical Pt_xSi formation using a thin layer of Pt deposited onto a cleaned sc-Si wafer, and subsequently annealed. In the first reaction, the Pt diffuses into the sc-Si and the intermediate Pt-rich silicide Pt_2Si is formed. After all Pt is consumed, the sc-Si diffuses into Pt_2Si to form the thermodynamically stable PtSi phase. The temperature range of the Pt_2Si formation (180-200 °C) and the PtSi formation (280-400 °C) are within the thermal budget of most CMOS processes.

3.2.2 Formation of platinum silicide thin films from amorphous silicon and platinum

Little is known about the Pt_xSi formation using an *a*-Si precursor. Ito *et al.* investigated Pt_xSi formation with hydrogenated *a*-Si (*a*-Si:H) and found the simultaneous existence of PtSi, Pt_2Si , and incompletely consumed initial Pt [9]. Impurities at the silicidation boundary, mainly hydrogen from the *a*-Si:H film, were hypothesized to limit Pt consumption. Here, thin layers of *a*-Si and Pt are employed instead. We hypothesize that the relative thicknesses of *a*-Si and Pt films control the stoichiometry and resulting mechanical and electrical properties of the silicide product. This methodology differs significantly from the formation of Pt_xSi from a thin Pt layer on a sc-Si wafer, which constitutes an unlimited supply of Si.

Samples with two Pt:*a*-Si film thickness ratios – 1:1 and 1:2 – were fabricated to explore the effect of precursor material thickness on silicide stoichiometry (Figure 34d and Figure 34e) and the resulting mechanical and electrical properties. To achieve this, a sc-Si carrier wafer was first sputter-coated with aluminium nitride (AlN, thickness: 3

μm) to act as a diffusion barrier between the silicide and carrier wafer. The deposition of AlN also allowed the mimicking of the topology of existing piezoelectrically-actuated NEM switch prototypes [8]. Thin layers of *a*-Si and Pt of 100-200 nm-thickness were subsequently sputter-coated on top of the AlN layer. The *a*-Si and Pt depositions were conducted sequentially in the same deposition system with vacuum maintained, thus minimizing adsorbed contamination between the layers and oxidation of the *a*-Si, both of which would inhibit silicidation. The samples were then removed from the deposition system and subsequently annealed for 6 hours at 500 °C inside an X-ray photoelectron spectrometer (XPS) in high vacuum ($<1 \cdot 10^{-8}$ Torr) [10], while continuously monitoring the Pt 4f and Si 2p XP signals. High-resolution angle-resolved XPS analysis of the near-surface region before and at the end of the annealing process allowed the stoichiometry of the as-deposited Pt and formed Pt_xSi , as well as its in-depth homogeneity, to be determined. Nanoindentation of the as-deposited and annealed samples was used to determine film modulus and hardness. Conductive atomic force microscopy (cAFM) was performed to evaluate contact resistance and surface morphology of the as-deposited Pt and formed Pt_xSi films. All experiments were repeated twice to ensure reproducibility.

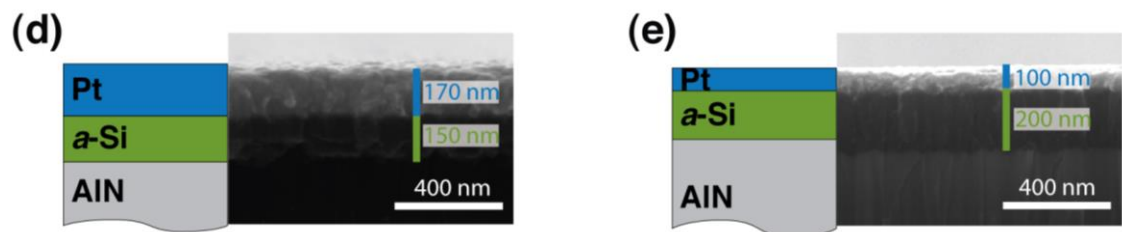


FIGURE 34: *a*-Si/Pt samples. d, Schematic and SEM cross-section image of the as-deposited Pt:*a*-Si = 1:1 sample. e, Schematic and SEM cross-section image of the as-deposited Pt:*a*-Si = 1:2 sample.

The high-resolution XPS (HR-XPS) Pt 4f spectrum of as-deposited Pt (from the Pt:*a*-Si = 1:1 sample; note: identical spectra were obtained with the Pt:*a*-Si = 1:2 sample) is displayed in Figure 35c. The Pt 4f peak consists of two components, Pt 4f_{7/2} and Pt 4f_{5/2}, due to spin-orbit coupling. Both peak position (70.90 eV) and lineshape of the Pt 4f_{7/2} are characteristic of metallic platinum (Figure 3c). Upon annealing, the Pt 4f_{7/2} spectra of both Pt:*a*-Si ratios (i.e., Pt:*a*-Si = 1:1 in Figure 35b and Pt:*a*-Si = 1:2 in Figure 35a) exhibited a multicomponent character: besides metallic platinum (70.90 eV), three new components appeared at 71.47, 72.14, and 72.50 eV, assigned to Pt₃Si, Pt₂Si, and PtSi, respectively. The relative concentrations of Pt, Pt₃Si, Pt₂Si, and PtSi are reported in the insets in Figure 35. The Pt:*a*-Si = 1:1 sample produced a dominant Pt₃Si/Pt₂Si phase mixture (74%), while the Pt:*a*-Si = 1:2 sample produced mostly PtSi (71%) with little Pt₂Si (23%) remaining. This demonstrates that the near-surface stoichiometry of Pt_xSi can be tuned by varying the thickness ratio of Pt and *a*-Si, and that Pt_xSi formation occurs at CMOS compatible temperatures (400-425 °C).

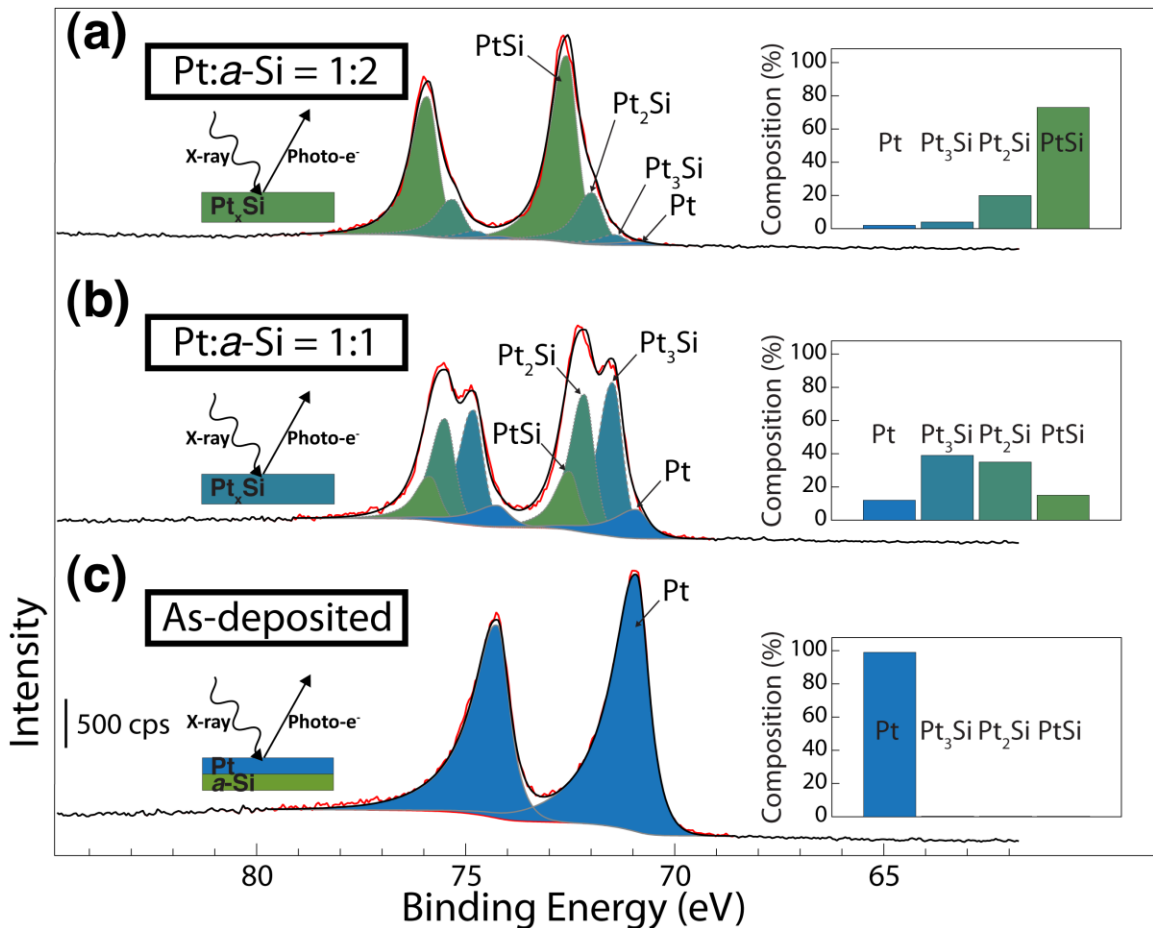


FIGURE 35: Surface Characterization of as-deposited Pt and formed Pt_xSi. a, High-resolution XPS spectra of the Pt 4f peaks of the annealed Pt:a-Si = 1:2 spectra. The Pt 4f peaks shift to higher binding energies indicating Pt_xSi formation with progressively increase Si content. The near-surface composition of the annealed Pt:a-Si = 1:2 sample is dominated by Si-rich PtSi. b, High-resolution XPS spectra of the Pt 4f peaks of the annealed Pt:a-Si = 1:1 spectra. The Pt 4f peaks shift to higher binding energies indicating Pt_xSi formation. Near-surface composition of the annealed Pt:a-Si = 1:1 sample dominated by Pt-rich P_xSi. c, High-resolution XPS spectra of the Pt 4f peaks of the as-deposited sample. The Pt 4f peaks indicate the presence of pure metallic Pt.

We analyzed the silicide samples using the continuous stiffness measurement (CSM) nanoindentation method [11] and depth-controlled nanoindentation to reveal the

changes in hardness and modulus due to silicidation of the two samples. It should be noted that, to characterize the mechanical properties of a thin film, two possible artifacts must be mitigated: (1) a surface roughness effect (at small indentation depths comparable to the surface roughness), inducing an underestimation of the hardness and modulus due to the incompact surface; and (2) a substrate effect (at large indentation depths beyond 20% of the film thickness), inducing an overestimation of the hardness and modulus due to the stiffer, harder AlN substrate. The CSM method, which enables the measurement of the modulus and hardness as a function of indentation depth, was used to determine the appropriate range of indentation depths to minimize the two aforementioned effects. Figure 36a shows the CSM modulus and hardness curves for the Pt:*a*-Si = 1:1 sample in the as-deposited condition and after annealing. Both the modulus and hardness curves show a shoulder at approximately 50 nm indentation depth, indicating that this depth corresponds to minimized surface roughness and substrate effects. Similar tests on the Pt:*a*-Si = 1:2 sample also found the optimal sampling depth to be 50 nm. Therefore, measurements at this depth are used to extract the mechanical properties of the films. Figure 36b summarizes the modulus and hardness values obtained after performing approximately 100 50-nm indents on the two samples in the as-deposited and annealed states. For both samples, the modulus and hardness increases by approximately 50% due to annealing. Thus, both silicide films are mechanically more robust and will therefore be significantly more resistant to mechanical degradation than the as-deposited Pt films from which they originated. These results represent the first reported values for modulus and hardness measurements on Pt_xSi.

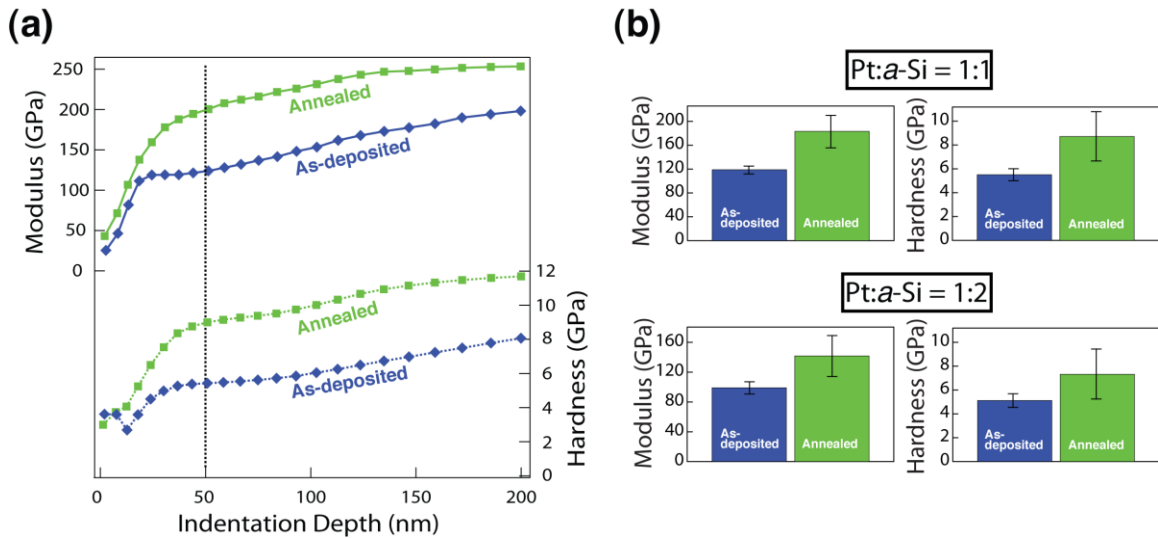


FIGURE 36: Nanoindentation of as-deposited Pt and formed Pt_xSi . a, Modulus and hardness as a function of indentation depth curves for the Pt:*a*-Si = 1:1 sample in the as-deposited and annealed state. Both modulus and hardness shoulder at approximately 50 nm indentation depth, indicating that this depth is ideal for measuring the thin film properties. b, Average modulus and hardness values and their standard derivations obtained from 100 depth-controlled indentations at 50 nm indentation depth for the Pt:*a*-Si = 1:1 and Pt:*a*-Si = 1:2 samples in their as-deposited and annealed states. For both Pt:*a*-Si ratios, the modulus and hardness significantly increased due to the Pt_xSi formation compared to the as-deposited film.

We further analyzed the silicide samples using conductive atomic force microscopy (cAFM) measurements to determine the contact resistance of the silicide films of different stoichiometries compared to as-deposited Pt. Figure 37a-c show contact resistance color relief maps of representative areas of as-deposited Pt, the annealed Pt:*a*-Si = 1:1 sample, and the annealed Pt:*a*-Si = 1:2 sample, respectively. Insets show the distribution of contact resistance values over the probed area; variations are due to grain boundaries, roughness, and contamination. The distribution shifts to higher values with increasing *a*-Si film thickness and thereby with increasing Si-content

in the silicide film (see Figure 2). The minimum contact resistance values encountered during the scan are 4.65 k Ω for as-deposited Pt, 5.14 k Ω for the Pt:*a*-Si = 1:1 sample and 9.37 k Ω for the Pt:*a*-Si = 1:2 sample (Figure 37d). The minimum contact resistance of both silicide stoichiometries is less than twice the value measured for as-deposited Pt. This shows that the silicide films possess a metallic-like contact resistance. The minimum contact resistance increase of the Pt-rich silicide film (Pt:*a*-Si = 1:1) compared to as-deposited Pt film is modest (<10%), and well within ranges needed for NEM switch applications. The coupling between contact resistance and *a*-Si content in the silicide film demonstrates that we can control the electronic properties of the silicide by changing the Pt:*a*-Si layer ratio and thereby the silicide stoichiometry.

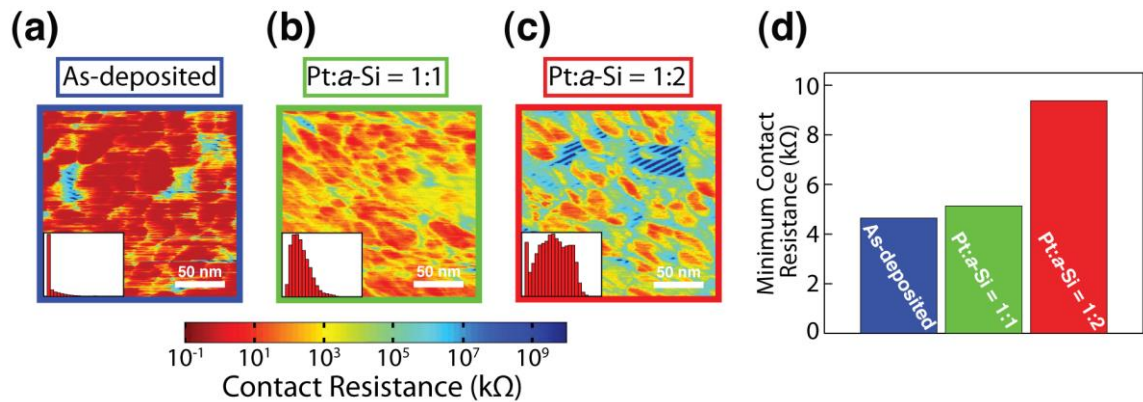


FIGURE 37: Conducting-mode contact atomic force microscopy measurements of as-deposited Pt and Pt_xSi samples. a-c, Contact resistance color relief maps of a representative 200 nm x 200 nm scan on a representative a) as-deposited Pt film, b) annealed Pt:a-Si = 1:1, and c) annealed Pt:a-Si = 1:2. Insets show the contact resistance distribution obtained from each scan. The contact resistance distribution shifts towards higher contact resistances with increasing a-Si availability from a-c. d, Minimum contact resistance values encountered during the 200 nm x 200 nm scans. Annealed Pt:a-Si = 1:1 film possesses contact resistance values approximately 10 % higher than those seen in pure Pt films. The higher a-Si content in the Pt:a-Si = 1:2 film leads to a further increased contact resistance to approximately twice the value of as-deposited Pt. However, these values are still within the same order of magnitude of pure Pt and well within acceptable bounds for NEM switches.

Figure 37a indicates a correlation of the surface topography, *i.e.* grain boundaries, and the measured contact resistance. Line scans of the contact resistance and sample topography images presented in Figure 38 were conducted to further explore this correlation.

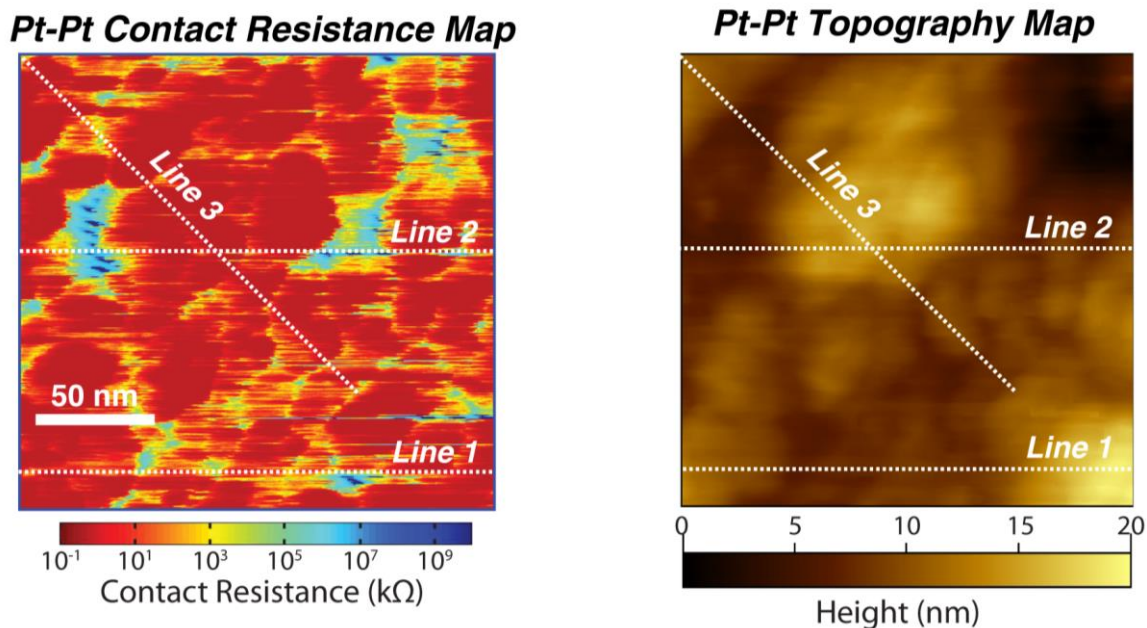


FIGURE 38: AFM contact resistance and topography images of a Pt-coated sample measured with a Pt-coated probe. The locations of three line scans are indicated on both images.

Figure 39 compares the height and contact resistance for three line scans. Regions of high contact resistance correspond to regions of valleys in the sample and low contact resistances were measured at peaks. The contact resistance and topography images in Figure 38 indicate that the Pt grain boundaries are located wherever a valley in the topography image is and that peaks in contact in topography correspond to the middle of each Pt grain. The multiple orders of magnitude higher contact resistance values at grain boundaries, seen in all three line scans, may be due to either a geometric effect or an inherent grain boundary effect. The Pt-coated AFM probe could be too big to sufficiently contact the topographically lower grain boundary region during the measurement and therefore record a large contact resistance. A second

explanation of the high contact resistance could be that the grain boundary is prone to increased contamination buildup or increased electron scattering due to impurities.

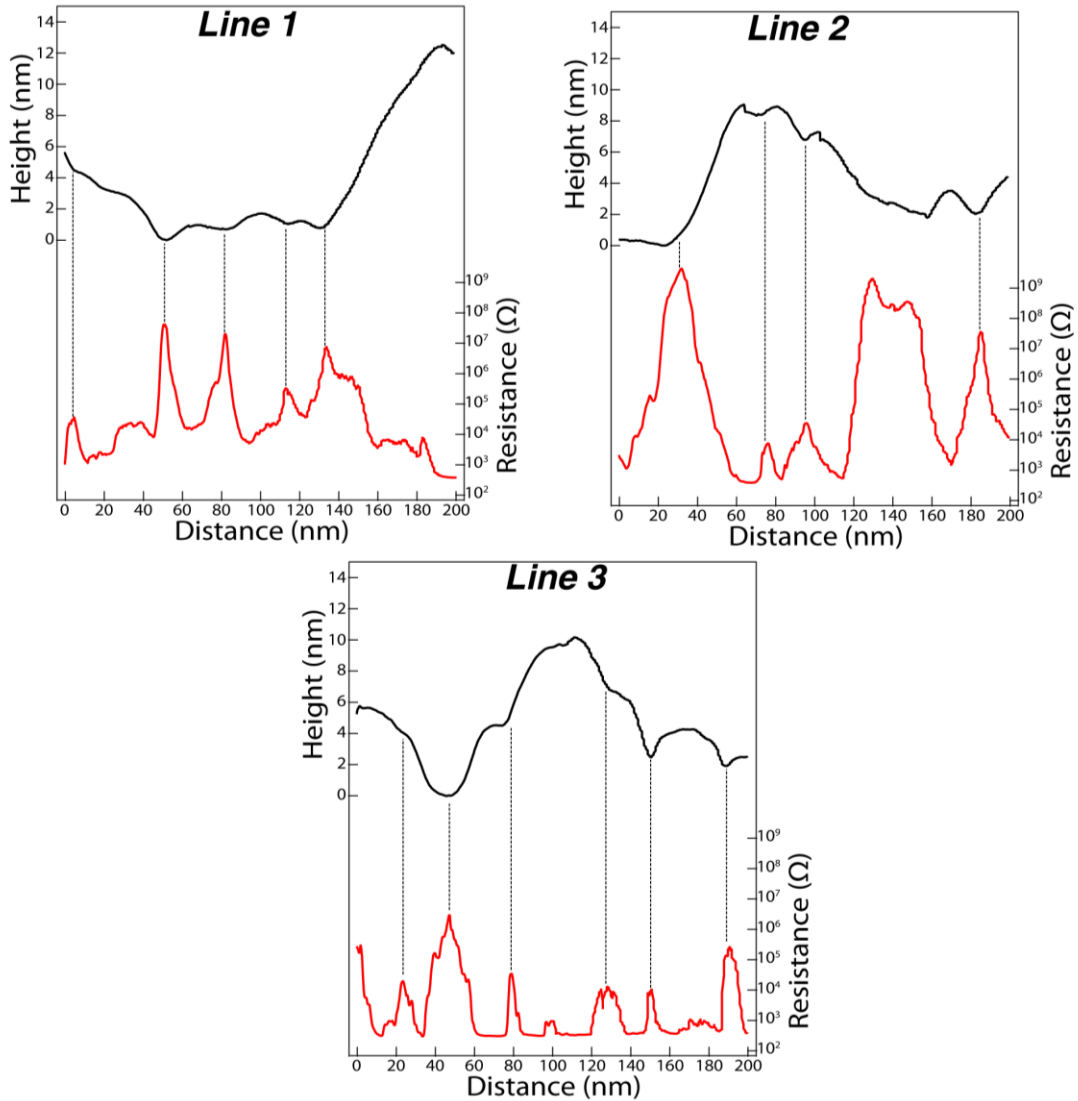


FIGURE 39: Height and contact resistance line scans of a Pt-coated sample. Peaks of the sample are correlated to low contact resistances and valleys of the sample are correlated to high contact resistances.

Figure 40 shows a replot of the data from Line 1 of Figure 39 with matched scale bars for scan distance and height. Additionally, a transmission electron microscopy image of a Pt-coated AFM, with identical scale bar than scan distance and height, is overlaid. The Pt-coated AFM probe shown in Figure 40 and the probe used to take the data shown in Figure 38 come from the same batch of sc-Si AFM probes (PPP-FM Probes, NANOSENSORS™, Neuchatel, Switzerland) and were both coated with 70 nm Pt.

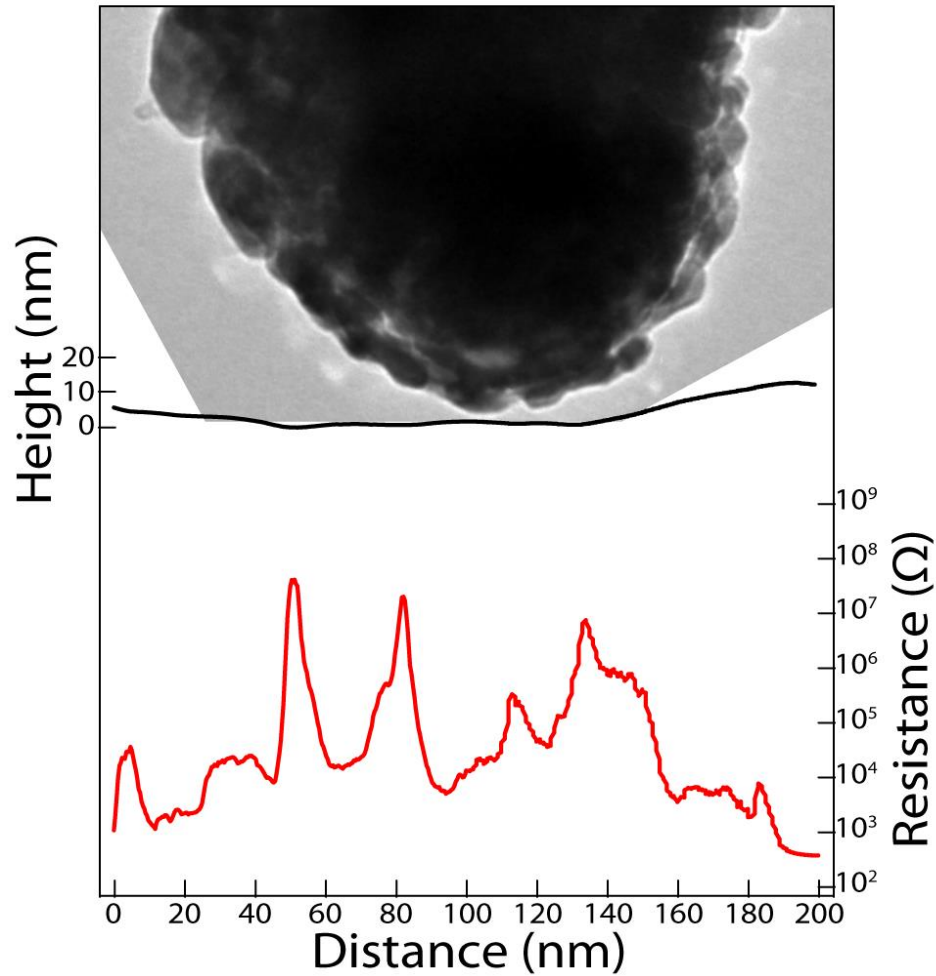


FIGURE 40: Height and contact resistance data of Line 1 plotted with equal scale bars for scan distance and height. Transmission electron microscopy image of a Pt-coated AFM probe is shown with identical scale bar than the scan distance and height.

A comparison of the size of the AFM probe to the profile of the Pt surface shows that the probe is able to make sufficient contact to the sample surface throughout the whole scan. This indicates that the geometric effect of the AFM probe size can be neglected and that the high contact resistance at grain boundaries is either due to

increased contaminant adsorption on those areas or inherently higher resistances of the grain boundaries due to impurities.

3.2.3 Platinum silicide-based release of microswitches

We demonstrate nanoscale gap formation using a silicide-based release process with Pt_xSi formed from *a*-Si and Pt for the first time in Figure 41. The Pt layer diffused into the *a*-Si layers above and below upon rapid thermal annealing (5 minutes, 600 °C, in nitrogen), to form two Pt_xSi layers cleanly separated by a 10-15 nm gap, a geometry that is rather involved to form using sacrificial etch processes. This vacuum gap is protected from air exposure which can be desirable for NEM applications where avoiding contamination is critical.

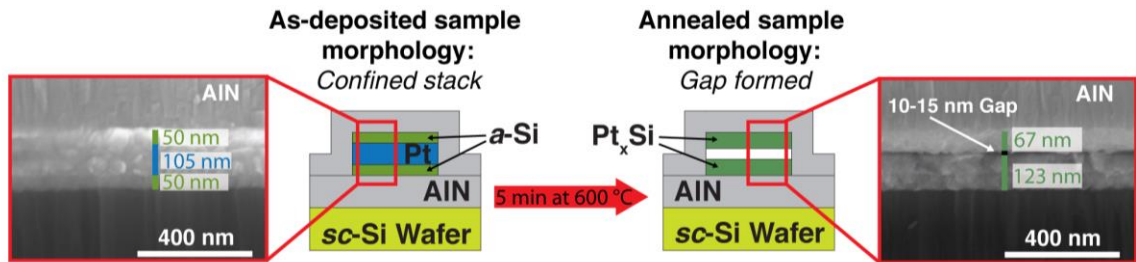


FIGURE 41: Schematic and SEM cross-section of the Pt_xSi -based silicide-release process. A Pt layer, which is initially sandwiched between two *a*-Si layers, diffuses into the *a*-Si layers upon rapid thermal annealing for 5 minutes at 600 °C and two completely separated Pt_xSi layers are formed.

A vacuum compatible, PID-controlled resistive heater for use inside a scanning electron microscope (SEM) was designed, fabricated, and tested to ultimately further

study the silicide-based release through *in situ* experiments.³ Figure 42 shows a schematic of the heater design, featuring: cross-sectional and planar sample areas, a first thermocouple to assess the sample temperature, and a second thermocouple to monitor the temperature of the SEM stage. The heater body is made out of copper due to its high thermal conductance, whereas the heater shell is made out of low thermal-conducting macor ceramic.

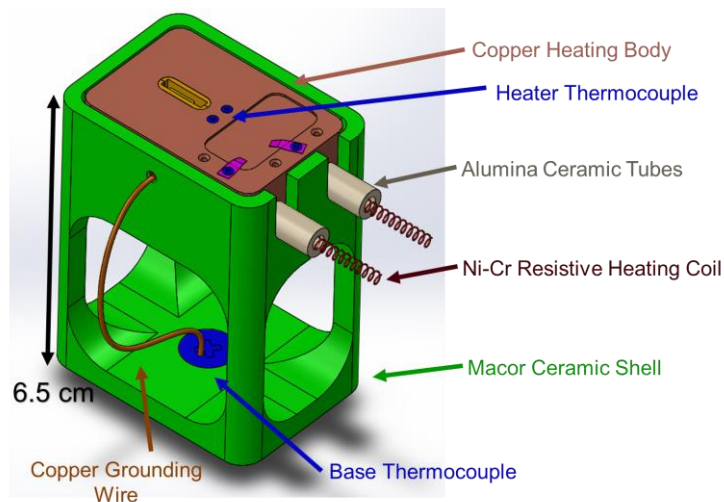


FIGURE 42: Schematic of a resistive, passive-cooled heater for use in a scanning electron microscope (SEM).

The functionality of the heater and its custom-made LabVIEW (National Instruments Corp., Austin, TX) control panel was tested using a SAC305 soldering alloy (96.5% Sn, 3% Ag, 0.5% Cu, $T_{\text{melt}} = 217\text{-}218\text{ }^{\circ}\text{C}$). The alloy started to melt at a

³ The resistive heater was designed, fabricated, and tested in collaboration with D. B. Durham (Department of Materials Science and Engineering, University of Pennsylvania).

measured temperature of $\sim 217\text{ }^{\circ}\text{C}$, providing an extremely accurate temperature measurement.

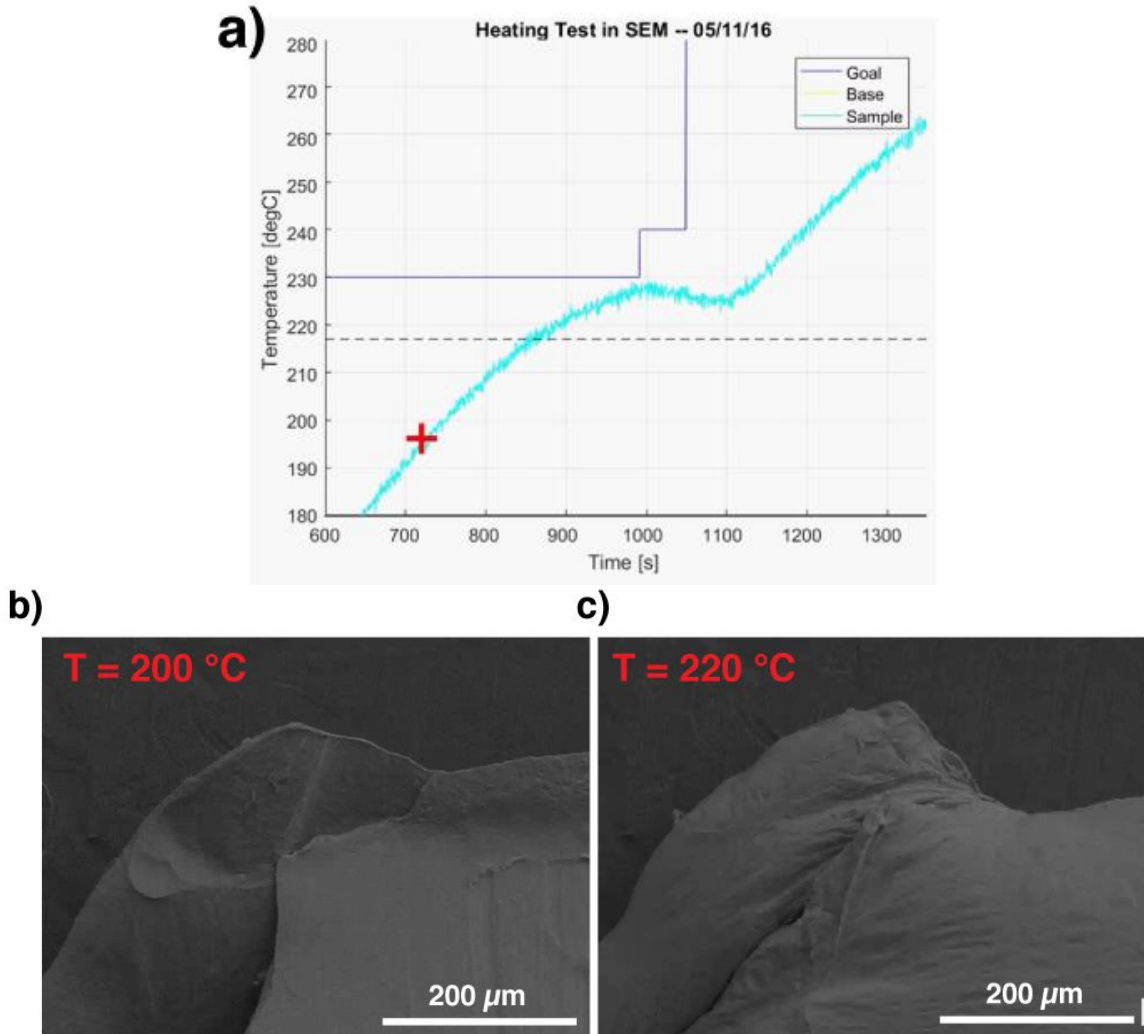


FIGURE 43: Screenshots of the scanning electron microscope (SEM) image and temperature measurement during heating of a SAC305 soldering alloy. a) Graph of the time-temperature recording during experiment. b) SEM image of the solder alloy at a temperature below T_{melt} . c) SEM image of the solder alloy at a temperature just above T_{melt} .

The fabricated SEM heater allows for the *in situ* observation of the gap formation of a-Si/Pt layer stacks as shown in Figure 41 and will thereby enable a quantitative study of the Pt_xSi-based release process. By varying the a-Si and Pt layer thicknesses, the occurring shrinkage can be accurately measured and the ideal gap formation recipe can be developed.

3.3 Platinum silicide stoichiometry and properties by design

3.3.1 Importance of metal silicide thin films

Solid-state reactions to form metal silicides (Me_xSi) have been widely studied since the early 1980s, and were later used for Ohmic contacts, Schottky barrier contacts, gate electrodes, local interconnects, and diffusion barriers in the microelectronics industry [12-16]. Recently, Me_xSi have become attractive as thermoelectric materials due to their metal-like electrical properties combined with semiconductor-like thermal transport [17-20]. Their mechanical robustness and thermal stability makes them promising for high temperature engines [12], and combined with their high electrical conductivity renders them of interest as next-generation contact materials for nanoelectromechanical (NEM) switches [7,21,22]. Me_xSi are also considered as alternative plasmonic materials [23], as well as advanced materials for lithium-ion batteries [24]. One dimensional transition metal silicides have been studied for their exotic properties such as room temperature ferromagnetism and field emission [25-27]. However, most investigations and applications rely on equilibrium Me_xSi phases and do

not attempt to control the preceding solid-state diffusion reactions that lead to Me_xSi formation to form specific silicide stoichiometries with desired properties [28].

Tailoring the physico-chemical properties of Me_xSi through the precise control of their stoichiometry and crystal structure would allow the design of materials suitable for specific applications. Our previous work has shown that the stoichiometry of platinum silicide (Pt_xSi) films greatly influences their electrical conductivity: Pt-rich silicides exhibit metallic-like conductivity, while Si-rich silicides are more resistive [21,22]. This makes the metal-rich silicide phase Pt_3Si particularly interesting for a variety of applications, *e.g.*, as wear-resistive electrical coatings for atomic force microscopy probes or as contact material for nanoelectromechanical switches, since these films offer similar mechanical robustness as Si-rich silicides while exhibiting improved electrical conductivity [21,22]. Additionally, the nanoscale adhesion of Pt_xSi films to Pt tips decreases from Pt-rich to Si-rich films. To ensure precise stoichiometric control, it is necessary to understand the synthesis mechanism at the atomic scale and the influence of initial precursor concentration in the ensuing chemical transformation. *In situ* TEM experiments have opened up new frontiers for gaining such understanding [29-33]. Here, we use *in situ* TEM to explore two routes to precisely control the stoichiometry of thin Me_xSi films, using Pt_xSi as a potential model system involving face-centered cubic transition metals. In the first, source-limited solid-state diffusion, precise control of the precursor thin film layer thicknesses predetermines the achievable silicide stoichiometry via annealing. In the second, kinetically-limited solid-state diffusion, a precisely controlled time-temperature regime obtains the desired silicide stoichiometry and phase.

3.3.2 *In situ* measurements to elucidate platinum silicide formation mechanisms

Samples of different Pt:*a*-Si film thickness ratios were fabricated as precursors to form Pt_xSi films using the source-limited solid-state diffusion approach while assessing their crystal structures and formation sequence. PELCO 50 nm silicon nitride (Si₃N₄) support TEM grids (Ted Pella Inc., Redding, CA) were sputter-coated with thin layers of *a*-Si and Pt, whose thicknesses were chosen to obtain nearly-pure phases of Pt₃Si, Pt₂Si and PtSi upon annealing. The Pt and *a*-Si depositions were conducted sequentially in the same deposition system under maintained vacuum. This minimizes contaminant adsorption between the layers and the oxidation of the *a*-Si - both inhibiting factors for silicidation. The coated grids were removed from the deposition system and characterized using a TEM (JOEL 2100 TEM, JEOL Ltd., Tokyo, Japan). An *in situ* heating TEM sample holder (Gatan Inc., Pleasanton, CA) was used to anneal the samples in the TEM while continuously recording the electron diffraction pattern (Figure 44), which allowed determination of the crystal structure and formation sequence of the different Pt_xSi phases. All samples were subjected to similar annealing treatments that included a 10 min hold at 500 °C followed by a 10 min hold at 600 °C.

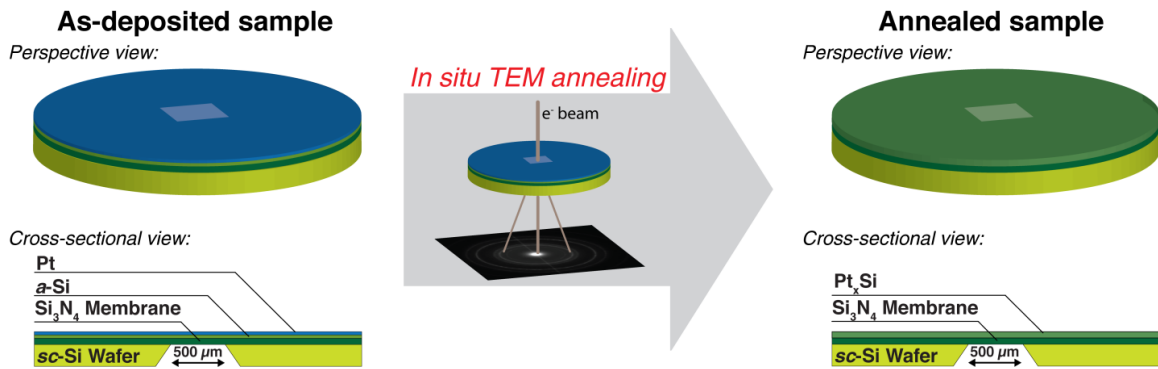


FIGURE 44: Schematics of the as-deposited and annealed samples and the used in situ TEM annealing technique

The Pt and *a*-Si films were sputter deposited in a Denton Vacuum Explorer 14 sputterer (Denton Vacuum Inc, Moorestown, NJ) with a purity of 99.99 % for both films. Pt was deposited in DC mode at 450 W and *a*-Si in AC mode at 230 W. The Pt nanoparticles were produced by coating an *a*-Si film with approx. 10 nm of Pt, which does not wet the surface completely, forming nanoparticles instead of a continuous film.

An *in situ* heating TEM sample holder (Gatan Inc., Pleasanton, CA) was used to form Pt_xSi inside the TEM. The heating holder is equipped with a thermocouple sensitive to ± 1 °C. All source-limited solid-state diffusion samples (Figure 45 and Figure 46) were subject to a similar annealing treatment which included the heating up to 500 °C (heating rate: 30 °C/min) and holding at 500 °C for 10 min. This was followed by heating up to 600 °C (heating rate: 30 °C/min), holding at 600 °C for 10 min and rapid cooling to 50 °C (cooling rate: 85 °C/min). The kinetically-limited solid-state diffusion sample was heated up with a heating rate of 30 °C/min until 200 °C and rapidly quenched to conserve the Pt₃Si phase. Subsequently, the sample was heated up to 300 °C (heating rate: 30

°C/min) to form Pt₂Si followed by rapid quenching. Finally, the sample was heated up to 500 °C (heating rate: 30 °C/min) to form PtSi and subsequently cooled down.

All TEM experiments were performed using a JEOL 2100 thermionic emission source TEM (JEOL Ltd., Tokyo, Japan). An accelerating voltage of 200 kV was used with a beam current of 106 µA resulting in a current density of 275 pA/cm².

The chemistry of the near-surface region was investigated by XPS using a customized XPS spectrometer (VG Scienta AB, Uppsala, Sweden) [10]. XPS analyses were performed using a monochromatic Al K_α source (photon energy: 1486.6 eV). The residual pressure in the analysis chamber was constantly less than 1·10⁻⁸ Torr. The spectrometer was calibrated according to ISO 15472:2001 with an accuracy of ± 0.05 eV. Survey and high-resolution spectra were acquired in constant-analyzer-energy mode with the pass energies of 200 eV and 100 eV, respectively. The full width at half-maximum (FWHM) of the peak-height for the high-resolution Ag 3d_{5/2} signal of a sputter-cleaned Ag sample was 0.57 eV. The spectra were processed using CasaXPS software (v.2.3.16, Casa Software Ltd., Wilmslow, Cheshire, U.K.). Background subtraction was performed using the Shirley-Sherwood method. The quantitative evaluation of XPS data, as described in [11], was based on integrated intensity using a first-principles model and applying Powell's equation. The inelastic mean free path was calculated using the TPP-2M formula [34]. Curve synthesis for the Pt 4f peaks was performed constraining the integrated intensity ratio of these two signals to 3:4 and their energy separation to 3.33 eV. The reference energies for Pt 4f_{7/2} peaks are 71.05 eV, 71.55 eV, 72.18 eV, and 72.75 eV for Pt, Pt₃Si, Pt₂Si, and PtSi respectively and are in agreement with literature values [21]. The Pt 4f peaks have been chosen to determine sample surface chemistry due to their high intensity and the high sensitivity of their position to the Pt_xSi

stoichiometry, in contrast to the less intense and less stoichiometrically-sensitive position of the Si 4p peaks.

3.3.3 Source-limited solid state diffusion

Figure 45 presents the results from the source-limited solid-state diffusion experiments. The Pt:*a*-Si film thickness ratios were chosen to be 1:3 (Pt:*a*-Si=1:3) to form PtSi, 1:1 (Pt:*a*-Si=1:1) for Pt₂Si, and 2:1 (Pt:*a*-Si=2:1) for Pt₃Si. Figure 45a shows representative selected-area electron diffraction (SAD) patterns of an as-deposited Pt/*a*-Si sample and the resulting Pt_xSi film. The diffraction pattern of the as-deposited film (top-right quadrant, Figure 45a) matches the theoretical pattern for Pt (the amorphous structures of the *a*-Si film and Si₃Ni₄ membrane do not produce any diffraction rings). Theoretical diffraction patterns were calculated using the theoretical crystal structures of Pt and Pt_xSi phases and CrystalMaker software (CrystalMaker Software Ltd., Oxfordshire, United Kingdom). For the annealed Pt:*a*-Si=2:1 sample, the 1:1 sample, and the 1:3 sample, the predominant diffraction rings match the theoretical diffraction pattern for monoclinic Pt₃Si (bottom-right quadrant, Figure 45a), tetragonal Pt₂Si (bottom-left quadrant), orthorhombic PtSi (top-left quadrant) respectively. Figure 45b summarizes the formation process of the Pt₃Si, Pt₂Si and PtSi films. The formation process of all three starts with the formation of Pt₃Si. This is the only phase observed for the Pt:*a*-Si=2:1 sample, and was stable throughout the annealing procedure. However, considerable grain-growth occurred with continued heating up to 600 °C as a result of the low Pt₃Si formation temperature of 200 °C, resulting in the appearance of high-intensity diffraction spots (bottom-right quadrant, Figure 45a). For the Pt:*a*-Si=1:1 and Pt:*a*-Si=1:3 samples, Pt₂Si formation followed Pt₃Si formation at approximately 300-325

°C. This phase remained stable for the Pt:*a*-Si=1:1 sample, whereas for the Pt:*a*-Si=1:3 sample, PtSi formed around 400-425 °C.

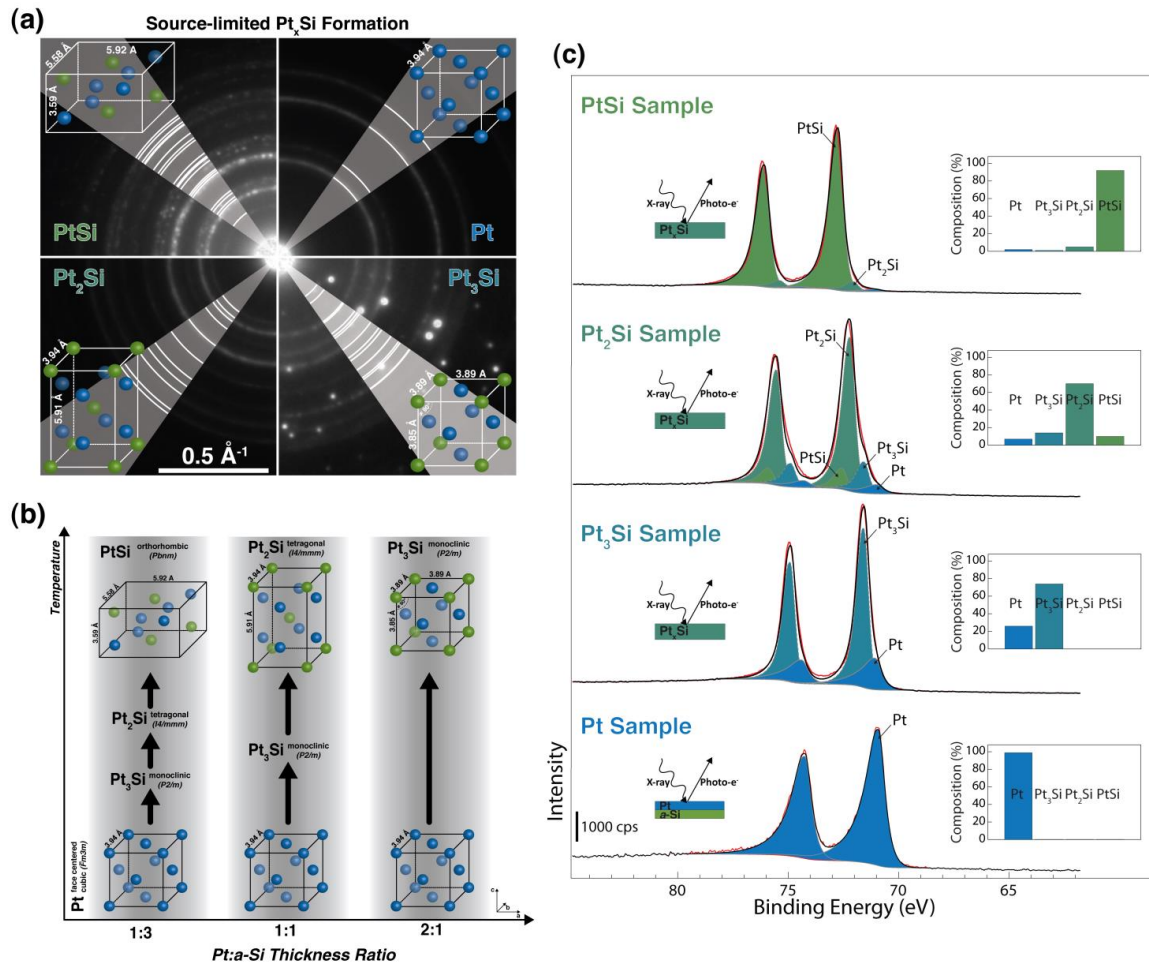


FIGURE 45: Source-limited Pt_xSi formation. a, Electron diffraction pattern of as-deposited Pt and Pt_3Si , Pt_2Si , and PtSi films produced using source-limited solid-state diffusion. Grey slices indicate diffraction ring positions according to the theoretical crystal structure shown schematically for each phase. b, Schematic of the source-limited solid-state diffusion process which utilizes precise control of the Pt and a-Si precursor film thicknesses to predetermine the desired Pt_xSi phase. c, High-resolution XPS spectra of the Pt 4f peaks for as-deposited Pt and resulting Pt_xSi formed on TEM grids using source-limited solid-state diffusion. PtSi sample (Pt:a-Si=1:3): quantitative analysis indicates formation of 92% of PtSi. Pt_2Si sample (Pt:a-Si=1:1): quantitative analysis indicates formation of 70% Pt_2Si . Pt_3Si sample (Pt:a-Si=2:1): quantitative analysis indicates formation of 74% Pt_3Si . Pt sample: quantitative analysis indicates the presence of pure metallic Pt

The annealed grids were characterized using high-resolution angle-resolved X-ray photoelectron spectroscopy (XPS) to determine the stoichiometry of the films (Figure 45c) [10]. In the high-resolution XPS spectrum of as-deposited Pt ("Pt Sample"), the Pt $4f_{7/2}$ peak position (71.05 ± 0.05 eV) and lineshape are characteristic of metallic platinum, thus confirming the TEM diffraction pattern displayed in Figure 45a (top-right quadrant). The high-resolution XPS spectrum of the annealed Pt:*a*-Si=2:1 sample ("Pt₃Si Sample") in Figure 45c shows a peak shift assigned to Pt₃Si, consistent with the diffraction behavior in Figure 1a (bottom-right quadrant). Quantitative analysis (Figure 45c, insets) determined that this sample consists of 74% Pt₃Si and 26% metallic Pt. Figure 45c also shows the high-resolution XPS spectra of the annealed Pt:*a*-Si=1:1 sample ("Pt₂Si Sample"). Quantitative XPS analysis showed that this sample consists of 70% Pt₂Si phase, while the remaining 30% are a mixture between metallic Pt, Pt₃Si and PtSi (7% Pt, 14% Pt₃Si, 9% PtSi). The high-resolution XPS spectra of the annealed Pt:*a*-Si=1:3 sample ("PtSi Sample") is displayed in Figure 45c. This sample is composed of 92% PtSi phase (remainder: 2% Pt, 1% Pt₃Si, 5% Pt₂Si), which matches well with the PtSi diffraction pattern in Figure 45a (left-top quadrant). The quantitative XPS analysis confirmed the Pt_{*x*}Si stoichiometries determined using *in situ* TEM electron diffraction. The overall results confirm that the stoichiometry of Pt_{*x*}Si thin films can be precisely tuned using source-controlled solid-state diffusion.

3.3.4 Kinetically-limited solid state diffusion

Samples with Pt:*a*-Si thickness ratio of 1:3 were produced to test if precise control of the temperature-time regime during silicidation can be used to tune the Pt_xSi stoichiometry (*i.e.* kinetically-limited solid-state diffusion). This Pt:*a*-Si thickness ratio will ultimately lead to PtSi formation, while passing the Pt_3Si and Pt_2Si stoichiometries (as seen in Figure 45b). Figure 46 summarizes the results. Figure 46a shows SAD electron diffraction images recorded at room temperature and after the annealing process has been halted at specific temperatures to produce highly selective Pt_xSi phases. The as-deposited sample, which exhibited a Pt electron diffraction pattern (top-right quadrant, Figure 46a), was heated up to 200 °C to form Pt_3Si and then quickly cooled down to retain this phase at room temperature (bottom-right quadrant). The Pt_3Si film was subsequently heated up to 300 °C to form Pt_2Si and quickly cooled down to retain this phase at room temperature (bottom-left quadrant). Finally, the formed Pt_2Si film was heated up to 500 °C so that PtSi is formed and subsequently cooled down (top-left quadrant).

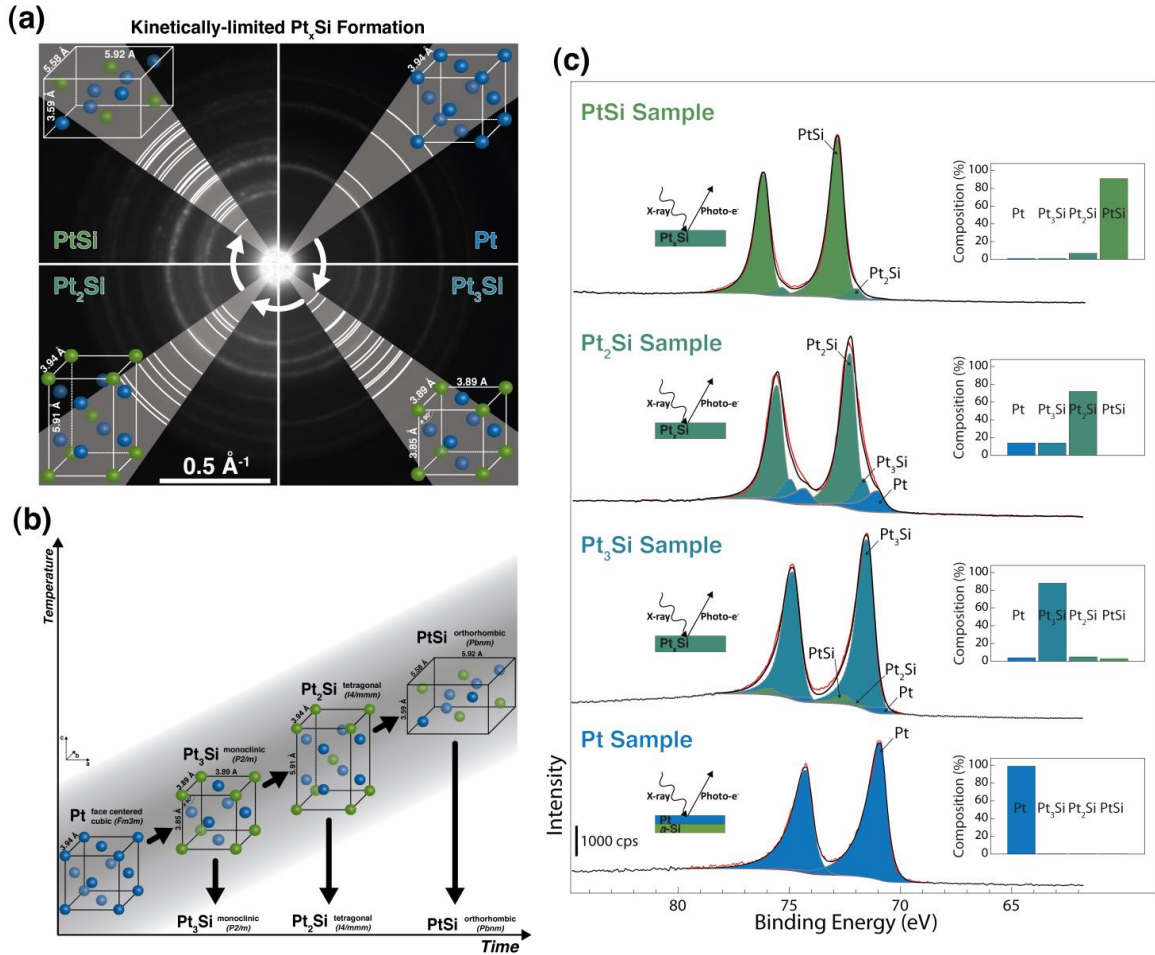


FIGURE 46: Kinetically-limited Pt_xSi formation. a, Electron diffraction pattern of as-deposited Pt and Pt_3Si , Pt_2Si , and $PtSi$ films produced using kinetically-limited solid-state diffusion. Grey slices indicate diffraction ring positions according to the theoretical crystal structure shown schematically for each phase. b, Schematic of the kinetically-limited solid-state diffusion process which utilizes precise control of the temperature-time regime to obtain the desired Pt_xSi phase. c, High-resolution XPS spectra of the Pt_{4f} peaks for as-deposited Pt and resulting Pt_xSi formed on TEM grids using kinetically-limited solid-state diffusion. *PtSi sample* (heated to 200 °C): quantitative analysis indicates formation of 91% of $PtSi$. *Pt₂Si sample* (heated to 300 °C): quantitative analysis indicates formation of 72% Pt_2Si . *Pt₃Si sample* (heated to 500 °C): quantitative analysis indicates formation of 88% Pt_3Si . *Pt sample*: quantitative analysis indicates the presence of pure metallic Pt.

The annealed TEM grid was characterized using XPS to determine the stoichiometry of the Pt_xSi phases formed (Figure 46c). The results presented indicate a similar phase selectivity for kinetically-limited diffusion (88% Pt_3Si , 72 % Pt_2Si , 91% $PtSi$) and for the source-limited case (74% Pt_3Si , 70% Pt_2Si , 92% $PtSi$). Comparison of the kinetically-limited diffraction patterns (Figure 46a) with those from the source-limited experiments (Figure 45a) show that the peak positions and intensity ratios are similar (Figure 47), which confirms the similar composition of the Pt_xSi phases for kinetically-limited and source-limited experiments measured using XPS. Figure 46a also shows that all phases formed exhibit minimal grain growth. Dark-field TEM results also indicated that the formed Pt_xSi films are nanocrystalline. Figure 46b summarizes the kinetically-limited Pt_xSi formation experiments, and shows that the stoichiometry of Pt_xSi films was precisely tunable by controlling the temperature-time regime during the annealing. The *in situ* TEM experiments presented in Figure 46 prove that kinetically-controlled solid-state diffusion is a highly effective way to tune the Pt_xSi stoichiometry.

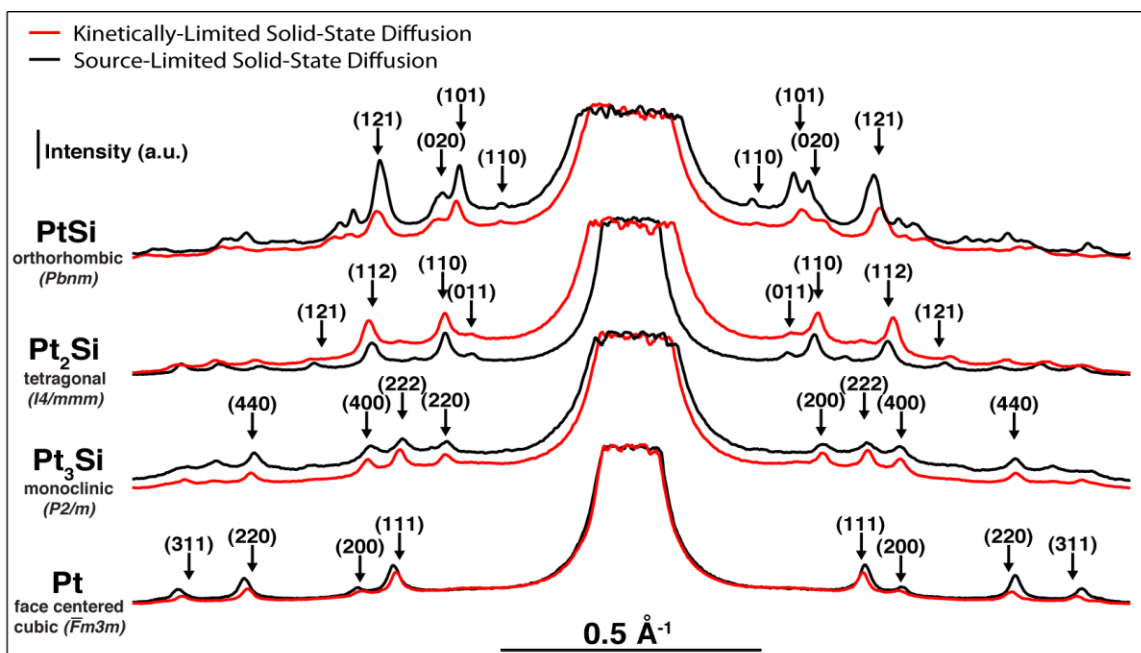


FIGURE 47: Comparison of diffraction pattern intensity distributions obtained from the kinetically-limited and source-limited solid-state diffusion samples. Peak locations and intensity ratios are similar for both methods and indicate that the two methods produce similar Pt_xSi compositions. The theoretical peak positions of the four strongest peaks are indicated by the downward arrows.

The annealed TEM grid was characterized using XPS to determine the stoichiometry of the Pt_xSi phases formed (Figure 46c). The results presented indicate a similar phase selectivity for kinetically-limited diffusion (88% Pt_3Si , 72 % Pt_2Si , 91% $PtSi$) and for the source-limited case (74% Pt_3Si , 70% Pt_2Si , 92% $PtSi$). Comparison of the kinetically-limited diffraction patterns (Figure 46a) with those from the source-limited experiments (Figure 45a) show that the peak positions and intensity ratios are similar (Figure 47), which confirms the similar composition of the Pt_xSi phases for kinetically-limited and source-limited experiments measured using XPS. Figure 46a also shows that all phases formed exhibit minimal grain growth. Dark-field TEM results also

indicated that the formed Pt_xSi films are nanocrystalline. Figure 46b summarizes the kinetically-limited Pt_xSi formation experiments, and shows that the stoichiometry of Pt_xSi films was precisely tunable by controlling the temperature-time regime during the annealing. The *in situ* TEM experiments presented in Figure 46 prove that kinetically-controlled solid-state diffusion is a highly effective way to tune the Pt_xSi stoichiometry.

3.3.5 Specifics of Pt_3Si formation

Both source-limited and kinetically-limited solid-state diffusion experiments (Figure 45, Figure 46) were able to produce highly selective Pt_3Si films, which have not been experimentally reported before or observed during Pt/sc-Si experiments. The well-studied Pt/sc-Si system is characterized by the specific Pt_xSi formation sequence of Pt diffusing into sc-Si around 250-300 °C to form the intermediate Pt_2Si phase. After all Pt is consumed, sc-Si will diffuse into Pt_2Si at 300-450 °C to form the thermodynamically stable PtSi phase [5,35]. We hypothesize that the amorphous nature of the a-Si film used in our experiments alters the diffusion behavior compared to sc-Si, which leads to the formation of the Pt_3Si phase. The Pt_3Si phase is formed due to the fact that in the Pt/a-Si system, a-Si acts initially as the dominant diffusing species (DDS) in contrast to the Pt/sc-Si system where Pt is initially the DDS. The distribution of bonding characteristics of a-Si compared to sc-Si leads to reduced activation energies for a-Si self-diffusion of up to 27% compared to those for sc-Si [36]. Thus, a-Si becomes mobile at lower temperatures than sc-Si. In addition to the increased mobility of a-Si, the Pt diffusivity is drastically reduced in a-Si compared to sc-Si. Pt has a diffusion coefficient at 500 °C of $\sim 5 \cdot 10^{-18}$ m²/s in a-Si [37], whereas the diffusion coefficient of Pt in sc-Si is $\sim 5 \cdot 10^{-16}$ m²/s [38], which means that Pt diffuses two orders of magnitude faster in sc-Si

than in *a*-Si. Both the increased *a*-Si and reduced Pt diffusivity could be the reason for the proposed *a*-Si diffusion into Pt and subsequent formation of Pt₃Si for the Pt/*a*-Si system. Additionally, *a*-Si possesses a higher free energy compared to *sc*-Si, which could result in a greater driving force for Pt₃Si formation. One can also consider the Walsler-Bené first phase rule [39], which says that the first phase to form in binary reaction couples is the compound with the highest congruent melting temperature adjacent to the lowest-temperature eutectic. For the Pt-Si system, Pt₃Si is closest to the lowest-temperature eutectic and would be expected to form as observed here.

The observed Pt₃Si formation can also be understood by the high degree of resemblance between the Pt and Pt₃Si crystal structures, including the lattice parameter. The Pt₃Si unit cell can be imagined as a Pt unit cell with the corner atoms replaced by Si. The ease of transformation between Pt and Pt₃Si without the need for massive atomic restructuring is thought to be the reason for such low temperature metamorphosis.

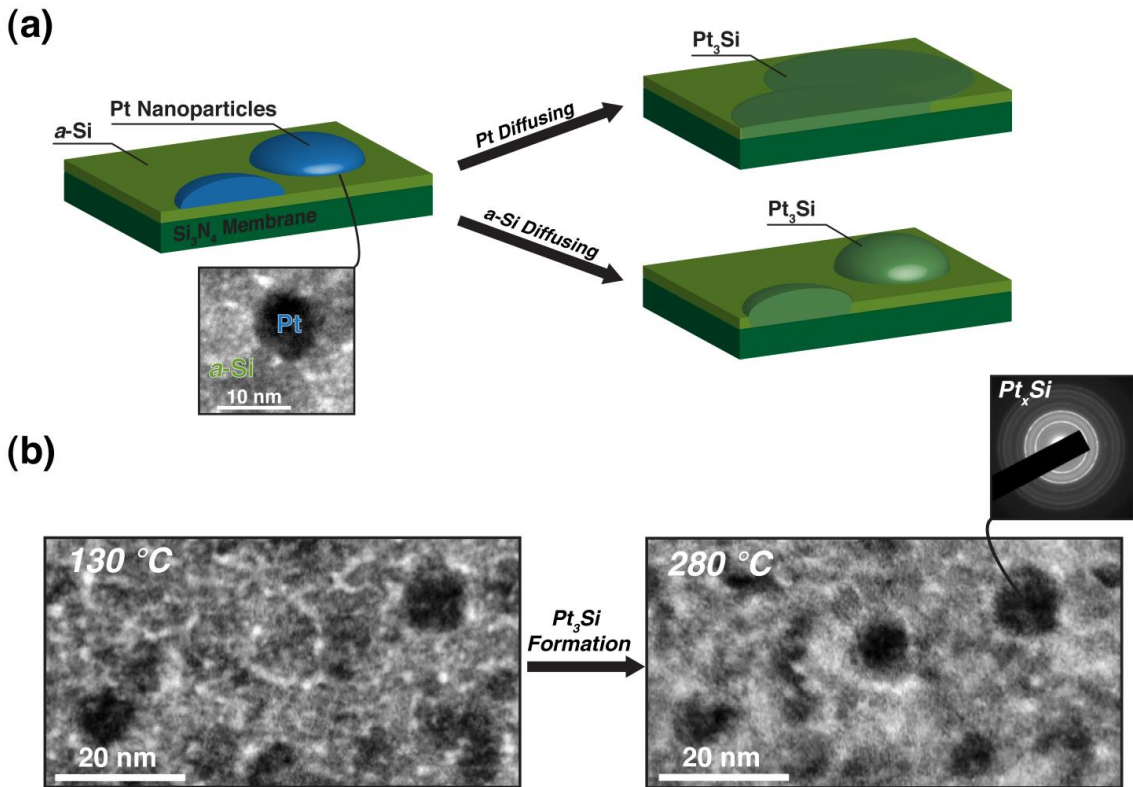


FIGURE 48: Determination of the dominant diffusing species (DDS) during Pt_3Si formation. a, The schematic and the TEM image on the left shows the as-deposited sample: an $a\text{-Si}$ film covered by Pt nanoparticles. Annealing will lead to Pt_3Si formation. If Pt is the DDS, then the Pt nanoparticles will diffuse into the underlying $a\text{-Si}$ layer and the Pt-containing region (high Z contrast) will appear larger in TEM images. If Si is the DDS, then the nanoparticle shape and size will be nearly preserved and no major change of the high Z contrast region will be visible in the TEM. b, TEM images of several Pt nanoparticles before (at $130\text{ }^\circ\text{C}$) and after ($280\text{ }^\circ\text{C}$) Pt_3Si formation. The overall shape and size of the Pt and Pt_3Si nanoparticles is similar, indicating that Pt_3Si formation occurs through diffusion of $a\text{-Si}$ into Pt. The electron diffraction pattern shows that Pt_3Si particles were formed.

To demonstrate that $a\text{-Si}$ is the diffusing species instead of Pt and that this leads to Pt_3Si formation, we coated a Si_3N_4 -support TEM grid with $a\text{-Si}$ and, subsequently, with

Pt nanoparticles of ~10 nm diameter (as shown in Figure 48a). Figure 48a shows a schematic and TEM image of the as-deposited sample together with the theoretical pathways leading to the formation of Pt₃Si, *i.e.*, the diffusion of Pt in *a*-Si or the diffusion of *a*-Si in Pt. If Pt is the DDS, then the Pt nanoparticles will diffuse into the underlying *a*-Si layer and a TEM Z-contrast image will show significant broadening of the Pt-containing regions. If, on the other hand, *a*-Si is the diffusing species as proposed here, then the general shape of the Pt nanoparticles should be conserved during Pt₃Si formation as only a small amount of *a*-Si is diffusing into the nanoparticles. Figure 48b shows an area of the sample with several Pt nanoparticles before (at 130 °C) and after (at 280 °C) Pt₃Si formation. The overall shape and size of the nanoparticles do not undergo any significant changes due to Pt₃Si formation. This result indicates that *a*-Si is the DDS, and that it diffuses into Pt to form Pt₃Si, which means that the occurrence of Pt₃Si in *a*-Si-based silicidation experiments is entirely due to the high diffusivity of *a*-Si, and that such films are not attainable using *sc*-Si. The diffusion of *a*-Si into Pt nanoparticles to form Pt₃Si should lead to a small increase in particle radius of approximately 9% (using a Pt density of 21.45 g/cm³ and a Pt₃Si density of 17.47 g/cm³). A comparison of the nanoparticle sizes before and after thermal annealing indeed indicates an increase in particle radius, whose relative change is in agreement with the prediction (Figure 49). This supports our assumption of *a*-Si acting as DDS. While our results point towards drastically changed diffusion mechanisms during Pt/*a*-Si silicidation leading to Pt₃Si formation, further tracer diffusion or Rutherford backscattering experiments will be necessary to precisely elucidate the occurring diffusion mechanisms and reaction thermodynamics.

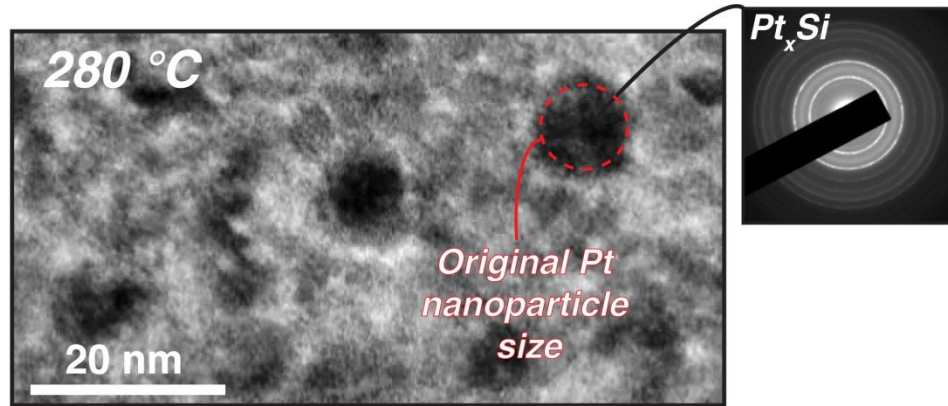


FIGURE 49: TEM image of formed Pt_3Si nanoparticles. Comparison of the initial Pt and resulting Pt_3Si nanoparticle sizes ($r_{\text{Pt}} \approx 8.8 \text{ nm}$, $r_{\text{Pt}_3\text{Si}} \approx 10.0 \text{ nm}$) show a particle radius increase due to Pt_3Si formation of similar magnitude then the theoretical value of 9%.

The Pt_3Si films resulting from Pt/a-Si annealing have several advantages over PtSi films that result from Pt/sc-Si. Most notably, Pt_3Si possesses similar mechanical properties as PtSi (~50% greater hardness and modulus compared to Pt) [21,22], but with a higher electrical conductivity [21,22]. The increased hardness of Pt_3Si can also be understood from our source-limited heating experiments where we observe not only grain coarsening but also formation of anti-phase boundaries (APBs) (Figure 50), which are two dimensional defects commonly found in L_{12} type crystal structures [40-43]. These APBs will hinder dislocation motion and thereby plastic deformation.

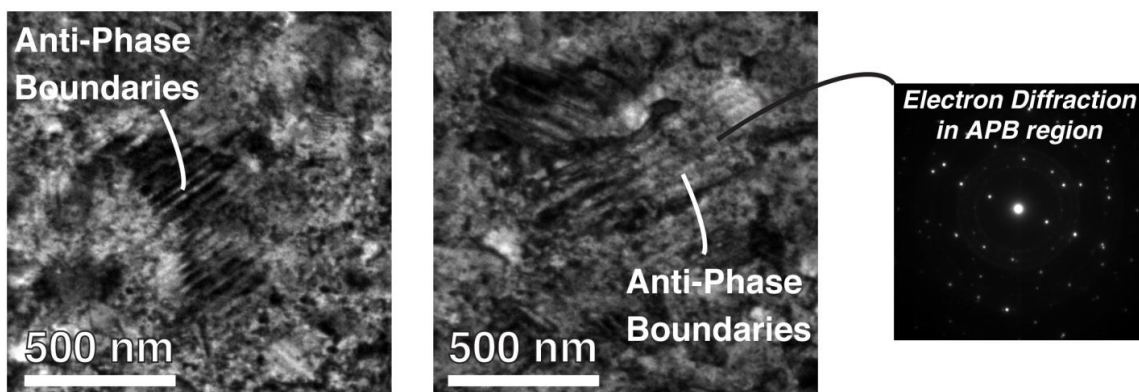


FIGURE 50: TEM images of anti-phase boundaries (APBs) formed in Pt₃Si and electron diffraction image of APB shows single-crystal diffraction spots.

3.3.6 Conclusions

In summary, we present two routes to control and pre-determine the stoichiometry, crystal structure and thereby the properties of thin Pt_xSi films. Both the precise control of the precursor film thicknesses (source-limited solid-state diffusion) and the precise control of the temperature-time regime during silicidation (kinetically-limited solid-state diffusion) were able to produce highly selective Pt₃Si, Pt₂Si, and PtSi films. These two routes to adjust the silicide stoichiometry, crystal structure and properties may also be applicable to other metal silicides and may give access to phases not attainable using traditional formation routes. In particular, the lessons learned from the Pt_xSi system may be applicable to metal silicides formed from other face-centered cubic transition metals such as Ni, Cu, Au, Pd, Ag, and Rh. We also show that the diffusion mechanism during Pt_xSi formation using Pt/*a*-Si bilayers significantly differs from the well-studied Pt/*sc*-Si system, allowing the formation of Pt₃Si - a stoichiometry with significant potential as an electrical conductive and wear-resistive coating.

3.4 Electronic properties of platinum silicide films and their control

Metal silicide (Me_xSi) thin films were extensively studied in the 1980s and have found use in the microelectronics industry as materials for electronic contacts, local interconnects, and diffusion barriers [12]. Recently, Me_xSi regained scientific attention as they are considered candidate materials for a variety of novel applications, such as plasmonics [23], lithium-ion batteries [24], field emitters [25-27], thermoelectrics [17-20], field-effect transistors [44], and nanoelectromechanical switches [7,21,22,45-47]. The increasing popularity of Me_xSi is a consequence of their metal-like electrical properties, semiconductor-like thermal transport, mechanical robustness, and thermal stability. However, Boltasseva *et al.* [23] and Cheng *et al.* [24], among others, pointed out that the composition and properties of Me_xSi need to be carefully optimized to fully utilize their potential in next-generation applications. We recently presented a methodology to precisely tune the composition of Me_xSi thin films by means of controlled solid-state diffusion [45]. This allows for the formation of platinum silicide (Pt_xSi) thin films over a wide composition range ($1 \leq x \leq 3$), including the novel Pt_3Si stoichiometry, with an associated wide range of mechanical and electronic properties [21,22,45]. While it is known that the Me_xSi composition strongly affects the resulting electrical, mechanical, and adhesive properties [21,22], systematic studies determining the effect of Me_xSi composition on specific properties are lacking. Here, we compare valence band (VB) X-ray photoelectron spectroscopy (XPS) measurements with calculations⁴ of the density of

⁴ The density functional theory calculations presented in this section were performed by Y. Qi and J. Yang under the supervision of A. M. Rappe (Department of Chemistry, University of Pennsylvania).

states (DOS) around the Fermi edge to elucidate the relationship between composition and electronic structure/properties for Pt_xSi thin films.

Using source-limited solid-state diffusion (*i.e.*, films are formed by annealing of sequentially-deposited Pt and Si thin films of specific thickness ratios) [45], we fabricated Pt_xSi thin films of Pt_3Si , Pt_2Si , and PtSi . These films were interrogated using high-resolution VB XPS measurements to determine the DOS at the Fermi edge, which accurately determines the electronic structure and many of the electronic properties of these Pt_xSi films. A high DOS at the Fermi edge is a requirement for having high electrical conductivity [44]. The Fermi edge shape therefore provides an indication of the electronic character of the tested material (metal, semimetal, or semiconductor) as shown schematically in Figure 51a. Metals are characterized by a large quantity of charge carriers (high density of states) near the Fermi edge that allows them to be efficient electrical conductors. Semimetals possess a significantly reduced DOS at the Fermi edge without an energy band gap (which, combined with their typically higher Seebeck coefficient and lower thermal conductivities compared to metals, makes them suitable thermoelectric materials) [48]. The Fermi edges of semiconductors are located inside the band gap without any electronic states at the edge. Since XPS probes the occupied states of a material (see Figure 51b), the spectral features of a valence band XPS spectrum directly correlate to the DOS. This relationship allows us to directly compare XPS measurements with theoretical DOS calculations.

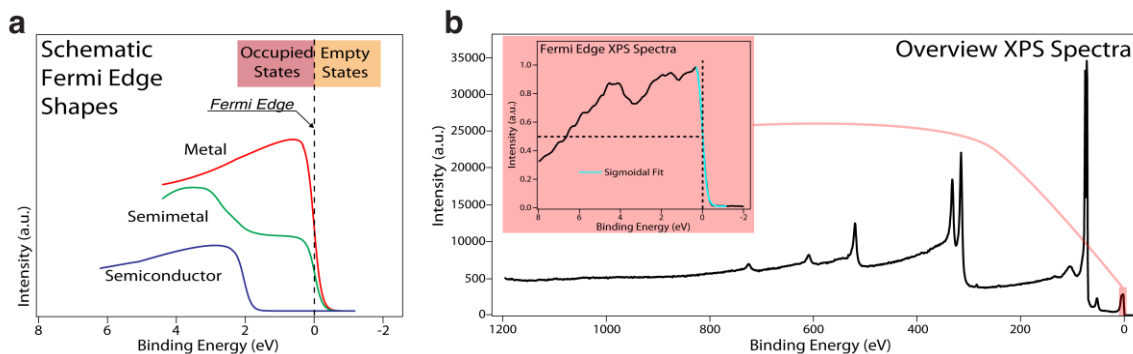


FIGURE 51: Fermi edge shapes and locations in XPS spectra. a. Schematic Fermi edge shape of a metal, a semimetal, and a semiconductor. The intensity of charge carriers at the Fermi edge reduces from metals to semimetals and becomes zero for semiconductors. b. Location of the Fermi edge within an experimental Pt XPS spectrum. The Fermi edge is located at a binding energy value of 0 eV.

Figure 52 shows the results of the VB XPS measurements and the theoretical DOS calculations for [Pt], [Pt₃Si], [Pt₂Si], and [PtSi] films (the “[...]” notation refers to the dominant phase of four respective mixtures achieved experimentally as shown in Figure 52c). The composition of the produced Pt_xSi films was determined using quantitative XPS (see *Experimental and Computational Methods*). This demonstrated the phase selectivity as shown in Figure 52c; the [Pt₃Si] film was 74% Pt₃Si, the [Pt₂Si] film was 70% Pt₂Si, the [PtSi] film 92% PtSi, and the [Pt] film was 100% Pt. These exact compositions were also employed in the theoretical DOS calculations using a linear combination approach to ensure a better comparability of the results. The VB XPS measurements show a direct correlation between the Si concentration and the Fermi edge shape (Figure 52a). This agrees with recent work by Fryer & Lad, who performed VB XPS measurements of co-deposited Pt_xSi films (1 ≤ x ≤ 3) [49]. The experimental DOS at the Fermi edge systematically decreases with increasing Si concentration from Pt

towards PtSi. The analyzed films show metallic and reduced-metallic Fermi edge shapes in the case of Pt and Pt₃Si, respectively, and typical semimetallic behavior for the Pt₂Si and PtSi films. The theoretical DOS calculations show a similar reduction of the DOS at the Fermi edge from Pt to PtSi. Additionally, the calculated DOSs for Pt, Pt₂Si, and PtSi are similar to those reported in previous works by Bentmann *et al.* [50] and Franco *et al.* [51]. No DOS calculations for Pt₃Si have been previously reported in the literature.

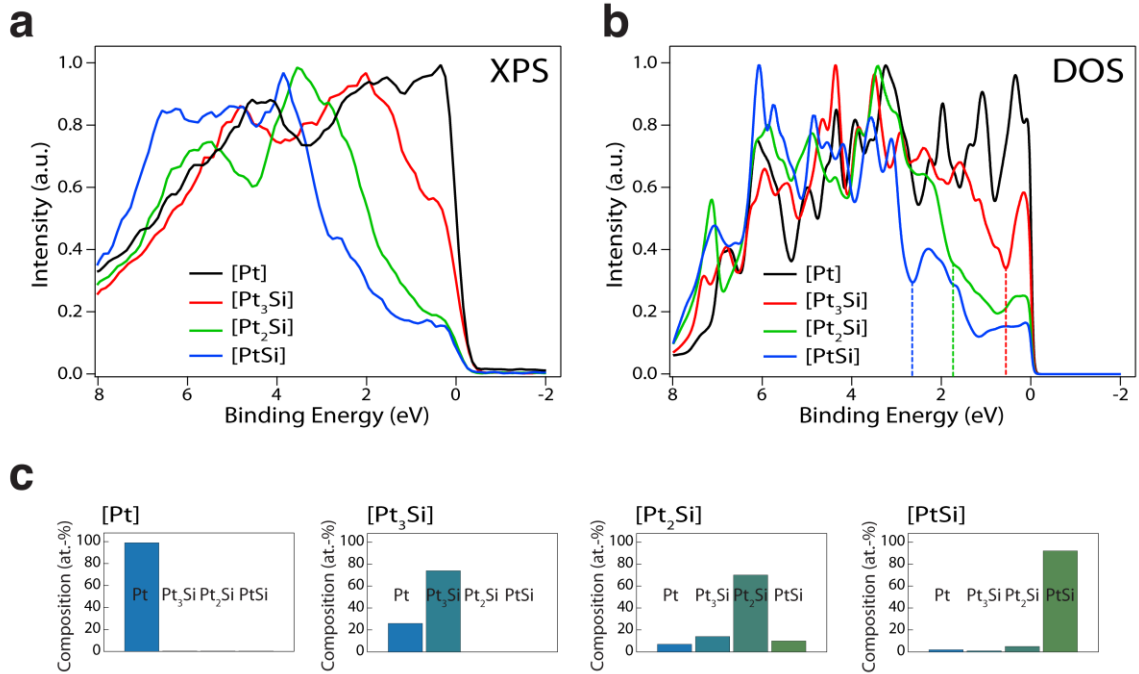


FIGURE 52: Experimental and theoretical Fermi edge shapes and compositions for [Pt], [Pt₃Si], [Pt₂Si], and [PtSi] samples. a. Experimental Fermi edge shapes of [Pt], [Pt₃Si], [Pt₂Si], and [PtSi] samples. Valence band electron population decreases with increasing Si-content of the silicide. b. Theoretical Fermi edge shapes of [Pt], [Pt₃Si], [Pt₂Si], and [PtSi] samples. Valence band electron population decreases with increasing Si-content of the silicide. The dotted vertical lines represent the location of the Pt_{5d} manifold for PtSi (2.7 eV below Fermi edge), Pt₂Si (1.8 eV below Fermi edge), and Pt₃Si (0.5 eV below Fermi edge). c. Thin film composition of [Pt], [Pt₃Si], [Pt₂Si], and [PtSi] samples as determined from quantitative XPS measurements.

Figure 53 shows a direct comparison of the experimental and theoretical DOS for [Pt], [Pt₃Si], [Pt₂Si], and [PtSi] films. Overall, we find that all experimental Pt_xSi valence band spectra capture not only the general shape but also several individual features of the theoretical Pt_xSi DOS very well (Figure 3b-d). However, Figure 53a shows that the experimental Pt valence band spectrum is unable to resemble the structural detail of the

theoretical Pt DOS. Comparison of our XPS with other XPS data show excellent agreement [49,52-54]; similarly comparison of our theoretical DOS and other DOS calculations show excellent agreement [54-55]; but there is some disagreement between the two for the case of Pt. This points towards an inherent difficulty in matching the valence band XPS spectrum of Pt to its theoretical DOS counterpart. The reasons for this phenomenon are discussed by Goldmann *et al.* [52] and Hofmann *et al.* [54]. The intensity and shape of XPS valence band spectra of open d shell metals, such as Pt, are modified and therefore unable to resemble DOS calculations, due to: 1) instrumental resolution of the XPS system, 2) matrix element modulation across the width of the d-band, 3) lifetime of the photohole, 4) interaction of the photohole with the conduction electrons, and 5) inelastic electron scattering. The factor that most prominently influences the structural detail of the valence band spectra is the lifetime of the photohole, which leads to a broadening of the XPS peaks. These effects are less pronounced in Pt_xSi due to the filling up of the d shell due to silicidation, in agreement with our results.

The measured and calculated valence bands for Pt and the Pt_xSi films are dominated by the Pt_{5d} manifold. The Pt_{5d} position within the valence band greatly influences the observed Fermi edge shapes and consequently the carrier densities. A maximum of the Pt_{5d} manifold is located directly at the Fermi edge in the case of Pt (Figure 53a), whereas it shifts further away from the Fermi edge for Pt_xSi with increasing Si content. Our calculations show that the Pt_{5d} manifold of PtSi is shifted to approximately 2.7 eV below the Fermi edge, whereas the Pt_{5d} manifold of Pt₂Si is only shifted to approximately 1.8 eV below the Fermi edge (see dotted vertical lines in Figure 52b), similar to previously reported values [50,51]. The novel Pt₃Si films show a shift of

the Pt_{5d} manifold of only approximately 0.5 eV, which results in a metallic-like character of the Fermi edge.

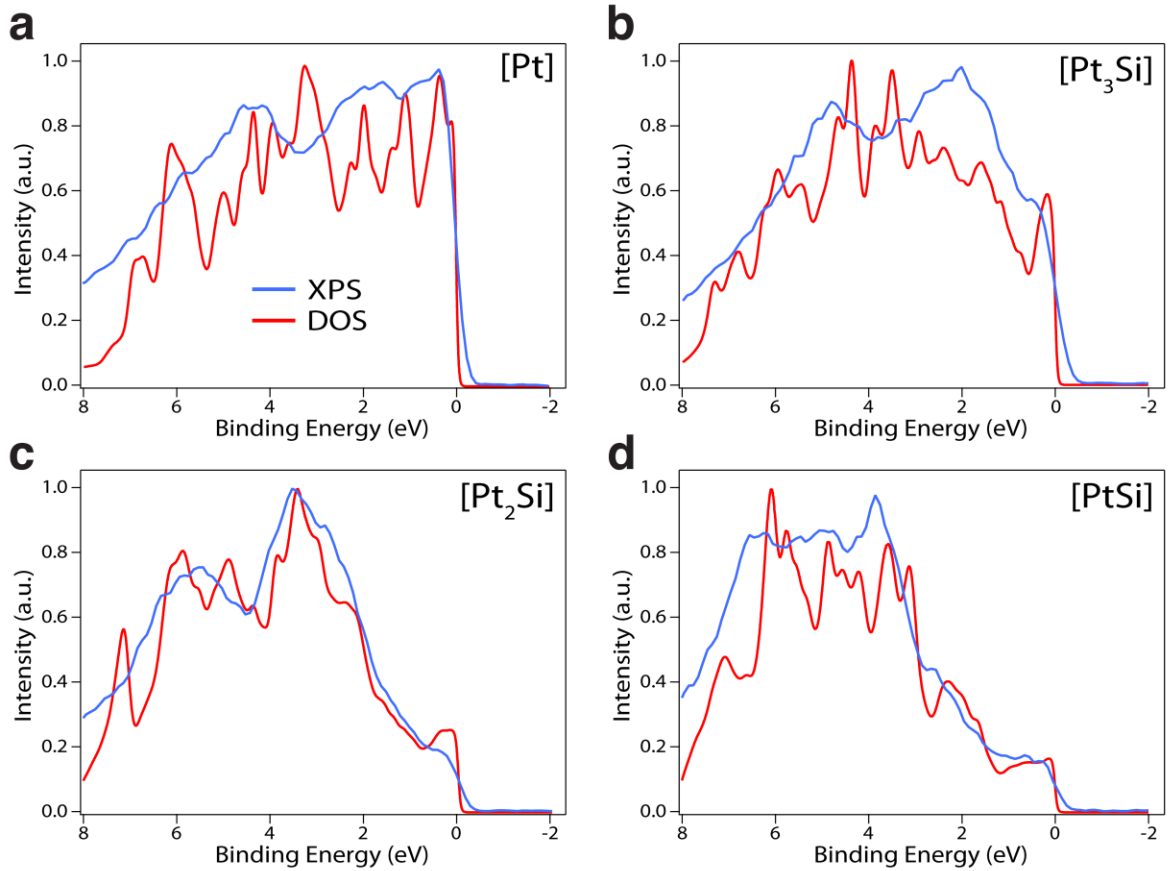


FIGURE 53: Comparison between experimental and theoretical Fermi edge shapes for [Pt], [Pt₃Si], [Pt₂Si], and [PtSi] samples. a. [Pt] sample (100% metallic Pt). b. [Pt₃Si] sample (which includes 74 % Pt₃Si). c. [Pt₂Si] sample (which includes 70% Pt₂Si). d. [PtSi] sample (which includes 92% PtSi).

Table 2 quantitatively compares the experimental and calculated DOS of Pt, Pt₃Si, Pt₂Si, and PtSi by means of their normalized carrier densities. The carrier densities were obtained by integrating the experimental and theoretical DOS within a

$2k_B T$ ($\sim 0.05\text{eV}$ for $T = 300\text{K}$) energy window around the Fermi edge [44]. The normalized carrier densities computed from the VB XPS measurements are in excellent agreement with the DOS calculations and confirm the systematic decrease in carrier density with increasing Si-content. The PtSi and Pt₂Si films were found to possess approximately 17-19% and 20-28% of the carrier density of Pt, respectively. These values are in good agreement with theoretical calculations performed by Bentmann *et al.* [50]. The Pt-rich Pt₃Si film possesses a very high carrier density of 59-61% of the DOS of Pt, which is a more than 3-fold improvement over the PtSi carrier density.

TABLE 2: Normalized carrier densities computed from VB XPS experiments and DOS calculations and measured sheet resistance values.

	Normalized Carrier Density		Sheet Resistance (Ω/\square)
	VB XPS	DOS Calculation	
<i>Pt</i>	1	1	2.6
<i>Pt₃Si</i>	0.59	0.61	18.9
<i>Pt₂Si</i>	0.20	0.28	31.8
<i>PtSi</i>	0.17	0.19	57.6

As mentioned above, a high DOS at the Fermi level is one of the requirements for having a high electrical conductivity. We performed four point probe measurements on the Pt, Pt₃Si, Pt₂Si, and PtSi films to determine the sheet resistance as an inverse measure of the electrical conductivity (Figure 54). The measured sheet resistance values show a systematic decrease in electrical conductivity from Pt to PtSi, which confirms the expected qualitative trend of the carrier density. The sheet resistance values for Pt,

Pt₃Si, Pt₂Si, and PtSi were measured as 2.6, 18.9, 31.8, and 57.6 Ω/□, respectively. The corresponding resistivity values were calculated as 10.6, 75.5, 127.2, and 230.4 μΩ-cm, respectively. The obtained sheet resistance and resistivity values for Pt, Pt₂Si and PtSi are in good agreement with results reported in other works [56,57].

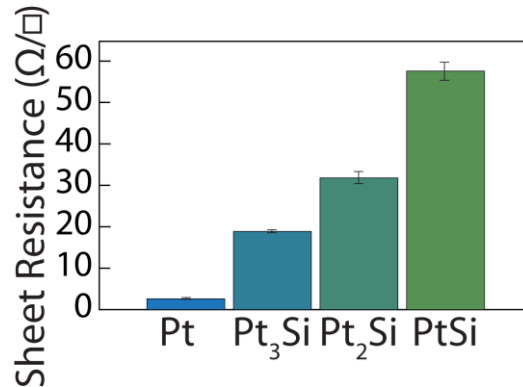


FIGURE 54: Sheet resistance of [Pt], [Pt₃Si], [Pt₂Si], and [PtSi] samples.

The high electrical conductivity (and correspondingly, the low sheet resistance and resistivity) of Pt₃Si compared to Pt₂Si and PtSi could motivate the use of Pt₃Si in several applications as a replacement for Pt₂Si or PtSi. Most notably for the semiconductor industry, where PtSi is considered as an attractive contact material to the source, drain, and gate for CMOS field effect transistors because of its low Schottky barrier and high thermal stability. However, PtSi suffers from low electrical conductivity due to its low DOS, which this work has verified. Recent work by Slepko and Demkov investigates Ti-doping of PtSi in an attempt to increase its DOS and thereby its electrical conductivity [44]. The researchers succeeded in increasing the DOS of PtSi by approximately 1.7 times through alloying with 12.5 at.% Ti. However, while the Ti doping

increased the DOS it also introduced Ti impurities that act as scattering centers and decrease the electrical conductivity. Here we were able to show that the Pt₃Si phase could solve these issues by inherently possessing a high DOS near the Fermi edge (approximately 3.4 times higher than DOS of PtSi) and a low sheet resistance and resistivity, thus indicating a high electrical conductivity. Since no doping is necessary to achieve this high DOS, Pt₃Si does not suffer from additional creation of scattering centers.

In summary, we show that the electronic structure and properties of Pt_xSi thin films can be tuned for specific applications between metallic and semimetallic properties by controlling the film stoichiometry. The comparison of valence band X-ray photoelectron spectroscopy spectra with theoretical density functional theory calculations shows that the density of states near the Fermi edge of Pt₃Si is significantly higher than that of Pt₂Si and PtSi. The resulting high electrical conductivity of Pt₃Si makes this stoichiometry particularly interesting for applications that demand high electrical conductivity combined with high thermal and mechanical stability [21]. This work on Pt_xSi provides a framework for studying the tunability of the electrical properties of other metal silicides based on Ni, Cu, Au, Fe, Co, Pd, Ag, and Rh among others. We expect that the open d shell metals (e.g. Fe, Co, Pd) will exhibit the strongest tunability of the electrical properties due to their similarity with Pt, which was shown to have a strong compositional dependence of the Pt_{5d} manifold position.

3.5 Preliminary results of single asperity cycling of platinum silicide contacts

Platinum silicide (Pt_xSi) AFM probes were fabricated in order to employ the atomic force microscopy (AFM) based test methodology presented in Section 2.3. The

goal of this study is to evaluate the performance of Pt_xSi as contact material in nanoelectromechanical (NEM) switches. AFM probes of the PtSi stoichiometry are commercially available through NANOSENSORS™ (NANOSENSORS™, Neuchatel, Switzerland). These probes are fabricated by removing the native oxide of a *sc*-Si AFM probe and subsequently coating the probe with a thin Pt film followed by annealing to facilitate the solid-state reaction between Pt and *sc*-Si similarly to the process shown in Figure 33. The usage of a large amount of *sc*-Si as silicon source for the silicidation reaction prevents other stoichiometries (*i.e.* Pt_2Si , Pt_3Si) from being formed in the fabrication method employed by NANOSENSORS. However, the properties of the Pt-rich stoichiometries Pt_2Si and especially Pt_3Si (*i.e.* metal-like conductivity, mechanical robust), as discussed earlier in Sections 3.2, 3.3 and 3.4, are more favorable for NEM-based applications. It is therefore desirable to fabricate AFM probes that possess Pt_2Si or Pt_3Si stoichiometries.

Pt-rich silicide-coated AFM probes were fabricated using commercial *sc*-Si AFM probes (PPP-FM Probes, NANOSENSORS™, Neuchatel, Switzerland) that were subsequently coated with *a*-Si and Pt thin films of specific thicknesses (see Section 2.1.2 for details on the coating process) based on the source-limited solid-state diffusion mechanism described in Section 3.3.3. The films thicknesses were 25 nm of *a*-Si and 40 nm of Pt so that a mixture of Pt_2Si and Pt_3Si can be obtained after the coated AFM probes are annealed for 10 min at 500°C in a rapid thermal annealing system (MILA-3000-P-N, ULVAC Technologies Inc., Kanagawa, Japan). Figure 55 shows a schematic of the employed Pt_xSi AFM probe fabrication process. It is important to note that *sc*-Si AFM probes are covered with a native oxide layer that prevents any reaction between the Pt/*a*-Si diffusion couple and the *sc*-Si substrate and thereby accurately allows for the

employment of the source-limited solid-state diffusion method. A *sc*-Si wafer witness sample was placed next to the AFM probes in the sputtering chamber and later subjected to a similar annealing treatment. This allows for the subsequent quantitative X-ray photoelectron spectroscopic (XPS) characterization and provides an estimate of the Pt_xSi stoichiometry of the AFM probes.

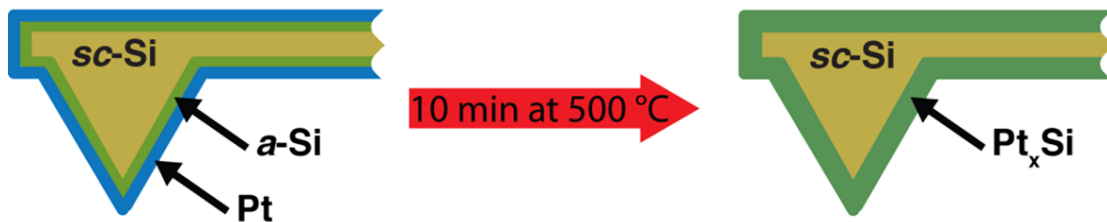


FIGURE 55: Schematic of the Pt_xSi AFM probe fabrication process. A commercial *sc*-Si AFM probe is sequentially coated with thin films of *a*-Si and Pt. Pt_xSi is later formed through a rapid thermal annealing treatment at 500°C for 10 minutes.

Another important feature of the commercial *sc*-Si AFM probes that has to be considered is their oxide-sharpened tip apex. NANOSENSORS™ employs an oxide-sharpening process to reduce the radius of the AFM probe tip by growing a sharp oxide “spike” out of the original *sc*-Si probe tip. Figure 56a shows a transmission electron microscopy image of an as-received, oxide-sharpened AFM probe. The goal of the oxide-sharpening process is to achieve better lateral resolution when performing a contact-mode AFM scan. However, this high aspect ratio oxide tip has negative implications if the AFM probe is coated as done here, as the oxide is very brittle, not uniformly dense and often extremely irregularly shaped. Pt_xSi AFM probes that are

fabricated directly from the as-received *sc*-Si AFM probe without the removal of the oxide tip, are prone to fracture of the oxide tip, and thereby of the Pt_xSi coating, in the contact area if employed in the AFM cycling test procedure. This motivates the complete removal of the oxide tip prior to the coating of the AFM probe with *a*-Si/Pt.

Figure 56 illustrates the used Pt_xSi AFM probe production process, accompanied by transmission electron spectroscopy and electron diffraction images. Controlled wearing/shaping of the as-deposited AFM probes was utilized to completely remove the oxide tip before *a*-Si/Pt deposition. Contact mode scans ($2\ \mu\text{m} \times 2\ \mu\text{m}$, 512×512 , 3 Hz) of the oxide-sharpened AFM probes under 80 nN normal load (note: same load as used in the AFM cycling tests) successfully removed the oxide tip when performed on diamond-like carbon (DLC) and ultrananocrystalline diamond (UNCD) substrates. The substrate influenced the final probe geometry significantly: The extremely flat (RMS < 1 nm) and mechanically robust ($E > 200\ \text{GPa}$, $H > 40\ \text{GPa}$) DLC substrate led to a complete flattening of the probe, similarly to a flat punch (top row TEM image in Figure 56b), whereas the more rough (RMS $\approx 15\ \text{nm}$) and mechanically robust ($E > 900\ \text{GPa}$, $H > 90\ \text{GPa}$) UNCD substrate produced more rounded probe tips (see bottom TEM image in Figure 56b). However, the *a*-Si and Pt coatings on both probe geometries were very conformal as shown in the overlay images of Figure 56c. The representative electron diffraction spectra of an *a*-Si/Pt coated probe is composed of diffraction rings typical for Pt (Figure 56c, note: *a*-Si will not contribute any diffractions rings due to its amorphous structure). Upon annealing, the overall probe geometry remains constant whereas Pt_xSi diffraction spots appear in the electron diffraction images – predominantly of the Pt_3Si phase. It can therefore be concluded that the presented fabrication process led to

predominantly Pt_3Si -containing Pt_xSi AFM probes (note: the exact composition of the AFM probe will be deduced from the XPS measurements of the witness samples).

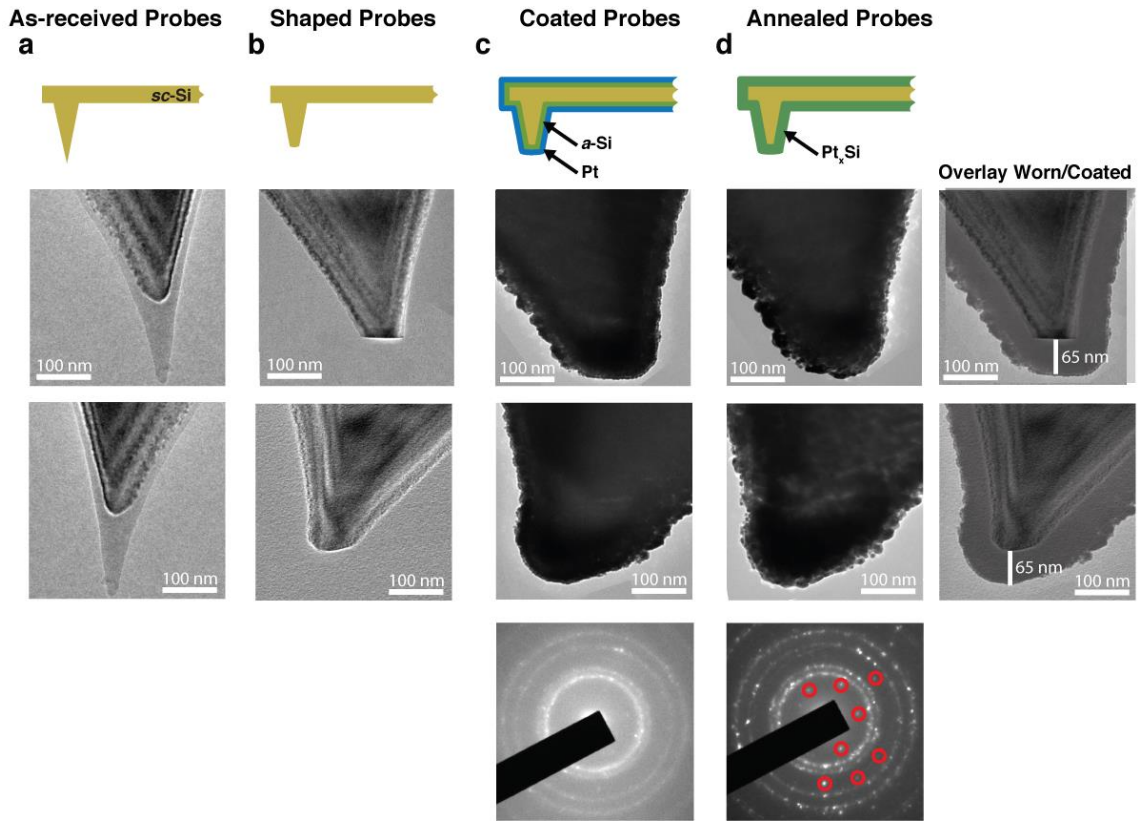


FIGURE 56: Fabrication process of Pt_xSi probes including electron micrographs and electron diffraction images. a) As-received *sc*-Si AFM probes possess an oxide-sharpened end. b) Contact AFM scans used to physically remove the silicon oxide and create a reproducible tip geometry. c) Sequential coating of the front- and backside of the AFM probe with *a*-Si and Pt. Electron beam diffraction image shows diffraction pattern typical of Pt. d) Annealing of coated AFM probes creates Pt_xSi . Electron beam diffraction image shows Pt_xSi diffraction spots appearing (marked with red circles).

AFM lifetime cycling tests as described in Section 2.3 were performed in order to compare the performance of the fabricated Pt_xSi AFM probes to those of Pt AFM probes

(Pt AFM cycling data shown in Figure 25). Figure 57 demonstrates that the Pt coated AFM probe experiences an increase in contact resistance of more than 3 orders of magnitude when cycled against a flat Pt counter surface. The fabricated Pt_xSi-coated AFM probe in contrast largely maintains its initial contact resistance throughout 10⁷ contacting cycles (increase in contact resistance smaller than 1 order of magnitude). These preliminary switching results, which show a stable contact resistance throughout 10⁷ contacting cycles are extremely promising for Pt_xSi's application as contact material in NEM switches. It can be concluded that silicidation suppresses the tribopolymer formation observed in Pt-Pt contacts (see Figure 21) and therefore leads to a stable contact resistance.

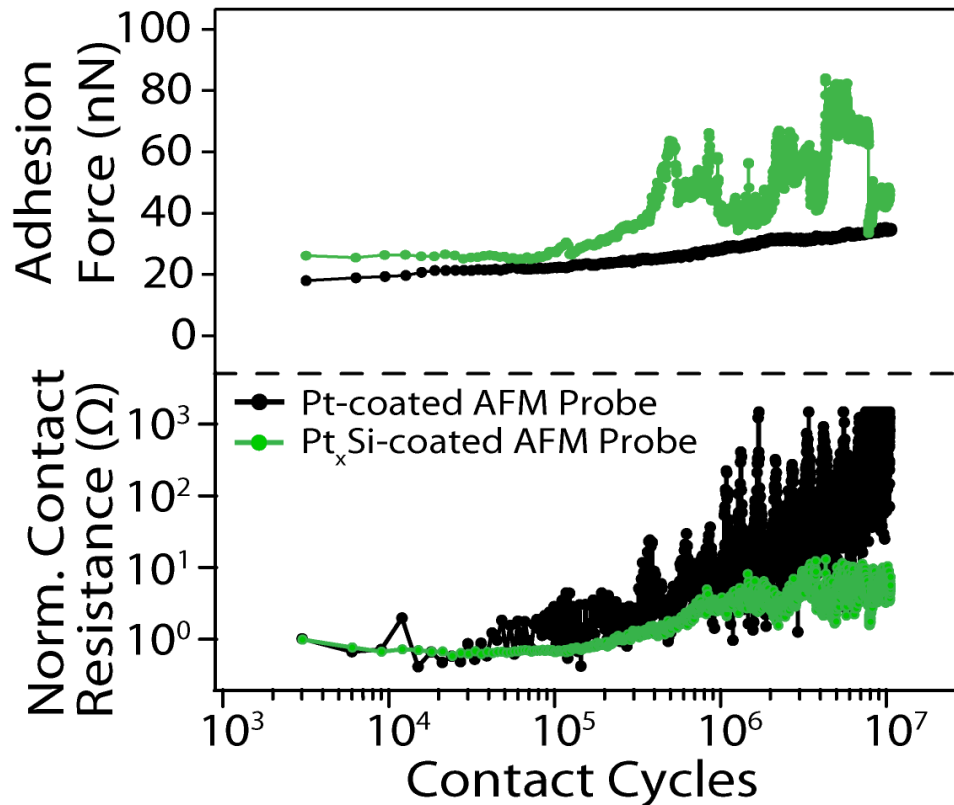
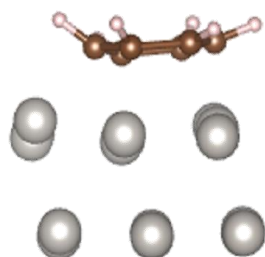


FIGURE 57: Atomic force microscopy lifetime tests of Pt-Pt and Pt_xSi-Pt nanocontacts. Pt_xSi-coated AFM probes exhibit constant contact resistance of 10⁷ cycles, whereas Pt-coated AFM probes exhibit a 3 order of magnitude increase in contact resistance. The adhesion force of the Pt_xSi-coated AFM probe becomes unstable after 3·10⁵ cycles.

Density functional theory (DFT) calculations⁵ can help identify the origins of tribopolymer formation when cycling Pt AFM probes and missing tribopolymer formation in Pt_xSi AFM probes. DFT calculations studying the interaction of benzene (C₆H₆) as a model hydrocarbon contaminant with Pt and PtSi surfaces are shown in Figure 58. Benzene strongly adsorbs onto the Pt surface as evidenced by the distortion of the benzene molecule from its equilibrium planar shape. The adsorption energy of benzene on a Pt surface is 0.9-1.9 eV, depending on the exact location on the surface. This high adsorption energy is originated in the catalytic activity of Pt and its affinity for

hydrocarbon-containing species. The benzene is essentially anchored onto the Pt surface. If a second Pt surface (also covered with benzene) would approach and impact a benzene-covered Pt surface, as it is the case in our Pt-Pt cycling experiments and in real NEM switches, then the anchored benzene molecules would interact with each other. Rappe *et al.* recently showed that in such a case the benzene molecules would partake in a polymerization reaction, driven by the high contact pressures, and eventually form polymer-like materials [58]. Rappe *et al.* showed that a dehydrogenation reaction takes place at about 27 GPa normal stress that eventually enables the formation of C-C bonds between different benzene rings [58]. The reaction product of repeated interactions of benzene-covered Pt surfaces is found to be a polymer-like structure – similar to the tribopolymer observed in Figure 21. It is important to note that the observed polymerization reactions would be impossible without the anchoring of the benzene molecules, which enable direct benzene-benzene interactions to take place.

Benzene Adsorption on Pt



Benzene Adsorption on PtSi

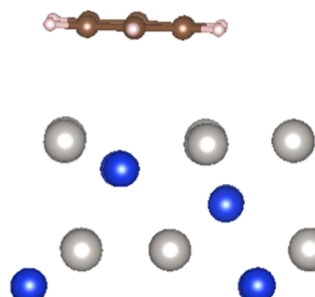


FIGURE 58: Density functional theory (DFT) calculations of the interaction of benzene (C_6H_6) with Pt and PtSi surfaces.⁵ Side view of the simulation box showing the strong adsorption of benzene on Pt and weaker adsorption of benzene on PtSi surfaces.

⁵ The density functional theory calculations presented here were performed by Y. Qi and J. Yang under the supervision of A. M. Rappe (Department of Chemistry, University of Pennsylvania).

In contrast, the PtSi surface only weakly adsorbs the benzene (adsorption energy = 0.07-0.5 eV). This can be seen in Figure 58 by the large PtSi-benzene separation as well as the planar equilibrium structure of the benzene molecule. If the PtSi-benzene system is contacted with a benzene-covered counter surface (such as benzene-covered Pt as it is the case in our experiments), the weakly-bound benzene will easily slide along the PtSi surface and out of the contacting area under an applied pressure. This process will inhibit any benzene-benzene interactions and thereby inhibit tribopolymer formation.

In summary, the filling up of the d-shell of Pt due to silicidation leads to a reduction in the catalytic activity and affinity to hydrocarbons, which reduces the adsorption energy of hydrocarbons up to one order of magnitude. The reduced adsorption energy of hydrocarbons on Pt_xSi surfaces leads to reduced hydrocarbon polymerization during mechanical loading and thereby to decreased tribopolymer formation. The reaction scheme found through DFT calculations explains the improved contact resistance stability of Pt_xSi during nanocontact cycling experiments in contrast to Pt contacts, which are prone to tribopolymer build-up.

BIBLIOGRAPHY CHAPTER 3

- [1] Ma, Q., Rao, V. *Reliability, Packaging, Testing and Characterization of MEMS/MOEMS VI – Proc. SPIE*. **2007**, 6463, 646305.
- [2] Crider, C. A.; Poate, J. M.; Rowe, J. E.; Sheng, T. T. *J. Appl. Phys.* **1981**, 52, 2860.
- [3] Bhaskaran, H.; Sebastian, A. *IEEE T. Nanotechnol.* **2009**, 8, 128.
- [4] Hung, L. W.; Nguyen, C. T. C.; PROC IEEE MICR ELECT, Wanchai, Hong Kong, China (January, 2010).
- [5] Stark, T.; Gruenleitner, H.; Hundhausen, M.; Ley, L.; *Thin Solid Films*. **2000**, 358, 79.
- [6] Wittmer, M. *J. Appl. Phys.* **1983**, 54, 5081.
- [7] Loh, O. Y.; Espinosa, H. D. *Nat. Nanotechnol.* **2012**, 7, 283-295.
- [8] Sinha, N.; Wabiszewski, G. E.; Mahameed, R.; Felmetsger, V. V.; Tanner, S. M.; Carpick, R. W.; Piazza, G. *Appl. Phys. Lett.* **2009**, 95, 053106.
- [9] Ito, T.; Fujimura, N.; Nakayama, Y. *Thin Solid Films*. **1988**, 167, 187.
- [10] Mangolini, F.; Ahlund, J.; Wabiszewski, G. E.; Adiga, V. P.; Egberts, P.; Streller, F.; Backlund, K.; Karlsson, P. G.; Wannberg, B.; Carpick, R. W. *Rev. Sci. Instrum.* **2012**, 83, 093112.
- [11] Mangolini, F.; Rossi, A.; Spencer, N. D. *J. Phys. Chem. C* **2011**, 115, 1339-1354.
- [12] Miglio, L.; d'Heurle, F. *Silicides - Fundamentals and Applications*; World Scientific Publishing: Singapore, 2000.
- [13] Peter, A. P.; Meersschaut, J.; Richard, O.; Moussa, A.; Steenbergen, J.; Schaekers, M.; Tokei, Z.; Van Elshocht, S.; Adelman, C. *Chem. Mater.* **2015**, 27, 245-254.
- [14] Tu, K. N.; Thompson, R. D.; Tsaur, B. Y. *Applied Physics Letters* **1981**, 38, 626-628.
- [15] Rhoderick, E. H.; Williams, R. H. *Metal-Semiconductor Contacts*, Clarendon Press: Oxford, 1988.
- [16] Chen, L. J. *JOM* **2005**, 57, 24-31.
- [17] Rowe, D. M. *Thermoelectrics Handbook: Macro to Nano*, Taylor & Francis Group: Abingdon, 2006.
- [18] Fedorov, M. I. *J. Thermoelectr.* **2009**, 2, 51-60.

- [19] Itoh, T.; Yamada, M. *J. Electron. Mater.* **2009**, *38*, 925-929.
- [20] de Boor, J.; Dasgupta, T.; Kolb, H.; Compere, C.; Kelm, K.; Mueller, E. *Acta Mater.* **2014**, *77*, 68-75.
- [21] Streller, F.; Wabiszewski, G. W.; Mangolini, F.; Feng, G.; Carpick, R. W. *Adv. Mater. Interfaces* **2014**, *1*, 1300120.
- [22] Streller, F.; Wabiszewski, G. E.; Carpick, R. W. *IEEE Nanotechnol. Mag.*, DOI: 10.11109/MNANO.2014.2373451.
- [23] Naik, G. V.; Shalaev, V. M.; Boltasseva, A. *Adv. Mater.* **2013**, *25*, 3264-3294.
- [24] Liu, C; Li, F.; Ma, L.-P.; Cheng, H.-M. *Adv. Mater.* **2010**, *22*, E28-E62.
- [25] Lin, H.-K.; Cheng, H.-A; Lee, C.-Y.; Chiu, H.-T. *Chem. Mater.* **2009**, *21*, 5388-5396.
- [26] Li, H.; Wu, J.; Wang, Z. M. *Silicon-based Nanomaterials*, Springer: Berlin, 2013.
- [27] Higgins, J. M.; Ding, R.; Jin, S. *Chem. Mater.* **2011**, *23*, 3848-3853.
- [28] Schmitt, A. L.; Higgins, J. M.; Szczech, J. R.; Jin, S. J. *Mater. Chem.* **2010**, *20*, 223-235.
- [29] Chou, Y.-C.; Wu, W.-W.; Cheng, S.-L.; Yoo, B.-Y.; Myung, N.; Chen, L. J.; Tu, K. N. *Nano Lett.* **2008**, *8*, 2194-2199.
- [30] Liu, X. H.; Wang, J. W.; Huang, S.; Fan, F.; Huang, X.; Liu, Y.; Krylyk, S.; Yoo, J.; Dayeh, S. A.; Davydov, A. V.; Mao, S. C.; Picraux, T.; Zhang, S.; Li, J.; Zhy, T.; Huang, J. Y. *Nat. Nanotechnol.* **2012**, *7*, 749-756.
- [31] Lin, Y.-C.; Chen, Y.; Xu, D.; Huang, Y. *Nano Lett.* **2010**, *10*, 4721-4726.
- [32] Stach, E. A.; Pauzauskie, P. J.; Kuykendall, T.; Goldberger, J.; He, R.; Yang, P. *Nano Lett.* **2003**, *3*, 867-869.
- [33] Nukala, P.; Agarwal, R.; Qian, X.; Jang, M. H.; Dhara, S.; Kumar, K.; Johnson, A. T. C.; Li, J.; Agarwal, R. *Nano Lett.* **2014**, *14*, 2201-2209.
- [34] Tanuma, S. *Surface Analysis by Auger and X-Ray Photoelectron Spectroscopy*, IM Publications: Charlton, 2003.
- [35] Poate, J. M.; Tisone, T. C. Kinetics and mechanism of platinum silicide formation on silicon. *Appl. Phys. Lett.* **1974**, *24*, 391-393.
- [36] Kobayashi, T.; Koguchi, M.; Iijima, S.; Ohkura, M.; Wada, Y. Nucleation of in-situ phosphorus-doped amorphous-silicon films deposited by pyrolysis of Si₂H₆ and PH₃. *J. Electrochem. Soc.* **1994**, *141*, 1365-1369.
- [37] Coffa, S.; Poate, J. M.; Jacobson, D. C. Determination of diffusion mechanisms in amorphous silicon. *Phys. Rev. B* **1992**, *45*, 8355-8358.

- [38] Lerch, W.; Stolwijk, N. A.; Mehrer, H.; Poisson, C. Diffusion of Platinum into Dislocated and Non-Dislocated Silicon. *Semicond. Sci. Technol.* **1995**, *10*, 1257-1263.
- [39] Walser, R. M.; Bené, R. W. First phase nucleation in silicon-transitionmetal planar interfaces. *Appl. Phys. Lett.* **1976**, *28*, 624-625.
- [40] Tichelaar, F. D.; Schapink, F. W. Structure of twin boundaries in L₁₂ ordered alloys. *Philos. Mag. A* **1986**, *54*, 55-60.
- [41] Tichelaar, F. D.; Schapink, F. W. TEM determination of incoherent twin-boundary structure in L₁₂ ordered alloys. *J. Phys. Colloq.* **1988**, *49*, 293-298.
- [42] Janowski, G. M.; Stafford, G. R. The microstructure of electrodeposited titanium-aluminum alloys. *Metall. Trans. A* **1992**, *23*, 2715-2723.
- [43] Chou, T. C.; Chou, Y. T. Volume and grain boundary diffusion in L₁₂ alloys with special reference to Ni₃Al compounds. *MRS Proceedings* **1984**, *39*, 461-474.
- [44] Slepko, A.; Demkov, A. A. *Phys. Rev. B* **2012**, *85*, 035311.
- [45] Streller, F.; Agarwal, R.; Mangolini, F.; Carpick, R. W. *Chem. Mater.* **2015**, *27*, 4147-4253.
- [46] Streller, F.; Wabiszewski, G. E.; Durham, D. B.; Yang, F.; Yang, J.; Qi, Y.; Srolovitz, D. J.; Rappe, A. M.; Carpick, R. W. Proceedings of the IEEE 61st Holm Conference on Electrical Contacts, San Diego, CA, **2015**, 363-369. doi: 10.1109/HOLM.2015.7355122
- [47] Streller, F.; Wabiszewski, G. E.; Carpick, R. W. Proceedings of the 14th International Conference on Nanotechnology, Toronto, ON, **2014**, 141-145. doi: 10.1109/NANO.2014.6967966
- [48] Bubnova, O.; Khan, Z. U.; Wang, H.; Braun, S.; Evans, D. R.; Fabretto, F.; Hojati-Talemi, P.; Dagnelund, D.; Arlin, J.-P.; Geerts, Y. H. *et al. Nat. Mater.* **2014**, *13*, 190-194.
- [49] Fryer, R. T.; Lad, R. J. *J. Alloy Compd.* **2016**, *682*, 216-224.
- [50] Bentmann, H.; Demkov, A. A.; Gregory, R.; Zollner, S. *Phys. Rev. B* **2008**, *78*, 205302.
- [51] Franco, N.; Klepeis, J. E.; Bostedt, C.; Van Buuren, T.; Heske, C.; Pankratov, O.; Terminello, L. J. *J. Electron Spectrosc. Relat. Phenom.* **2001**, *114-116*, 1191-1196.
- [52] Hoehst, H.; Huefner, S.; Goldmann, A. *Phys. Lett.* **1976**, *57A*, 265-266.
- [53] Strasser, P.; Koh, S.; Anniyev, T.; Greeley, J.; More, K.; Yu, C.; Liu, Z.; Kaya, S.; Nordlund, D.; Ogasawara, H.; Toney, M. F.; Nilsson, A. *Nat. Chem.* **2010**, *2*, 454-460

- [54] Hofmann, T.; Yu, T. H.; Folse, M.; Weinhardt, L.; Baer, M.; Zhang, Y.; Merinov, B. V.; Myers, D. J.; Goddard III, W. A.; Heske, C. *J. Phys. Chem. C* **2012**, *116*, 24016–24026.
- [55] Krupski, K.; Moors, M.; Jozwik, P.; Kobiela, T.; Krupski, A. *Materials* **2015**, *8*, 2935–2952.
- [56] Powell, R. W.; Tye, R. P.; Woodman, M. J. *Platinum Met. Rev.* **1962**, *6*, 138-143.
- [57] Conforto, E. *Formation and properties of nanometer-thick platinum silicide layers*. PhD. Thesis, Ecole Polytechnique Federale Du Lausanne, 1996.
- [58] Qi, Y.; Yang, J; Rappe, A. M. *ACS Appl. Mater. Interfaces* **2016**, *8*, 7529-7535.

CHAPTER 4: CHEMICAL AND STRUCTURAL CHARACTERIZATION OF TRIBOPOLYMERS

Chapters 2 and 3 showed that tribopolymer formation constitutes the Achilles' heel of nanoelectromechanical switches, drastically limiting their lifetime and thus preventing successful commercialization. In order to systematically design materials that are immune to tribopolymer formation, exact knowledge of the chemistry and structure of the formed species is desirable. The amount of tribopolymer formed during the atomic force microscopy cycling tests presented in chapter 2 is insufficient (see Figure 21) to perform spectroscopic studies, which motivates the formation of larger quantities of tribopolymer and subsequent chemical and structural analysis [1]. This chapter will present a macrotribometer-based method to produce a quantity of tribopolymer that allows for spectroscopic analysis.

4.1 Experimental setup to produce tribopolymer

A custom-build macrotribometer⁶ [2,3] located at the Materials Tribology Laboratory at the University of Delaware was utilized to form tribopolymer in Pt-Pt contacts. This experiment was inspired by work from Hermance & Egan [4], who studied tribopolymer (Hermance & Egan call it “mysterious brown deposit”) formation in different sliding material pairs. Hermance & Egan found that Pt-Pt contacts are extremely prone to the build-up of tribopolymers – similar to observations in this thesis. Here, we coated 3.175 mm diameter steel balls and steel shim stock with 1.4 μm of platinum. The Pt-

⁶ The macrotribology experiment presented in this chapter was performed on equipment in Prof. David Burris Group at the University of Delaware.

coated balls were then repeatedly slid (1.5 mm stroke length, 5.3 Hz frequency) over the Pt-coated shim stock in a ball on flat configuration under 80 mN load. This load corresponds to a Hertz pressure of 390 MPa and a contact diameter of 20 μm . Figure 59a shows a schematic and picture of the experimental setup. The whole experiment was conducted in a custom-build environmental chamber containing a 1000 ppm benzene/air mixture (Matheson Gas, Basking Ridge, NJ). Benzene was used as a model hydrocarbon gas, similar to Hermance & Egan's work [4], experiments conducted by De Boer *et al.* [5-7], and molecular dynamics simulations conducted by Rappe *et al.* [8]. A total of 10^5 sliding cycles were performed and the friction coefficient as well as normal load were recorded throughout the experiment. The recorded friction coefficient serves as a useful indicator of the contact material pairing: $\mu \approx 0.8$ was seen for Pt-steel and steel-steel contacts, $\mu \approx 0.4$ - 0.5 was typical for Pt-Pt contacts, and $\mu \approx 0.3$ - 0.4 for Pt-Pt contacts under the benzene-containing atmosphere. The plot of the friction coefficient as function of sliding time shown in Figure 59b illustrates that a Pt-Pt contact was present throughout the duration of the six-hour experiment. The friction coefficient remained fairly constant throughout the whole experiment, except around 0.7 and 1.2 hrs when slight normal force instabilities occurred.

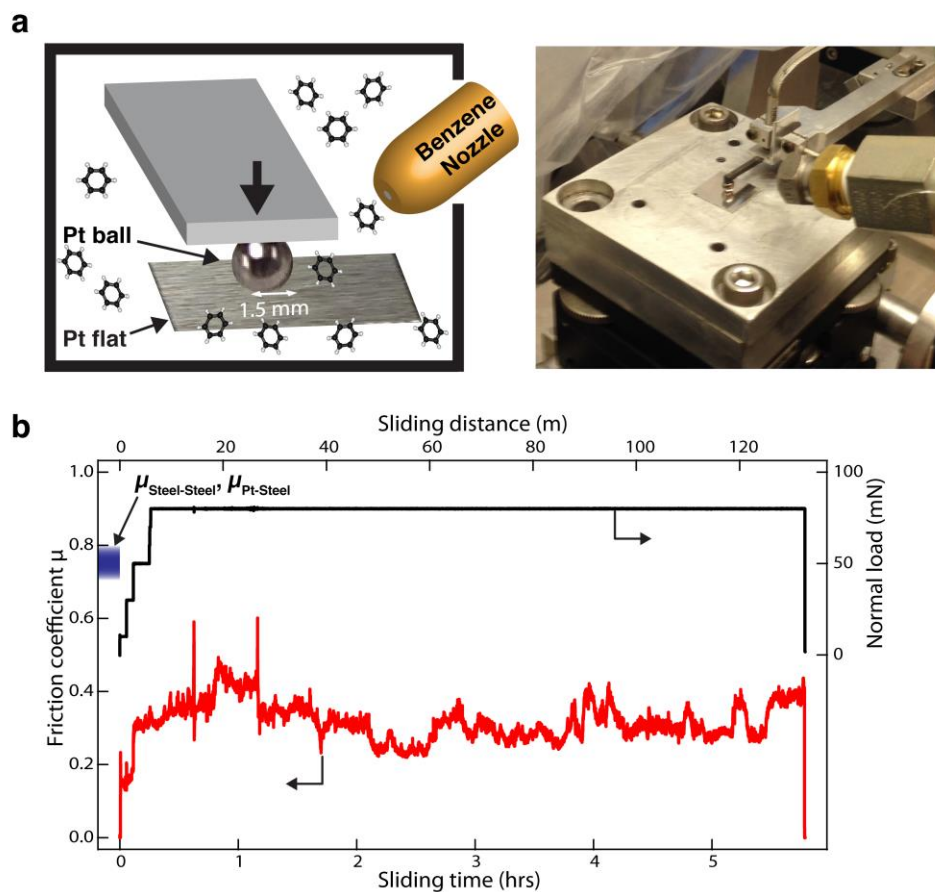


FIGURE 59: Experimental setup and results of the macrotribometer experiment to form tribopolymer. a) Schematic and picture of the experimental setup. A Pt-coated steel ball is slid against a Pt-coated shim stock under a benzene-containing atmosphere. b) Friction coefficient and normal load as a function of sliding time and sliding distance. The friction coefficient stayed below 0.6, indicating Pt-Pt contact throughout the experiment.

Figure 60a and b show optical images of the wear track and of an unworn area of the Pt-coated shim stock, respectively. On first glance, it can be clearly seen that the sliding experiment led to wear track formation and deposition of debris around the wear track. The two red stars in Figure 60a mark the turning points of the sliding ball and the area between them constitutes the actual wear track. Several types of debris with

distinct appearances were formed in and around the wear track. After careful inspection of the wear track and its surrounding area, three main types of debris can be categorized. Type ① is roundish, black-appearing debris distributed randomly but at approximately equal distances of 150 μm from the wear track. Type ② is patchy, brown-appearing debris located about 100 μm on either side of the wear track. Type ③ is flaky, metallic/black-appearing debris mostly located around the turnaround points. Figure 60c shows two cross-sectional topography measurements of the wear track conducted with a Zygo New View 3100 white light interferometer (Zygo Corporation, Middlefield, CT, United States). The green cross-section is representative of the majority of the wear track and shows a 0.93 μm deep groove of 17 μm diameter (close to the theoretical contact diameter value of 20 μm). The blue cross-section is taken from a 100 μm long area of the wear track, where the Pt coating was removed during the sliding. The missing Pt is illustrated by the different color in the optical image and a groove of similar depth then the Pt-coating thickness of 1.4 μm (see blue cross-section in Figure 60c). The depth of the cross-sections throughout the wear track suggest that Pt was partially worn away from the wear track. This is also evident by many patchy areas inside the wear track where Pt has been partially removed. The removed Pt “flakes” can be expected to be part of debris type ③ around the inflection points, due to its metallic appearance.

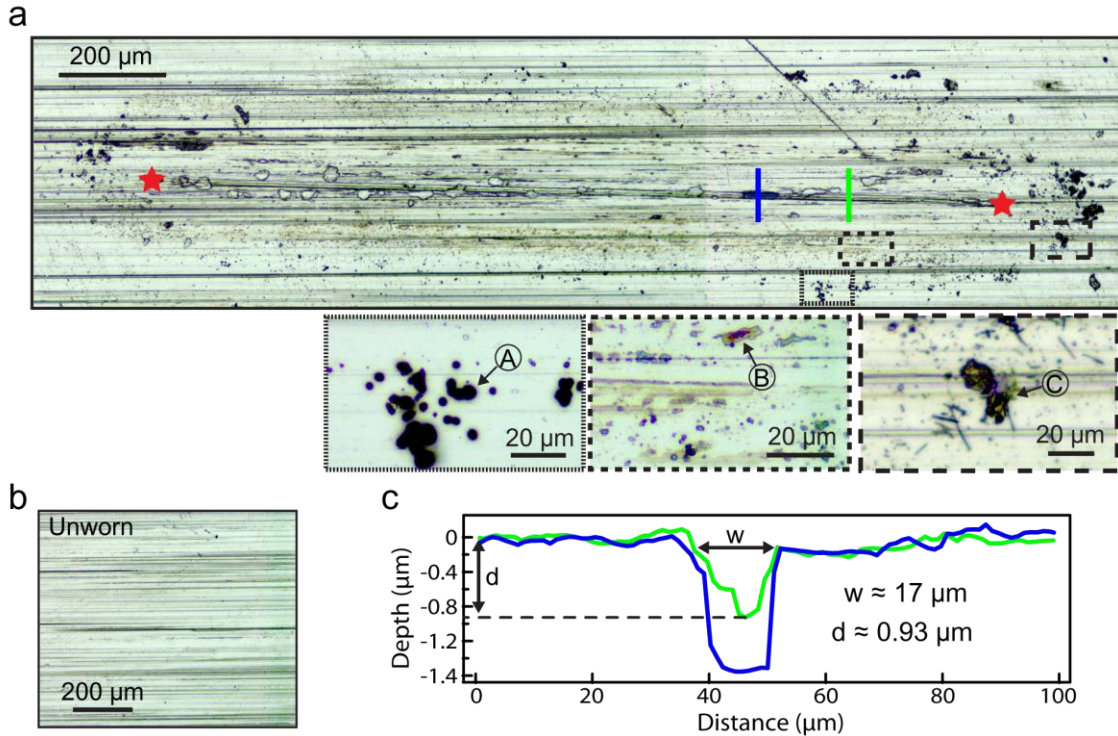


FIGURE 60: Optical images and profilometry of the wear track. a) Optical image of the whole wear track with three zoom-in regions (labeled **A**, **B**, **C**) indicating the different types of tribopolymer formed. b) Optical image of the unworn Pt-coated sheet stock. c) Cross-sectional measurement of the wear track topography using a scanning white light interferometer. The locations of the two cross-sections are indicated in a).

4.2 Spectroscopic characterization of tribopolymers

Figure 61a presents scanning electron microscopy (SEM) and energy-dispersive X-ray spectroscopy (EDX) images of the three debris types **A**, **B** and **C**. A clear correlation between the debris locations and a strong carbon signal can be seen, indicating the carbonaceous nature of the tribopolymer. Especially debris type **A** possesses a very intense carbon signal and its shape is precisely mirrored in the EDX carbon map. The carbon signal of debris **B** is less intense than that of debris **A**, but

also correlated to its location. Debris © is only partially composed of carbon as the big flake not visible in the EDX carbon map is composed of Pt. This is in line with the partially metallic appearance of debris © in the optical images. Figure 61b shows the platinum, carbon and oxygen signals of an EDX line scan across debris type ©. The location of the line scan is illustrated by the dotted line. It can be seen that all three elemental signals are sensitive to the debris. The platinum signal decreases and both the carbon and oxygen signal increase across debris type ©. The carbon signal experiences a six-fold increase in signal, whereas the oxygen signal increases only minimally. This shows that the tribopolymer type © is mainly composed of carbon. The fact that Pt is still detected at the debris is due to the large information depth of up to 3 µm in EDX. Since the height of the different debris types does not exceed 1.5 µm, a nearly constant signal from the Pt-coating is measured in EDX.

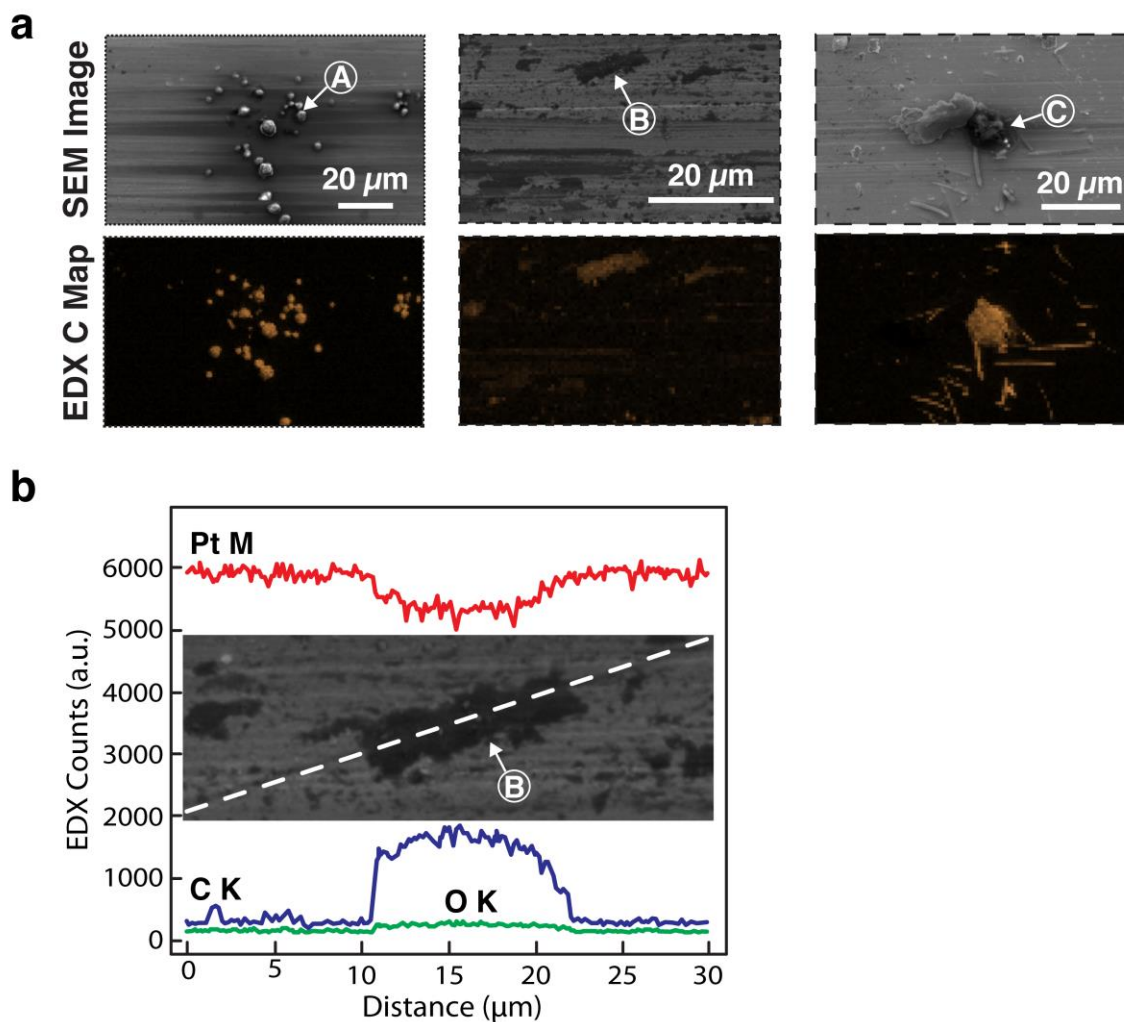


FIGURE 61: Energy-dispersive X-ray spectroscopy (EDX) measurements of the three identified tribopolymer kinds. a) EDX map of the carbon concentration. b) EDX line scan of carbon, oxygen and platinum concentrations in tribopolymer type \textcircled{B} . The location of the cross-section is illustrated by the dotted line.

The different tribopolymers were subject to infrared (IR) spectroscopic analysis. IR spectroscopy is a common tool to analyze polymeric substances and identify their backbone and functional groups. An IR spectrum is formed due to the absorption of electromagnetic radiation at frequencies that correlate to the vibration of specific

chemical bonds inside a molecule [9]. Here, we used an Anasys nanoIR2™ system (Anasys Instruments, Santa Barbara, CA) that allows for IR absorption spectroscopy with nanometer scale resolution. Figure 62 shows a schematic of the nanoIR2™ technique. The sample of interest is illuminated with pulses of IR radiation during the measurement. Heat is created in the sample that causes a rapid thermal expansion of the sample absorbs the IR radiation. This thermal expansion is precisely detected by an AFM probe that is in contact with the sample. Rapid thermal expansions excite resonant oscillations in the AFM cantilever, whose amplitude is directly proportional to the absorption coefficient of the sample [10]. An IR absorption spectra is then produced by recording oscillation amplitude of the AFM cantilever as a function of IR wavelength. Just like regular IR spectroscopy, nanoIR2™ can detect the chemical nature of the sample by relating each absorption peak to a specific excitation of a molecular resonance. These fundamental absorption frequencies are they key to determining the structure-spectral relationships [9]. Here, our goal is to identify if the tribopolymer really possesses polymer-like absorption spectra and then to differentiate the three tribopolymers according to their saturation and functional groups.

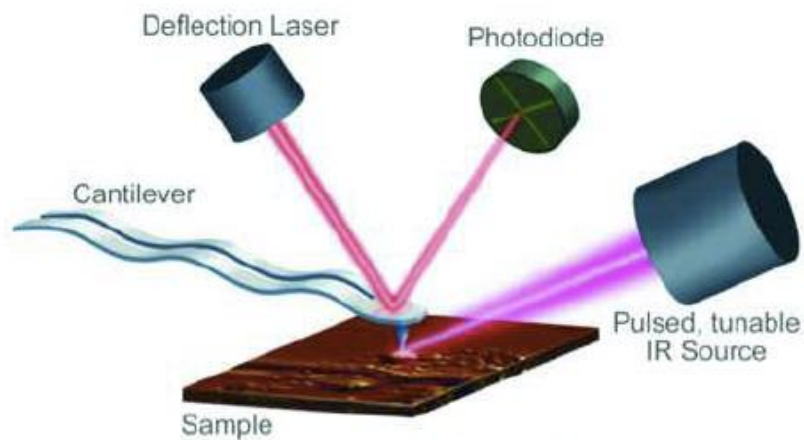


FIGURE 62: Schematic of the Anasys nanoIR2™ working principle. The sample is illuminated with pulses of IR radiation and an AFM probe is utilized to detect the absorbed radiation with nanoscale spatial resolution. [10]

Figure 63 shows nanoIR spectra of the unworn Pt-coated shim stock (subjected to the benzene-containing atmosphere) and the three identified tribopolymer types. The discontinuity in the absorption signal between wavenumbers 2200 cm^{-1} and 2300 cm^{-1} is due to a required change in excitation laser. The two different lasers also possess different noise levels, as evident when comparing the low wavenumber data with the high wavenumber data. However, distinct differences between the three debris types and the unworn reference area were noticeable. A book chapter by Coates [9] was used to interpret the recorded IR absorption spectra in the following discussion.

All four spectra revealed characteristics of organic, unsaturated (C=C bond-containing) hydrocarbons due to the appearance of absorption signals at wavenumbers above 3000 cm^{-1} . In particular, the isolated absorptions around 3010 cm^{-1} and 3040 cm^{-1} are characteristic for simple unsaturated olefins, which are especially pronounced in debris type ②. Moreover, hydroxyl groups (-OH), visible through a broad band known to

exist between 3650 cm^{-1} and 3250 cm^{-1} , were clearly detected in debris (A) and less pronounced in debris (B) and (C). Debris (A) and, again to a lesser extent, (C) also showed the presence of carbonyl groups ($\text{C}=\text{O}$) between 1750 cm^{-1} and 1700 cm^{-1} . Debris types (C) and the unworn sample both show absorption signal below 1000 cm^{-1} , which are typical for trans-unsaturation ($\text{CH}=\text{CH}$). It is important to note that none of the measurements showed absorption signals typical for aromatic species (strong peak at 1500 cm^{-1}), which indicates that the benzene ring has been opened.

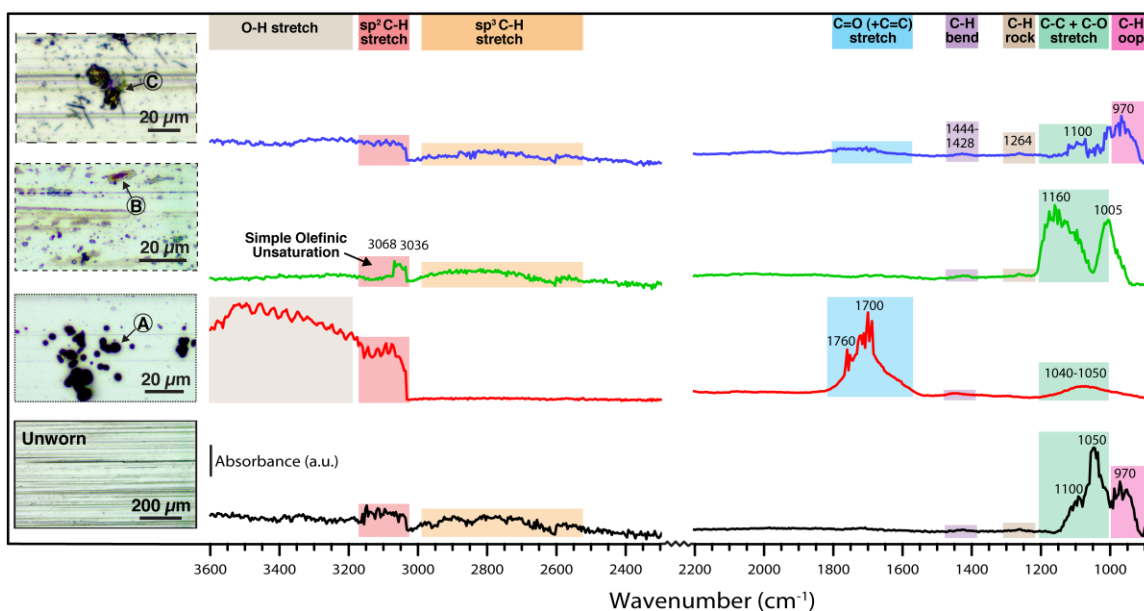


FIGURE 63: Nano infrared (nano-IR) measurements of the unworn Pt-coated shim stock and the three identified tribopolymer types. The break in signal between 2200 cm^{-1} and 2300 cm^{-1} corresponds to a change in excitation laser.

In summary, the unworn sample was found to possess absorption features typical of unsaturated species, more specifically, trans-unsaturated species. These features were weak and the spectra of the unworn sample are dominated by features

typical for aliphatic compounds. Debris ① showed very pronounced features typical for an organic, unsaturated polymer that contains a significant amount of hydroxyl and carbonyl groups. Debris ② exhibited features typical for an organic, simple olefinic unsaturated polymer, without any additional hydroxyl or carbonyl groups. The brown color of debris ② is typical for nitrogen-containing compounds. However, the nanoIR signals did not reveal a clear amino-group signal. The nitrogen-signals could be below the detection limit of the nanoIR measurement and warrant further spectroscopy measurements (see chapter 5.3). Finally, debris ③ shows features of both the unworn sample and debris ①. This is due to the fact that debris ③ is partially composed of worn-off Pt-coating mixed with debris ①. This leads to believe that only two different tribopolymers were produced: the organic, black-colored, unsaturated, hydroxyl- and carbonyl-containing debris ① and the organic, brown-colored, simple olefinic unsaturated debris ②.

4.3 Summary

This section presented a methodology to produce quantities of tribopolymer in Pt-Pt contacts that allow for spectroscopic analysis. The goal of this study is to gain knowledge of the chemistry and structure of the formed tribopolymer in order to systematically design materials that are immune to tribopolymer formation. A macrotribometer was used to slide a Pt-coated ball on a Pt-coated counter surface in a hydrocarbon-containing (benzene) atmosphere to accelerate tribopolymer growth. Two kinds of tribopolymers were produced and spectroscopically analyzed. The first one was an organic, black-colored, unsaturated, hydroxyl- and carbonyl-containing tribopolymer

and the second one an organic, brown-colored, simple olefinic unsaturated tribopolymer. This work demonstrates that polymer-like substances can be formed from airborne hydrocarbons under sufficient mechanical loading and catalytic activity of the contact materials.

BIBLIOGRAPHY CHAPTER 4

- [1] Streller, F.; Wabiszewski, G. E.; Carpick, R. W. *IEEE Nanotechnol. Mag.*, DOI: 10.11109/MNANO.2014.2373451.
- [2] Moore, A. C.; Burris, D. L. *Osteoarthritis and Cartilage* **2015**, *23*, 161-169.
- [3] Bonnevie, E. D.; Baro, V. J.; Wang, L.; Burris, D. L. *Tribol. Lett.* **2010**, *41*, 83-95.
- [4] Hermance, H. W.; Egan, T. F. *Bell Syst. Tech. J.* **1958**, *37*, 739-776.
- [5] Brand, V; Baker, M. S.; de Boer, M. P. *Tribol. Lett.* **2013**, *51*, 341-356.
- [6] Brand, V; Baker, M. S.; de Boer, M. P. *J. Microelectromech. Syst.* **2013**, *22*, 1248-1250.
- [7] Brand, V; Saleh, M. P.; de Boer, M. P. *Tribol. Int.* **2015**, *85*, 48-55.
- [8] Qi, Y.; Yang, J; Rappe, A. M. *ACS Appl. Mater. Interfaces* **2016**, *8*, 7529-7535.
- [9] Coates, J. *Interpretation of Infrared Spectra, A Practical Approach* in Encyclopedia of Analytical Chemistry; John Wiley & Sons Ltd: Chichester, 2000.
- [10] NanoIR2 Brochure, Anasys Instruments,
<http://www.anasysinstruments.com/nanoIR2Brochure.pdf>, accessed 6/20/2016

CHAPTER 5: CONCLUSIONS AND FUTURE DIRECTIONS

In this dissertation, we have discussed the assessment and the development of next-generation contact materials with applications in nanoelectromechanical (NEM) switches. Additionally, a macrotribology-based methodology to produce a large quantity of tribopolymer was presented.

Despite the large driving force to employ NEM switches as “beyond CMOS” [1], low-power field effect transistor replacement [2] these efforts are currently hindered by reliability issues in the contact interface [3]. The electrical contact has to be able to physically open and close up to a quadrillion (10^{15}) times without failing, which typically occurs due to adhesion (by sticking shut) or contamination (reducing switch conductivity) [2]. These failure mechanisms are not well understood, and materials that exhibit the needed performance have not been demonstrated. Thus, commercially viable NEM switches demand the scientific development and characterization of novel contact materials, along with efficient methods to evaluate the interfacial performance of these materials.

In order to effectively assess NEM switch contact material candidates under device-like conditions, we developed a novel, high-throughput electrical contact screening method based on PeakForce Tapping® (Bruker Corporation, Billerica, MA) atomic force microscopy (AFM) that enables the simultaneous evaluation of electrical contact resistance and adhesion during millions of contact cycles to be tested in laboratory timeframes [4]. We developed AFM probe holders that enable sputter coating of AFM tips with various materials as well as the thermal annealing of AFM probes to facilitate solid-state diffusion reactions. We cycled self-mated Pt contacts under forces

and environments representative of NEM switch operation for ten million times, while recording the electrical contact resistance and adhesion. The contact resistance increased more than three decades due to cycling-induced growth of insulating tribopolymer. We then employed different Pt-Pt contact pre-treatment methods, including slide-cleaning and plasma-cleaning, and found that slide-cleaning can reduce the amount of electrical degradation. Plasma-cleaning however, was seen to completely inhibit the electrical degradation of Pt-Pt contacts cycled for ten million cycles due in part to the removal of absorbed adventitious carbon prior to cycling. This suggests a route for mitigating contamination-induced failure.

We further developed novel contact material candidates that are highly conductive, minimally adhesive, chemically inert, mechanically robust, and amenable to CMOS fabrication processes. Specifically, we investigated platinum silicide (Pt_xSi) [5]. We showed that the controlled diffusion of sequentially-deposited thin films of amorphous silicon and platinum allows tunability of the chemical composition of Pt_xSi over a wide range ($1 < x < 3$) [6,7]. We measured the mechanical and electrical contact properties of Pt_xSi of multiple stoichiometries and then compared them with pure Pt. These experiments showed that the Pt-rich silicide phase (Pt_3Si) may be an excellent contact material for NEM switches due to its desirable combination of mechanical robustness with metal-like conductivity. We also demonstrate that Pt_xSi can be used to release NEM switches with a self-formed gap caused by interfacial separation driven by shrinkage-induced tensile stress. In order to better understand the effect of Pt_xSi stoichiometry on electrical structure and properties, we compared valence band X-ray photoelectron spectroscopy and theoretical density of states (DOS) calculations [8]. We found that increasing the silicon content in Pt_xSi decreases the carrier density. Among all

Pt_xSi phases, Pt₃Si offers the highest DOS due to the modest shift of the Pt_{5d} manifold away from the Fermi edge by only 0.5 eV compared to Pt, rendering it promising for applications. These results, demonstrating tunability of the electronic structure of thin metal silicide films, suggest that metal silicides can be designed to achieve application-specific electronic properties. Finally, we presented preliminary results on the AFM-based assessment of Pt_xSi contacts with application in NEM switches. Pt_xSi AFM probes were fabricated through solid-state diffusion and cycled against Pt counter surface under forces and environments representative of NEM switches. The electrical contact resistance was found to remain within the same order of magnitude throughout ten million interaction cycles, demonstrating the highly promising properties of Pt_xSi for NEM switch applications.

Lastly, we presented a methodology to produce quantities of tribopolymer in Pt-Pt contacts that allow for spectroscopic analysis. The goal of this study is to gain knowledge of the chemistry and structure of the formed tribopolymer in order to systematically design materials that are immune to tribopolymer formation. A macrotribometer was used to slide a Pt-coated ball on a Pt-coated counter surface in a hydrocarbon-containing (benzene) atmosphere to accelerate tribopolymer growth. Two kinds of tribopolymers were produced and spectroscopically analyzed. The first one was an organic, black-colored, unsaturated, hydroxyl- and carbonyl-containing tribopolymer and the second one an organic, brown-colored, simple olefinic unsaturated tribopolymer. This work demonstrates that polymer-like substances can be formed from airborne hydrocarbons under sufficient mechanical loading and catalytic activity of the contact materials.

Based on these conclusions, several avenues for further investigation are suggested in the following sections.

5.1 Future work on contact material assessment

Our previous work on developing and fabricating AFM probe holders for sputter deposition and rapid thermal annealing (RTA) in conjunction with the developed AFM cycling protocol using PeakForce Tapping®, sets the stage for time-efficient materials screening to be conducted. While the sputter and RTA holder are working perfectly, there are still some areas where the PeakForce Tapping® methodology could be improved.

As described in section 2.3.1 does the PeakForce Tapping® methodology produce one data point for the contact resistance vs. cycle number and adhesion vs. cycle number plots every 3000 cycles. This comes from the averaging of a 200 nm x 200 nm area, which takes 3 seconds to scan at 1 kHz tapping frequency and 2 Hz scan rate. In other words – the tip makes 3000 contacts with the sample while scanning the 200 nm x 200 nm area, which then gets averaged to one data point. This 3000 cycle spacing delivers a high information density for large cycle numbers ($>10^5$), but lacks information below these numbers. Especially the fact that the first recorded data point comes after 3000 cycles is worrisome since low-cycle changes to the tip-sample contact are averaged out this way. We therefore propose to accompany the PeakForce Tapping® tests with slow force-distance cycling to capture the low-cycle number behavior more accurately. Here is a possible experimental plan to implement the proposed changes:

1. Load AFM probe and sample.

2. Perform test resistor check.
3. Calibrate AFM deflection sensitivity and cantilever stiffness.
4. Perform force-distance measurements (same normal force and bias voltage then used later in the PeakForce Tapping® method) in a 5 x 5 grid over a 200 nm x 200 nm area. Take 120 images.
5. Switch using mode to PeakForce Tapping®
6. Perform PeakForce Tapping® measurements in same 200 nm x 200 nm area until desired cycle count is reached.

The implementation of force-distance “cycling” prior to PeakForce Tapping® measurements creates data points spaced only 25 cycles apart (or even smaller if the user were to choose a 4x4 or 3x3 grid) up to 3000 cycles while still averaging over a 200 nm x 200 nm area. Figure 64 shows example Pt-Pt cycling data sets recorded using a combination of slow force-distance cycling followed by PeakForce Tapping®. While comparing Figure 64 with Figure 57, one can see the information gained from the early lifetime behavior (low cycling count regime). (Note: a mistake happened while switching from fast F-D curves to PeakForce Tapping® mode during the experiment shown at Figure 64 that led to the large data gap between 1500 and 30000 cycles. If carried out correctly, the first PeakForce Tapping® data point will appear at 3000 cycles.) The adhesion information in the first 10s to 100s of contacting cycles is especially important to evaluate if the tip underwent any severe plastic deformation through the first 10s to 100s of cycles, which would be visible by a drastic change in adhesion force (or a loss in electrical conductivity of the coating were to be removed). It is therefore advised to perform slow force-distance cycling prior to PeakForce Tapping® measurements in the

future to achieve continuous contact resistance and adhesion data from 10^1 to 10^7 cycles.

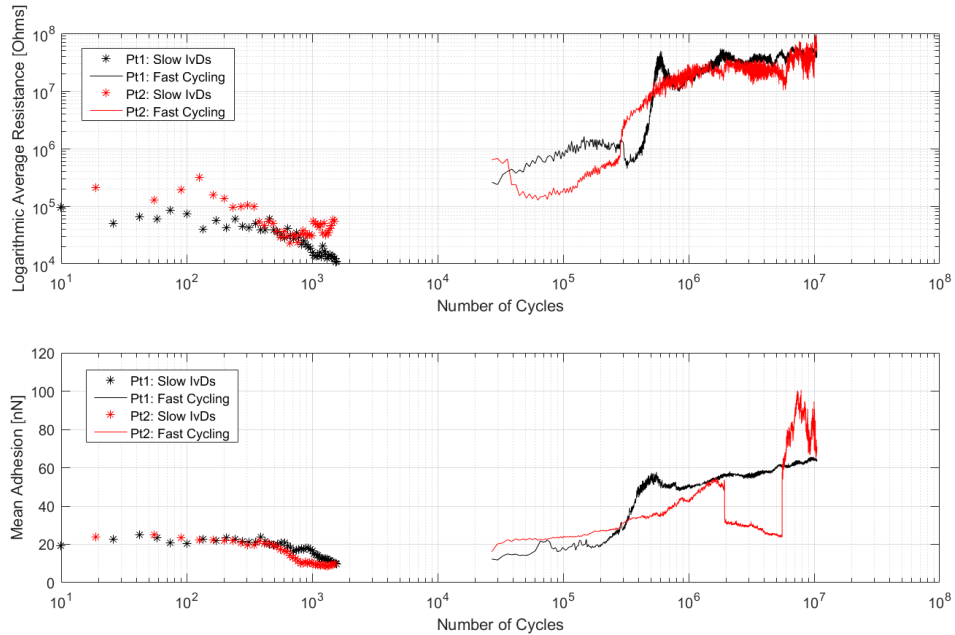


FIGURE 64: Example of Pt-Pt cycling tests conducted with modified cycling methodology including slow force-distance cycling in the beginning of the test.

A second route to improve the presented PeakForce Tapping® cycling methodology is to accompany it with transmission electron microscopy (TEM) images of the AFM probe tip before and after cycling. These images would provide very useful information to quantify the amount of tribopolymer formation, similarly to Figure 21, and to observe possible plastic deformation of the AFM probe tip. TEM images can be especially important once different contact material candidates are compared with each other. The formed tribopolymer can be easily identified in the TEM and therefore allows for a comparison of the tribopolymer thicknesses of different contact material pairs. It is

also important to compare the shape of the AFM probe tip before and after cycling to exclude the effect of plastic deformation on the measured contact resistance and adhesion values. One has to be sure that an increase in contact resistance is associated with tribopolymer formation and not with plastic deformation reducing the contact area or removing the conductive coating.

Finally, one can consider expanding the amplitude-modulation AFM-based method (AM-AFM) presented in Chapter 2.2 to achieve a higher cycle count. So far we have used AM-AFM to cycle an AFM probe at its resonance frequency (~ several 10s of kHz) against a counter surface to achieve several billion interaction cycles in laboratory timeframes. Higher cycle counts are desirable in order to investigate the long life behavior of nanoscale contacts. This can be achieved by using the presented AM-AFM methodology at higher interaction frequencies by oscillating the cantilever at higher harmonics. The heterodyne method, described in Ref. 9, allows for cycling frequencies of several MHz and could potentially achieve up to $5 \cdot 10^{10}$ cycles in laboratory timeframes.

5.2 Future work on contact material development

In chapter 3 we established Pt₃Si thin films as novel wear resistive and electrically conductive coating. This attractive property combination renders these films of interest for NEM switches, as well as AFM probe coating for conductive AFM measurements (c-AFM). Typically, Pt- or AuIr-coated AFM probes are commercially available for c-AFM measurements. These coatings wear off very quickly, especially if a mechanically robust sample is scanned. Recently, PtSi-coated AFM probes reached the market (PtSi-FM Probes, NANOSENSORS™, Neuchatel, Switzerland) and seem

attractive due to their increased mechanical robustness. However, the inherently low electrical conductivity of PtSi inhibits the use of these probes for many c-AFM samples. The highly electrically conductive and mechanically robust Pt₃Si stoichiometry fills this void and is not attainable using the fabrication process implemented in the commercial PtSi probes (the sc-Si probe body is used as Si source for silicidation, which will deliver PtSi probes). We previously presented a fabrication process based on the solid-state reaction of thin Pt and a-Si films to produce Pt₃Si-coated AFM probes in Figure 55. In order to show the advantageous properties of Pt₃Si probes in comparison to Pt, Au or commercial PtSi probes, wear tests are recommended. Pt, Au and PtSi AFM probes can be easily fabricated using the sputtering and rapid thermal annealing holders presented in section 2.1.2. A Hysitron TI-950 TriboIndenter (Hysitron Corp., Minneapolis, MN), available in Prof. Kevin Turner's Laboratory at the University of Pennsylvania, allows one to perform scratch tests using a diamond nanoindenter tip. It would be interesting to perform scratch tests on Pt₃Si-, Pt-, Au-, and PtSi-coated sc-Si wafers and compare the scratch resistance and wear volume of these films.

A second avenue would be to perform *in situ* single-asperity wear and contact cycling tests inside a TEM using a Hysitron PicoIndeter (Hysitron Corp., Minneapolis, MN). This piece of equipment is available at the University of Pennsylvania and can be used to perform scratch tests in which a diamond indenter is pressed against Pt₃Si-, Pt-, Au-, or PtSi-coated AFM probes and then laterally displaced by a fixed amount. Figure 65 shows a schematic of the Hysitron PicoIndenter setup. Image tracing of the AFM tip shape before and after these tests allows for the accurate determination of the wear volume [10]. Since the diamond indenter is electrically conductive, a bias can be applied between AFM probe and indenter to reveal wear volume and electrical current for Pt₃Si-,

Pt-, Au-, and PtSi-coated AFM probes. In order to compare the cycling behavior of these coatings, the PicoIndenter probe (conductive diamond) can be cycled against the coated AFM tips, whose cantilever provides accurate force resolution, while a bias is applied between indenter and probe. Cycling experiments using Pt₃Si AFM probes can be compared to Pt, Au, and commercial PtSi AFM probes. Overall it can be expected that the Pt₃Si-coated AFM probes come close to the electrical performance of Pt-coated AFM probes while also possessing the mechanical robustness of the commercial PtSi AFM probes. These measurements would strengthen the position of Pt₃Si as novel electrically conductive and wear resistive coating. Lastly, environmental TEM could be utilized to test the susceptibility to tribopolymer formations for different contact material pairs under varying atmospheres.

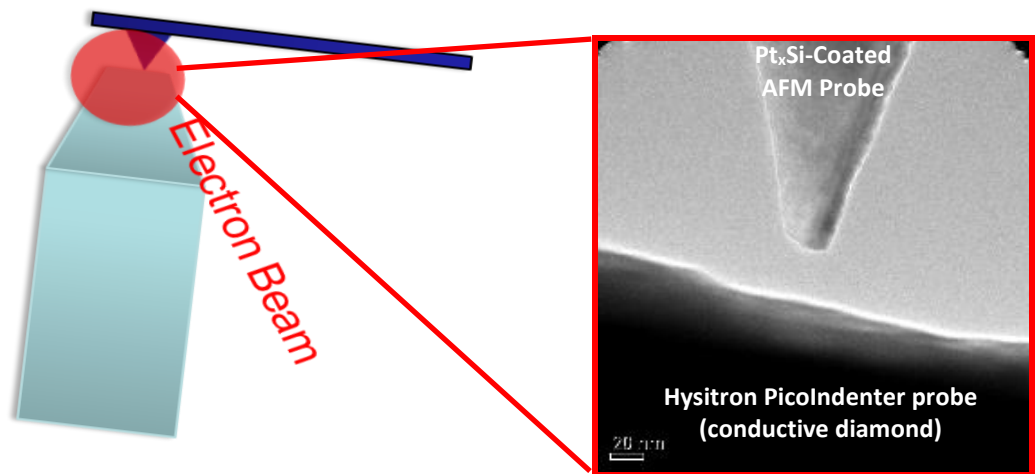


Figure 65: Schematic of the *in situ* TEM cycling and scratch tests setup. A Hysitron PicoIndenter probe made out of conductive diamond will be cycled or scratched against a Pt_xSi or any other coated AFM probe under an applied bias. In the case of cycling, the pull-off force and contact resistance can be measured during the test to evaluate the early-lifetime behavior of the single-asperity contact.

In addition to performing *in situ* switching and wear tests, the TEM can be used to characterize and observe the *in situ* Pt_xSi formation. The Hysitron PicoIndenter is equipped with electrical connections that are used to apply a bias in the previously described switching experiments. Heatable AFM probes (Anasys Instruments, Santa Barbara, California) that are coated with *a*-Si and Pt thin films can be heated up by connecting them to these electrical connections [11]. This allows the direct observation of the Pt/*a*-Si interdiffusion to form Pt_xSi. Electron diffraction can be conducted to characterize the crystal structure changes associated with the different Pt_xSi stoichiometries.

Pt_xSi recently gained scientific attention as candidate material for a variety of novel applications, such as plasmonics [12], lithium-ion batteries [13], field emitters [14-16], and thermoelectrics [17-20]. However, researchers [12,13] have pointed towards a lack of knowledge about the exact properties of Pt_xSi and other metal silicides for these applications. With the methodology of producing stoichiometrically-controlled Pt_xSi thin films in place, it would be interesting to test the different Pt_xSi stoichiometries with respect to their performance in aforementioned applications.

Next to studying the performance of Pt_xSi as NEM switch contact material, titanium nitride (TiN), ruthenium (Ru), and graphene-coated Pt (gr-Pt) were tested as well, in a preliminary mode. We tested commercial TiN coated AFM probes (NT-MDT America Inc., Tempe, AZ) and found that these probes, while offering very good mechanical robustness, are extremely prone to oxide formation. This resistive oxide was found to inhibit current flow, making TiN unusable in NEM switches unless highly

controlled NEM switch packaging is pursued. We fabricated Ru-coated⁷ AFM probes using the sputter holder presented in section 2.1.2. We performed X-ray photoelectron spectroscopy (XPS) analysis of the deposited Ru films and found that an oxide was quickly formed upon removal of the films from the deposition chamber. Valence band XPS measurements revealed a high density of states in the RuO_x films, confirming the conductive nature of the oxide. The Ru-coated AFM probes were subjected to the PeakForce Tapping® cycling methodology presented in section 2.3, including measurements featuring a slide and plasma-cleaning pretreatment. Figure 66 shows the results for as-deposited, slide-cleaned, and oxygen plasma cleaned Ru-probes cycled against a Pt-coated flat. It can be seen that the as-deposited Ru-coated AFM probes, covered with their conductive oxide, performed well by only exhibiting an order of magnitude increase in contact resistance over 10⁷ cycles. The slide-cleaning did not lead to better cycling performance in the case of Ru-Pt contacts, unlike it was seen previously for Pt-Pt contacts. The contact resistance of the slide-cleaned contact increased by three orders of magnitude through the switching experiment. The plasma-cleaned Ru AFM probe and Pt flat reached an open circuit condition (no current flow detectable) after 8·10⁴ cycles, indicating a detrimental effect of the oxygen plasma cleaning on the Ru-Pt contact pairing. A XPS study to elucidate the effect of oxygen plasma cleaning on a Ru surface covered with its native oxide would give more insight into possible causes for the behavior shown in Figure 66.

⁷ The Ru sputtering target used to fabricate the Ru-coated AFM probes is courtesy of Prof. I-Wei Chen (University of Pennsylvania).

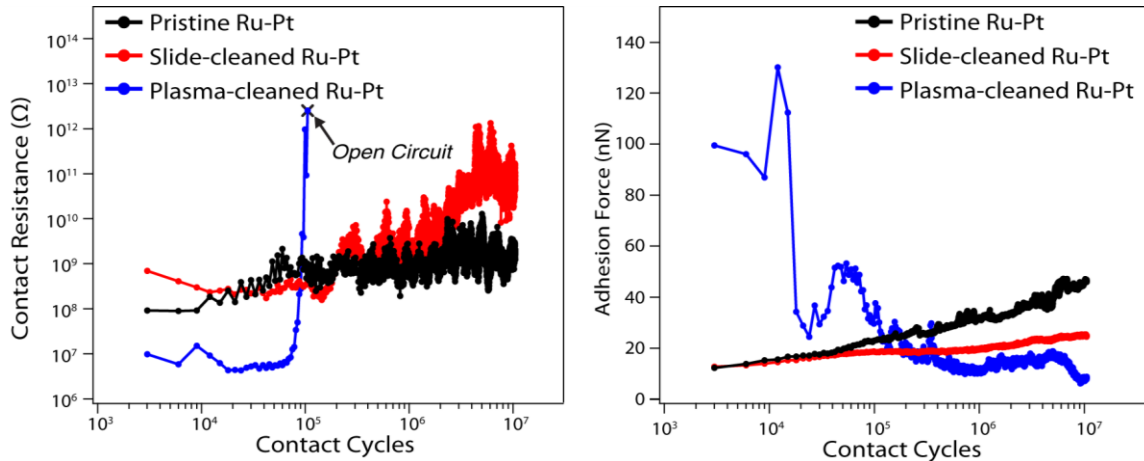


FIGURE 66: Contact resistance and adhesion as a function of contact cycles for Ru-coated AFM probes in different pretreatment states.

Finally, gr-Pt was studied as possible contact material in nanoscale contacts. While an integration of graphene into a NEM switch fabrication process seems impossible due to the high growth temperature of graphene on Pt of over 1000 °C [20], the study of graphene-covered Pt could lead to more insight regarding the tribopolymer formation in Pt contacts. Tribopolymer forms on Pt due to absorption of airborne hydrocarbons, followed by stress-induced polymerization as discussed in section 3.3.5. Graphene is known to be impermeable by gases and thus prevents the absorption of hydrocarbons on Pt, and thereby tribopolymer formation, while offering electrical conductivity [22]. We grew few-layer graphene on a Pt foil (> 90% coverage) for 2 hours at 1100 °C under CH₄ atmosphere⁸. Figure 67 shows a representative force distance and current-distance curve ($V_{\text{bias}} = 50 \text{ mV}$) of a Pt probe making contact with the gr-Pt sample. It can be seen that the electrical resistance of the tip-sample contact is 125 kΩ.

⁸ The graphene growth on Pt foil was carried out by Dr. Jinglei Ping (University of Pennsylvania)

We can therefore conclude that the graphene allows for sufficient current flow between the Pt-coated tip and sample to warrant further studies.

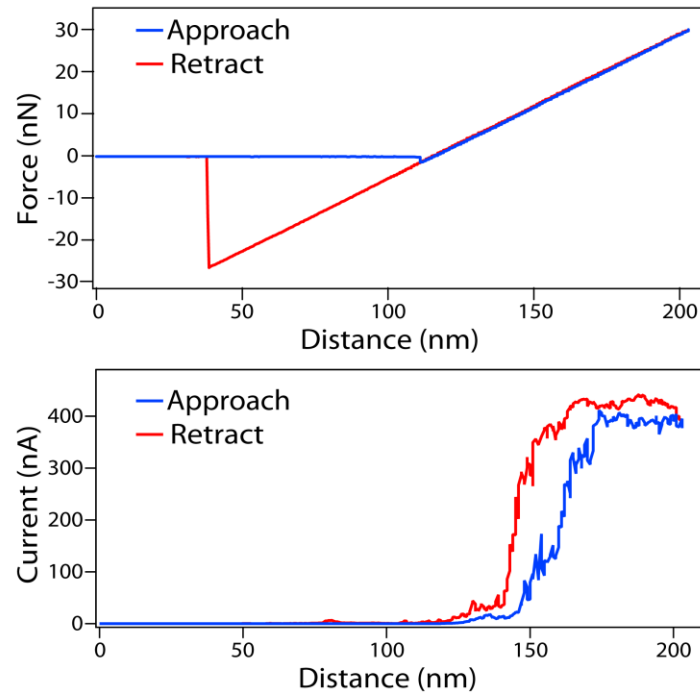


FIGURE 67: Force-distance and current-distance curves of a Pt-coated AFM probe against a graphene-coated Pt sample.

Figure 68 shows a scanning electron microscopy image of the gr-Pt sample. It can be seen that the Pt foil experienced large grain growth due to the high growth temperature of graphene. The inset in Figure 68 shows that a characteristic wrinkle pattern is present on the Pt surface that does not continue outside of each grain. It is not possible to tell whether the wrinkles come from the Pt or from the graphene covering the Pt.

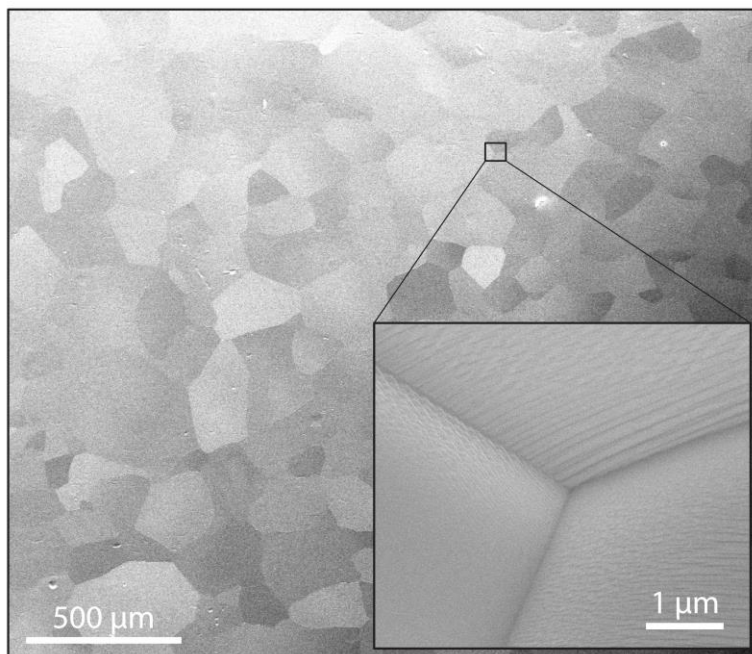


FIGURE 68: Scanning electron microscopy (SEM) image of the graphene-covered Pt foil.

Conductive AFM (C-AFM) measurements on the gr-Pt sample were conducted to further investigate the electrical behavior of this sample and the origin of the observed wrinkles. Figure 69 shows AFM topography and contact resistance measurements of the gr-Pt sample performed under 30 nN normal load and 5 mV bias. It can be seen that the regions of high current flow are closely coupled to regions of high topography (i.e. the top of the wrinkles). Minimum contact resistances of 10 k Ω were recorded during the scan, confirming the positive effect of shear stresses on low contact resistance values. Changing the normal loading during C-AFM scans did not have an effect on the appearance of the wrinkles, which leads to believe that the wrinkles are originated within the Pt foil. However, researchers studying graphene grown on Cu using high resolution

AFM observed similar wrinkle pattern and ascribed them to the graphene itself [23]. It is possible that the wrinkles are stable and thus not strongly affected by load.

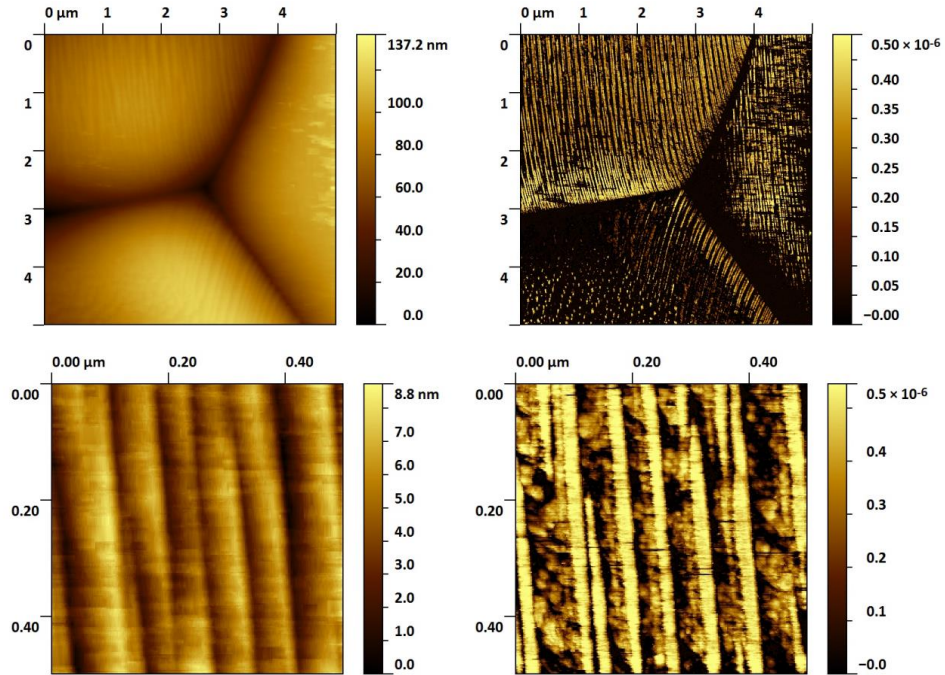


FIGURE 69: AFM topography and conductivity measurements of Gr-Pt sample. Top row: 5 μm x 5 μm topography (left) and conductivity (right, in A) scan on Gr-Pt sample. Bottom row: 500 nm x 500 nm topography (left) and conductivity (right, in A) scan on Gr-Pt sample.

While the AFM-based experiments proved that the gr-Pt sample is electrically conductive, it first should be proven that graphene is completely covering the surface before the PeakForce Tapping® cycling methodology is employed. A logical next step is therefore to perform Raman spectroscopy on the gr-Pt sample. In order to obtain high quality Raman data, the graphene needs to be transferred to another substrate. The Pt

foil will need to be etched and the remaining graphene transferred to, for example, a Si wafer. After successful confirmation of the graphene presence, AFM-based cycling tests should be conducted on the gr-Pt sample and compared to Pt-Pt results. The graphene film presumably prevents or reduces tribopolymer formation and the gr-Pt sample should therefore perform better in AFM cycling tests than a Pt sample.

5.3 Future work on tribopolymer formation and characterization

While the work on the structural characterization of tribopolymers in macroscale Pt-Pt contacts demonstrated that polymer-like substances can be formed from airborne hydrocarbons under sufficient mechanical loading and catalytic activity of the contact materials, additional characterization and experiments are necessary to completely elucidate the complete polymer structure.

Chapter 4.2 showed that two kinds of tribopolymers were formed. The first one was an organic, black-colored, unsaturated, hydroxyl- and carbonyl-containing tribopolymer and the second one an organic, brown-colored, simple olefinic unsaturated tribopolymer. The brown color of the second formed tribopolymer suggests the presence of nitrogen-containing groups [24]. Energy-dispersive X-ray spectroscopy (EDX) measurements are suggested in order to prove that the brown tribopolymer, which is similar in color to the tribopolymer formed by Hermance & Egan [25], is in fact nitrogen-containing. Additionally, the sp^2/sp^3 carbon hybridization of the tribopolymers is of interest and can be determined using electron energy loss spectroscopy (EELS) inside a TEM or using imaging Near Edge X-Ray Absorption Fine Structure (NEXAFS) measurements.

In addition to spectroscopic measurements, nanoindentation measurements could reveal valuable information regarding the mechanical robustness of the tribopolymer. This information is especially important to accurately model a single asperity tribopolymer-containing contact in molecular dynamics simulations. The Hysitron TI-950 TriboIndenter (Hysitron Corp., Minneapolis, MN) available at the University of Pennsylvania could be used to accurately determine the mechanical properties of the formed tribopolymer.

Another interesting avenue would be to change the experimental setup from a ball on flat in sliding configuration to a ball on flat in switching configuration. An experiment where the Pt-coated ball is switched against the Pt-coated counter surface in a benzene atmosphere would deliver tribopolymer formation under similar stress states than they are inside NEM switches. It would be interesting to compare the quantity and structure tribopolymers formed in sliding contacts to the tribopolymer formed in impacting contacts. The previously used custom-made macrotribometer [26,27] is able to perform aforementioned task, however maximum switching frequencies of only few tens of Hz can be achieved.

A second expansion of the macrotribology experiment would be to test other materials, besides Pt, and their affinity to tribopolymer formation and the structure of the formed species. Pt_xSi would be a logical next material to test to experimentally verify the proposed lower affinity to tribopolymer formation in Pt_xSi contacts. A steel ball and shim stock can be subsequently sputter-coated with *a*-Si and Pt followed by a thermal annealing treatment to form Pt_xSi .

While performing further characterization on the already formed tribopolymer or when conducting new experiments, it will be very important to compare these results to

the density functional theory calculations performed by the Rappe Group at the University of Pennsylvania [28]. Validation of experimental results through their theoretical calculations and vice versa will prove to be extremely valuable in unlocking the tribopolymer formation mechanism in electro-mechanical contacts and to ultimately design materials that are resistant to tribopolymer formation.

BIBLIOGRAPHY CHAPTER 5

- [1] "International technology roadmap for semiconductors (2009 edition)," 2009.
- [2] Loh, O. Y.; Espinosa, H. D. *Nat. Nanotech.* **2012**, 7, 283–295.
- [3] Chen, L.; Guo, Z. J.; Noshi, N.; Eid, H.; Adams, G. G.; McGruer, N. E. *J. Micromech. Microeng.* **2012**, 22, 045017.
- [4] Streller, F.; Wabiszewski, G. E.; Carpick, R. W. *IEEE Nanotechnol. Mag.*, DOI: 10.11109/MNANO.2014.2373451.
- [5] Bhaskaran, H.; Sebastian, A. *IEEE T. Nanotechnol.* **2009**, 8, 128.
- [6] Streller, F.; Wabiszewski, G. W.; Mangolini, F.; Feng, G.; Carpick, R. W. *Adv. Mater. Interfaces* **2014**, 1, 1300120.
- [7] Streller, F.; Agarwal, R.; Mangolini, F.; Carpick, R. W. *Chem. Mater.* **2015**, 27, 4147–4253.
- [8] Streller, F.; Qi, Y.; Yang, J.; Mangolini, F.; Rappe, A. M.; Carpick, R. W. *J. Phys. Chem. Lett.* **2016**, 6, 2573–2578.
- [9] Dupas, E.; Gremaud, G.; Kulik, A.; Loubet, J.-L. *Rev. Sci. Instrum.* **2001**, 71, 3891-3897.
- [10] Jacobs, T. D. B.; Carpick, R. W. *Nat. Nanotechnol.* **2013**, 8, 108-112.
- [11] Liu, J; Somnath, S.; King, W. P. *Sens. Actuators* **2013**, 201, 141-147.
- [12] Naik, G. V.; Shalaev, V. M.; Boltasseva, A. *Adv. Mater.* **2013**, 25, 3264-3294.
- [13] Liu, C; Li, F.; Ma, L.-P.; Cheng, H.-M. *Adv. Mater.* **2010**, 22, E28-E62.
- [14] Lin, H.-K.; Cheng, H.-A; Lee, C.-Y.; Chiu, H.-T. *Chem. Mater.* **2009**, 21, 5388-5396.
- [15] Li, H.; Wu, J.; Wang, Z. M. *Silicon-based Nanomaterials*, Springer: Berlin, 2013.
- [16] Higgins, J. M.; Ding, R.; Jin, S. *Chem. Mater.* **2011**, 23, 3848-3853.
- [17] Rowe, D. M. *Thermoelectrics Handbook: Macro to Nano*, Taylor & Francis Group: Abingdon, 2006.
- [18] Fedorov, M. I. *J. Thermoelectr.* **2009**, 2, 51-60.

- [19] Itoh, T.; Yamada, M. *J. Electron. Mater.* **2009**, *38*, 925-929.
- [20] de Boor, J.; Dasgupta, T.; Kolb, H.; Compere, C.; Kelm, K.; Mueller, E. *Acta Mater.* **2014**, *77*, 68-75.
- [21] Kang, B. J.; Mun, J. H.; Hwang, C. Y.; Cho, B. J. *J. Appl. Phys.* **2009**, *106*, 104309.
- [22] Berry, V. *Carbon* **2013**, *62*, 1-10.
- [23] Egberts, P.; Ye, Z.; Liu, X.-Z.; Dong, Y.; Martini, A.; Carpick, R. W. *Phys. Rev. B* **2013**, *83*, 035409.
- [24] Coates, J. *Interpretation of Infrared Spectra, A Practical Approach* in Encyclopedia of Analytical Chemistry; John Wiley & Sons Ltd: Chichester, 2000
- [25] Hermance, H. W.; Egan, T. F. *Bell Syst. Tech. J.* **1958**, *37*, 739-776.
- [26] Moore, A. C.; Burris, D. L. *Osteoarthritis and Cartilage* **2015**, *23*, 161-169.
- [27] Bonnevie, E. D.; Baro, V. J.; Wang, L.; Burris, D. L. *Tribol. Lett.* **2010**, *41*, 83-95.
- [28] Qi, Y.; Yang, J.; Rappe, A. M. *ACS Appl. Mater. Interfaces* **2016**, *8*, 7529-7535.